DATA DRIVEN MODELING AND PREDICTIVE CONTROL OF COMBUSTION AT REACTIVITY CONTROLLED COMPRESSION IGNITION ENGINES

By

Behrouz Khoshbakht Irdmousa

A DISSERTATION

Submitted in partial fulfillment of the requirements for the degree of

DOCTOR OF PHILOSOPHY

In Mechanical Engineering - Engineering Mechanics

MICHIGAN TECHNOLOGICAL UNIVERSITY

2023

This dissertation has been approved in partial fulfillment of the requirements for the Degree of DOCTOR OF PHILOSOPHY in Mechanical Engineering - Engineering Mechanics.

Mechanical Engineering–Engineering Mechanics Department

Dissertation Co-advisor: *Dr. Jeffrey D. Naber*

Dissertation Co-advisor: *Dr. Mahdi Shahbakhti*

Committee Member: *Dr. David Wanles*

Committee Member: *Dr. Jeremy Worm*

Department Chair: *Dr. Jason Blough*

Dedication

To my parents for their boundless love and support.

Contents

List of Figures

List of Tables

Preface

The contents of the PhD dissertation are mainly based on one published journal papers, three published conference papers and one journal paper under preparation. Publishers of these papers have granted permission for reuse of material (Appendix C). The contributions of the authors in these papers are as follows:

- Chapter 2. Data-driven modeling and predictive control of combustion phasing for RCCI engines. The data-driven linear parameter varying algorithm was developed by Syed Zeeshan Rizvi and Javad Mohammadpour and used by Behrouz Khoshbakht Irdmousa for identification of combustion dynamics at a reactivity controlled compression ignition engine. Experimental data from the RCCI engine at Energy Mechatronics (EML) Lab were collected by Behrouz Khoshbakht Irdmousa and were used to develop and validate the data driven dynamic model for RCCI engine. The identified dynamics model were used by Behrouz Khoshbakht Irdmousa at a model predictive controller strategy which was collaboratively developed by Akshat Raut and Behrouz Khoshbakht Irdmousa. Later Behrouz Khoshbakht Irdmousa used the developed MPC controller to control crank angle for 50% fuel burnt at an actual RCCI engine. Dr. Mahdi Shahbakhti and Dr. Naber supported these works by providing technical advice and evaluating the results.

◇ Chapter 3. This chapter uses an input-output based approach which was crated by Zeeshan Rizvi and Javad Mohammadpour. Behrouz Khoshbakht Irdmousa adapted this method to model RCCI combustion dynamics without requiring any state definition. The model was trained and tested with experimental data obtained by Behrouz Khoshbakht Irdmousa. Later, the input-output based dynamic model were used at a constrained model predictive controll strategy which was formulated by Behrouz Khoshbakht Irdmousa and a MIMO controller were formed to control combustion phasing and load at an RCCI engine. Dr. Mahdi Shahbakhti and Dr. Naber provided valuable technical advices during this process.

◇ Chapter 4. In this study a physics-based maximum pressure rise rate model were developed by Aditya Basina using steady state data from a validated RCCI engine model. Behrouz Khoshbakht Irdmousa used it and developed a control oriented maximum pressure rise rate model using transient data from an RCCI engine. Behrouz Khoshbakht Irdmousa also developed a control oriented data driven model for RCCI engine based on linear parameter varying model. Control-oriented data-driven and physics-based Modeling of Maximum Pressure Rise Rate in Reactivity Controlled Compression Ignition Engines are also completed in this section.

◇ Chapter 5. Input output based data driven model for reactivity and stratification modeling Behrouz Khoshbakht Irdmousa developed an open

cycle computational fluid dynamics model for the RCCI engine at EML Lab. He validated the model based on steady state and transient experimental data. He also developed chemical reactivity index and stratification index for engine relevant condition and dual fuel mixtures. He ran the high fidelity CFD model based on transient inputs and generated transient reactivity and stratifcation variation data for the related inputs. These data were used by Behrouz Khoshbakht Irdmousa for developing two data driven models based on linear parameter varying method and input-output based Kernel Canonical Correlation Analysis (KCCA) methods for chemical reactivity and stratification at an RCCI engine.

Acknowledgments

This work would not have been possible without the patient and dedicated guidance of my academic advisors, Dr. Jeffrey Naber and Dr. Mahdi Shahbakhti. I am indebted to Dr. Naber for giving me an opportunity to continue my education and pursue a Ph.D. degree in mechanical engineering. I will never forget his critical support during the initial months of my studies. I am grateful for the time and effort he invested in supporting my studies and providing technical and non-technical guidance. I am also very thankful to Dr. Mahdi Shahbakhti for choosing me as a research assistant to work on his National Science Foundation-supported project, supporting me through a research assistantship, and providing valuable ideas to advance my research. I should also thank the Dept. of Mechanical Engineering-Engineering Mechanics and especially Dr. Craig Fredrich for supporting my PhD work through Teaching Assistantships, and the Graduate School for providing support through the Finishing fellowship program.

I should thank Dr. Javad Mohammadpour from Clemson University and his students Zeeshan Rizivi and Yajie Bao for providing technical support for data-driven studies. I also appreciate Dr. Ali Borhan from Cummins Inc. for his insightful discussions on use of predictive models for engine control.

I would like to thank my friends and colleague at advanced power research center,

Ehsan Ansari, Niranjan Miganakallu, Hakan Uras, Stas Zinchik, Vinicius Vinhaes, Sid Gopujkar, William Hansley, Paul Dice for their support and friendship.

I am also thankful to my friends at Michigan Tech for their care and friendship which help me continue my education far away from my family. Seyfi Polat, Mohammadreza Nazemi, Shadi Darani, Hamit Solmaz, Ehsan Taheri, Emre Doguturk, Dr. Ali Ebnesari and his family, Mustafa Ozkal, Masoud Sarabi, Behdad Afkhami, Sarvesh Tendolkar, Arash Hoseinzadeh, Dr. Mohsen Azizi, Mahdi Soltani, Raheleh Salimi, Behzad Ahmadi, Eisa hedayati, Zhuyong Yang and others.

I owe everything in my life to the love and support I received from my parents, Sarah and Rasoul, my brothers, Sirous, Parviz and Sasan. Their belief in my abilities has always motivated me to continue improving myself, and for that I cannot thank them enough.

Nomenclature

List of symbols and abbreviations used in this work:

AFR	Air Fuel Ratio (-)
ANN	Artificial Neural Networks
AC	Alternating Current
BD	Burn Duration (CAD)
BDC	Bottom Dead Center
$BMEP$	Break Mean Effective Pressure (kPa)
BTE	Break Thermal Efficiency
$CA50$	Crank Angle for 50% Fuel Burnt (CAD aTDC)
CAD	Crank Angle Degree
CCA	Canonical Correlation Analysis
CDF	Conventional Dual Fuel
CDC	Conventional Diesel Combustion
CFD	Computational Fluid Dynamics
CNG	Compressed Natural Gas
COV	Coefficient of Variation
CO	Carbon Monoxide
DDM	Data Driven Modeling
DI	Direct Injection

e	Estimation or Tracking Error
E	Stochastic White Noise
E_k	Estimation Error
ECU	Engine Control Unit
EGR	Exhaust Gas Recirculation (%)
EML	Energy Mechatronic Lab
EOC	End of Combustion (CAD aTDC)
EU	European Union
EVC	Exhaust Valve Closing (CAD aTDC)
$FPGA$	Field Programmable Gate Array
$FRBS$	Fuzzy Rule Based System
FQ	Fuel Injected Per Engine Cycle (mg/cycle)
GA	Genetic Algorithm
GDI	Gasoline Direct Injection
$\mathcal{H}$	Forward Toeplitz Matrix
HC	Hydrocarbon
$HCCI$	Homogeneous Charge Compression Ignition
ICE	Internal Combustion Engine
ID	Ignition Delay (msec)
$IMEP$	Indicated Mean Effective Pressure (kPa)
IVC	Inlet Valve Close

IVO	Inlet Valve Open
J	MPC Cost Function
$\mathcal{J}$	Lagrangian Cost Function
$\mathcal{J}$	Least-square Cost Function
$KCCA$	Kernelized Canonical Correlation Analysis
$\mathcal{L}$	Lagrangian Function
$\mathcal{L}$	Lower Triangle Matrix
$\mathcal{L}$	Lagrangian Function
$LDCV$	Light Duty Commercial Vehicle
LDT	Light Duty Truck
LFT	Linear Fractional Transformation
LHV	Lower Heating Value (kJ/kg)
LPV	Linear Parameter Varying
LTC	Low Temperature Combustion
LTI	Linear Time Invariant
$MABX$	dSPACE MicroAutoBox
MPC	Model Predictive Control
$MPRR$	Maximum Pressure Rise rate (kPa/CAD)
MFB	Mass Fraction Burn (%)
$MIMO$	Multi-Input Multi-Output
MLR	Multi Linear Regression

MPC	Model Predictive Control
NOx	Nitrogen Oxide
$\mathcal{O}$	Observatory Matrix
p_k	Scheduling Variable at Time Instant k
P_{soc}	Pressure at Start of Combustion (kPa)
$PCCI$	Premixed Charge Compression Ignition
PFI	Port Fuel Injection
PID	Proportional Integral Derivative
PM	Particular Matter (-)
PPM	Particular Per Million (-)
PR	Premixed Ratio (-)
Q	Weighting Matrix on Tracking Error
$\mathcal{R}$	Past Inputs Matrix
R	Weighting Matrix on Magnitude of Control Action
R^2	Coefficient of Determination
$RCCI$	Reactivity Controlled Compression Ignition
RI	Ringing Intensity
RRI	Relative Reacivity Index
$RSME$	Root Mean Square Error
SI	Spark Ignition
SI	Stratification Index

SS	State Space
SOI	Start of Injection
SOC	Start of Combustion
SVM	Support Vector Machine
TDC	Top Dead Center
U	RCCI engine inputs
$\mathbb{U}$	RCCI Engine Inputs Over Prediction Horizon
UHC	Unburnt Hydrocarbon
$\mathcal{V}$	Past Outputs Matrix
W	Support Vector Weighting Matrix
X	RCCI engine states
$\mathcal{X}$	RCCI Engine States Over Entire Train Data
Y	RCCI engine outputs
$\mathcal{Y}$	RCCI Engine Outputs Over Entire Train Data
$\mathbb{Y}$	RCCI Engine Outputs Over Prediction horizon
Z	Future Plant Inputs and Outputs
α, β, κ, η	Lagrange Multipliers
φ	Feature Map Function
τ	Ignition Delay
Ψ	Reference Outputs Over Prediction Horizon
Φ	Prediction Matrix
Ω	Grammian Matrix

Ω	Prediction Matrix
Γ	Regularization Matrix
Ξ	Grammian Matrix
λ	Eigen Value

Abstract

Reactivity Controlled Compression Ignition (RCCI) engines operates has capacity to provide higher thermal efficiency, lower particular matter (PM), and lower oxides of nitrogen (NOx) emissions compared to conventional diesel combustion (CDC) operation. Achieving these benefits is difficult since real-time optimal control of RCCI engines is challenging during transient operation. To overcome these challenges, data-driven control-oriented models are developed in this study. These models are developed based on linear parameter-varying (LPV) modeling approach and input-output based Kernelized Canonical Correlation Analysis (KCCA) approach. The developed dynamic models are used to predict combustion timing (CA50), indicated mean effective pressure (IMEP), maximum pressure rise rate (MPRR), reactivity and stratification metrics as functions of fuel quantity (FQ), start of injection (SOI) timing and premixed ratio (PR) as the RCCI engine's control variables. The identified model is then used for the design of a model predictive controller (MPC) to control crank angle for 50% fuel burnt (CA50) for varying engine conditions on the actual RCCI engine. This study also established constrained multi-input multi-output (MIMO) model predictive controller (MPC) to track desired crank angle for 50% fuel burnt and IMEP at various engine conditions. This research has demonstrated and implemented two fast and reliable method to model highly nonlinear RCCI combustion engine and develop control-oriented models for RCCI combustion

Chapter 1

Introduction and Research Motivation

RCCI is a dual fuel low-temperature combustion (LTC) strategy for internal combustion engines (ICE) which runs with a blend of a low reactive fuel and a high reactive fuel. It offers higher fuel conversion efficiency at lower and medium loads and lower NOx emissions at higher loads compared to diesel and spark ignition (SI) engines [4]. The low-reactive fuel (e.g., gasoline) is introduced to fresh air via port fuel injection (PFI) which provides an opportunity to form a well-mixed blend of fuel, air, and recirculated exhaust gases, if any. The high-reactive fuel (e.g., diesel) is directly injected (DI) inside the cylinder during the compression stroke which creates a reactivity gradient in the combustion chamber. The controlled reactivity gradient

in RCCI engines causes longer combustion duration and lower pressure rise rates compared to homogeneous charge compression ignition (HCCI) engines [5]. In RCCI engines, ignition initially occurs at small isolated high reactive pockets which continue to grow and merge with other expanding pockets while other ignition pockets emerge. These reaction zones which are formed in high reactive zones proceed to low reactive regions to complete the combustion [6]. This form of distributed combustion initiation leads to lower gas temperature compared to conventional diesel combustion (CDC) which results in lower heat loss and higher fuel conversion efficiency. Due to the sensitivity of RCCI reactions to the thermal and chemical composition of air-fuel mixtures, combustion control of RCCI engines is a major challenge during transient operations. In RCCI engines, dual fuel blending ratio and multiple injections are employed as control variables to adjust global and local in-cylinder mixture reactivity which is used for control and optimization of combustion phasing, burn duration, and emissions in these engines [7].

1.1 Motivations

Internal combustion engines (IC engines) are a major power source for vehicles around the globe. The number of registered vehicles is projected to reach 1.47 billion vehicles (small, medium, and large-sized automobiles) including 279 million in the United States by 2023 [8]. 240 million passenger vehicles use internal combustion engines as

drive sources in the United States [9]. Therefore 13.3 million barrels of petroleum are consumed in the transportation sector in the United States each day. [10] The Significant role of internal combustion engines demonstrates the importance and value of research and development about them to improve their advantages such as efficiency and remove their drawbacks such as toxic emissions. The increased number of internal combustion engines in recent decades signifies their adverse emission effects on human health and efficiencies in countries' economies. Therefore, researchers are looking to improve IC engine's efficiencies and reduce their emissions. Several strict regulations including Euro and US emission standards were introduced and adopted to curb emissions and improve efficiencies.

Fig. 1.1 shows emission regulation development in the United States, European Union, China, and Brazil. The latest national emission standard in the United States limits particulate matter (PM) and oxides of nitrogen(NOx) to 0.03 g/kWh and 0.003 g/kWh, respectively [1]. To meet emission standards in diesel engines, several technologies such as after-treatment and low-temperature combustion (LTC) were introduced. After treatment, can bring emissions to acceptable ranges, however, with difficulty for NOx. To reduce the burden on after-treatment devices, in-cylinder combustion control strategies such as LTC can be implemented [11]. It has been confirmed that low-temperature combustion can reduce NOx without increasing PM emissions [12]. Reactivity controlled compression ignition (RCCI) is one of LTC combustion strategies.

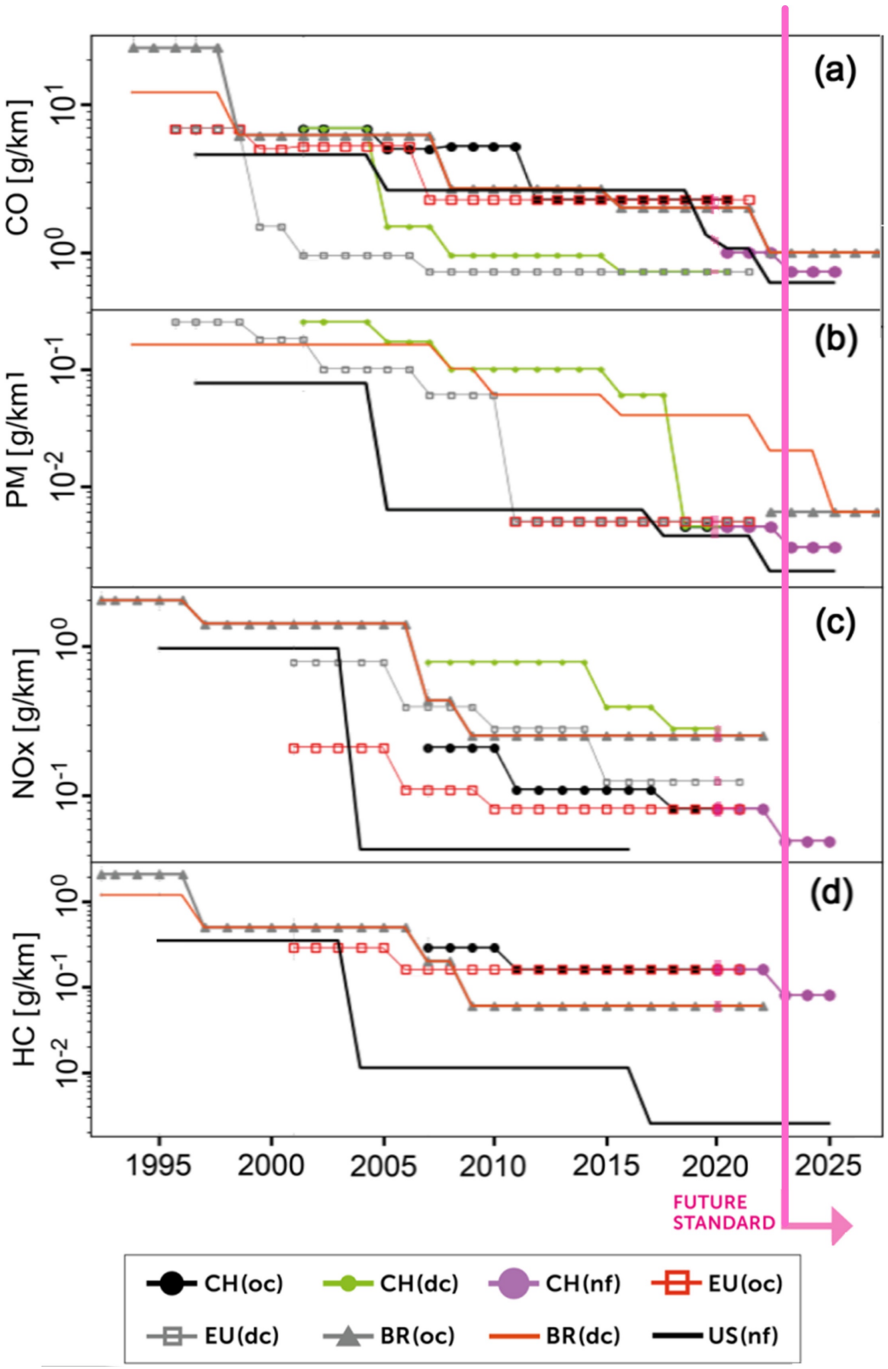

Figure 1.1: Exhaust emission standards of (a) CO, (b) PM, (c) NOx, and (d) HC for otto cycle (oc), diesel cycle (dc), and natural fuel (nf) on light duty commercial vehicles (LDCV) and light duty trucks (LDT) in the US, EU, China, and Brazil [1].

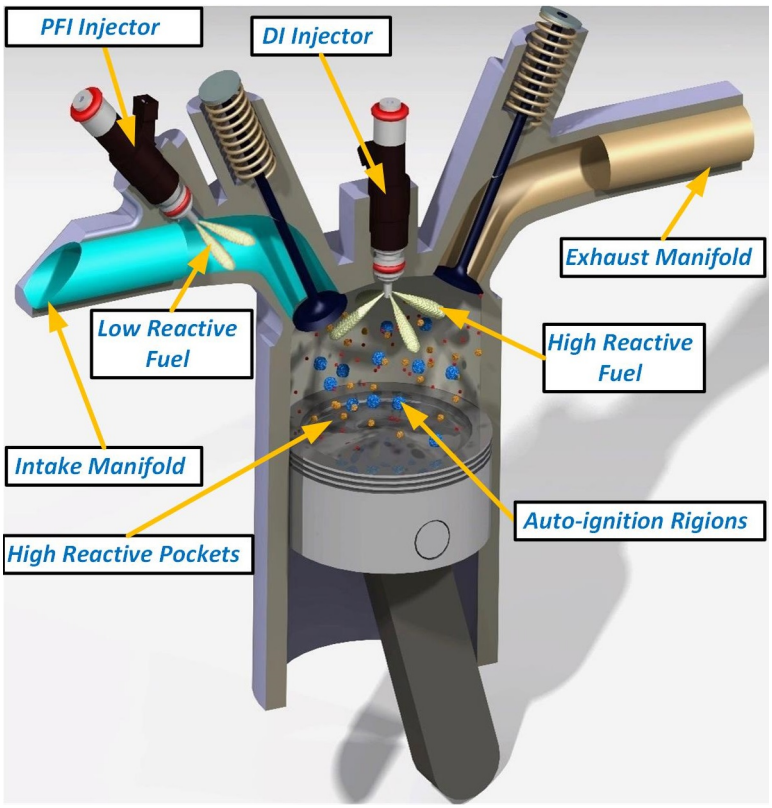

Figure 1.2: RCCI engine configuration

Fig. 1.2 shows RCCI engine configuration. It operates by port fuel injection of low reactive fuel and direct injection of high reactive fuel to the combustion chamber. High-reactivity fuel such as diesel is added in a cylinder advanced to TDC by a high-pressure direct injector to increase the reactivity of charge. Thermodynamic analysis of LTC combustion engines demonstrated their lower heat transfer and more effective conversion of thermal energy to work due to the lower temperatures are the main reasons for achieving higher efficiency. [13]. RCCI was initially proposed by Kokjohon et al. by optimizing dual fuel operation with port injection of gasoline and optimized direct multiple diesel injection [14]. Table (1.1) shows a comparison

of efficiency and major emissions between RCCI and conventional diesel combustion (CDC). It demonstrates that RCCI operation is a good option to meet new emission standard requirements for diesel operation.

Table 1.1
Light duty RCCI compared with conventional diesel operation [3].

	RCCI	**CDC**
BTE (%)	39.0%	36.4%
Soot (gr/kw-h)	0.05	0.23
NOx(ppm)	53	417
UHC(ppm)	3207	251
CO (ppm)	1099	140

Combustion phasing control is important for RCCI operation since it affects engine-out emission and brake thermal efficiency. A Study by Reitz et al. proposes optimal combustion phasing with CA50 around 8.5 bTDC [15]. Design of a control system that controls RCCI operation with available control means such as fuel mass, high/low reactive fuel ratio, and early direct injection timing would be essential to optimize RCCI operation. The goals for this control system can be considered as stable operation during transient operation, reducing cycle-to-cycle variations, avoiding misfire and too high maximum pressure rise rate, increasing thermal efficiency, controlling exhaust temperature, and further reduction in NOx and soot. Controlling RCCI combustion requires a good understanding of RCCI operation. RCCI operation can be studied through experimental tests and computational models such as computational fluid dynamics (CFD) coupled with chemical kinetics modeling

and multi-zone modeling. Multizone modeling is faster but they ignore charge motion inside the cylinder while CFD models are very detailed and provide detailed information but they are computationally expensive. Detailed CFD models of RCCI combustion coupled with engine experiments can provide valuable information on mixing, reaction, and the effect of several parameters on combustion. This can provide the controller with complete observation on the controlled engine which can be used to adjust control action. One of the main challenges facing controller design for RCCI engines is their highly nonlinear nature. The main reason for this nonlinearity is the strong nonlinear dependence of combustion rate on in-cylinder gas composition [16]. Therefore, all engine input parameters such as fuel quantity ratio and injection timing change cylinder composition and consequently exhibit a nonlinear behavior from the engine. This makes the real-time RCCI controller design complex. One way to handle this complexity is to utilize the linearization technique of linear parameter varying (LPV). LPV method presents nonlinear systems as parametrized linear systems whose parameters change with their state. LPV method substantially reduces modeling efforts by using experimental data to present a wide range of nonlinear RCCI engine operations as combined linear operations. Finally, derived linear models can be utilized in a model predictive control (MPC) framework to optimize RCCI operation, while considering actuators and states constraints.

1.2 Research objectives

This research has been motivated by RCCI engine potential to meet new emissions and improved fuel economy regulations. This study aims to address challenges in controlling combustion at RCCI engines. Its goal is to understand and model reactivity formation and stratification inside the combustion chamber as the driving force for RCCI combustion initiation and propagation. Moreover, the prediction of combustion chamber reacivity and stratification during steady-state and transient operation is another objective of this study which will completed by the development of a validated open-cycle computational fluid dynamic model for the RCCI engine. This study also looks to develop a fast and accurate control-oriented model for RCCI combustion and reduce combustion dynamic identification by implementing data-driven approaches. Utilization of the developed control-oriented models for RCCI combustion control is another goal of this study. The outcome of this work will be a robust constrained and unconstrained predictive controller that has good tracking performance for desired combustion timing and load at RCCI engines. Summary of research objectives are

❶ Development and validation of open cycle computaional fluid dynamic model for RCCI engine.

❷ Development of a fast and accurate reactivity and stratification model for dual fuel mixtures at engine relevant conditions.

❸ Development of high fidelity control-oriented model for RCCI combustion based on linear parameter varying strategy.

❹ Addressing state selection challenges for RCCI dynamic model using unknown state identification approach.

❺ Development of a constrained and unconstrained model predictive controller based on identified state-space dynamic models and testing performance of controller on actual RCCI engine

1.3 Literature Review

Previous research related to this work will be reviewed based on the research areas required to fulfill this work. They are grouped into RCCI engine modeling and experimental studies, RCCI control oriented model development and data-driven linear parameter varying modeling studies.

1.3.1 Review of RCCI Engine Investigations

Researchers have studied RCCI operation using computational and experimental methods to gain the required knowledge for improving it. For better clarification, the literature review for RCCI operation investigation is split into two sections modeling studies, and experimental studies. The literature review for RCCI operation is focused on works that provide insight useful for future control work. A summary of some of the major modeling and experimental RCCI studies is shown in Fig. 1.3.

1.3.1.1 Review of Modeling RCCI Investigations

RCCI operation modeling was initially started by Kokjohn et al. at the University of Wisconsin-Madison. It developed from Homogeneous Charged Compression Ignition (HCCI) and Premixed Charge Compression Ignition (PCCI) engine modeling. Kokjohn et al.[14] experimentally and numerically studied dual fuel HCCI and PCCI combustion. They controlled combustion in PCCI by means of varying fuel reactivity. The engine was modeled by coupling KIVA with the CHEMKIN code. They found that by port fuel injection of diesel fuel and early direct injection of diesel fuel, combustion phasing can be controlled at low and high loads. Using the model result they found that ignition points are coincident with the location of high

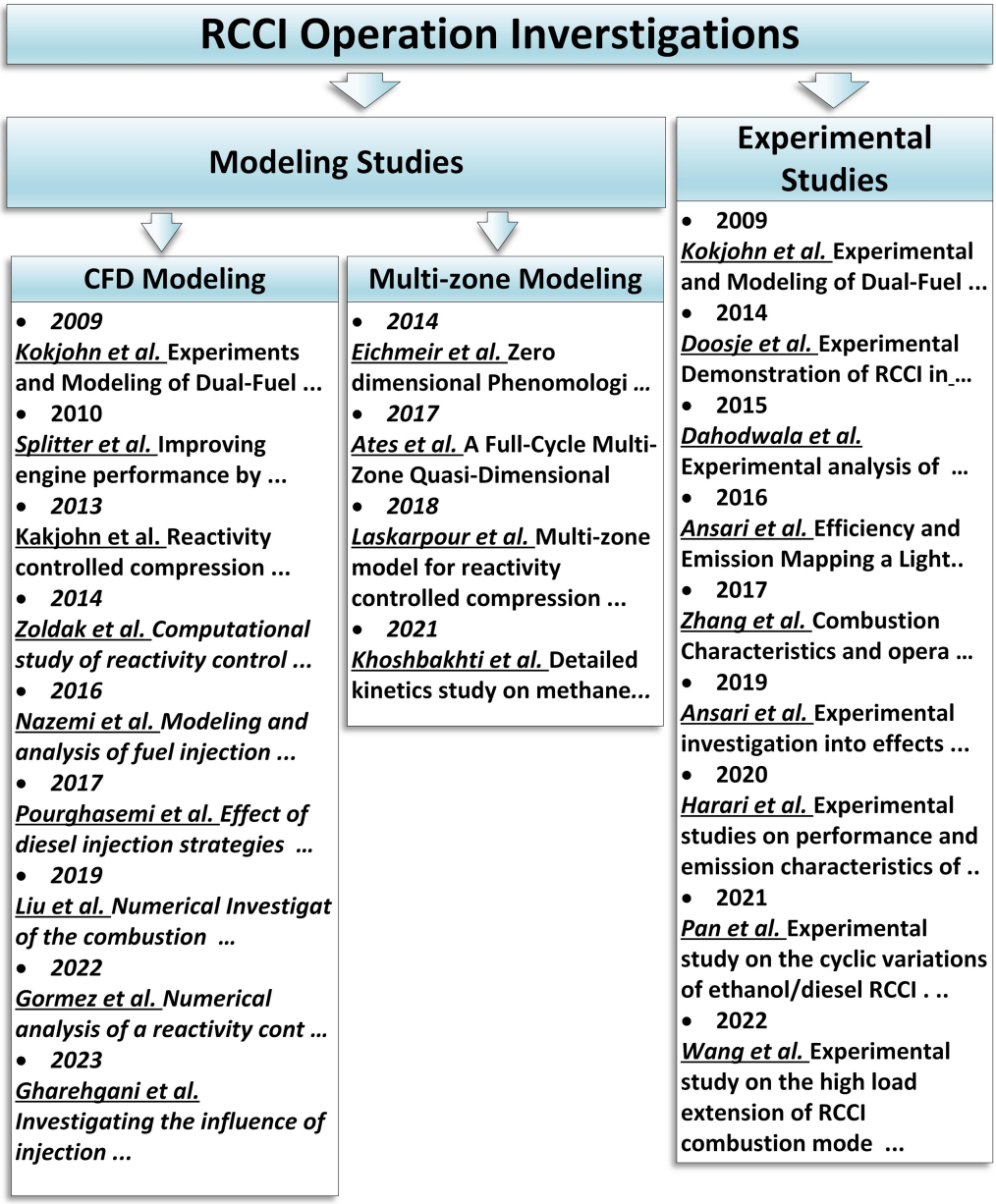

Figure 1.3: Sample of previous studies in RCCI operation

diesel concentration which formaldehyde was formed from low-temperature reactions. They reported dual fuel PCCI operation with NOx and soot well below heavy-duty limits.[17]

Splitter et al. [18] conducted a CFD modeling on fuel reactivity requirements for PCCI combustion. By modeling, they found that by increasing engine load, optimum combustion phasing does not require high reactive fuel. Moreover, this study showed that ethanol requires higher quantities of diesel fuel to maintain optimum combustion compared to diesel required for running gasoline. The main reason for this condition comes from lower reactivity and higher enthalpy of vaporization of ethanol compared to gasoline. In another study, Kokjohon [19] found that early diesel injection at dual fuel engines reduces high-pressure rise rates significantly. This research leads to the introduction of RCCI operation. RCCI operations were successfully run in load range from 1 bar BMEP until 9.5 bar BMEP [4, 15]. This range was limited by self-imposed restrictions on maximum pressure rise rate (MPRR)¡10 bar/deg , CO emissions less than 5000 ppm, and IMEP coefficient of variance (COV) less than 3%. Kokjohn and Reitz [20] compared conventional diesel combustion and RCCI combustion in a light-duty engine based on efficiency and NOx levels equivalent to US Tier 2 Bin 5. In this comparison, they assumed that CDC is using selective catalytic reduction to meet NOx constraints. Their research demonstrated that RCCI can meet Tier 2 Bin 5 cycle-averaged NOx targets without NOx after treatment. Moreover, they found that RCCI was 4% better in fuel consumption and 7.3% better in total fluid consumption (fuel + diesel exhaust fluid) compared to conventional diesel combustion with selective catalytic reduction. Hanson et al. [21] used KIVA to model RCCI combustion in a Light Duty engine and optimize the piston bowl. They found that

for constant compression ratio, increasing piston bowl radius and reducing bowel depth (to keep compression ratio constant) will increase gross indicated efficiency of RCCI operation. This is consistent with other research mentioning beneficial effects of large low curved bowl compared to a small high curved bowel. Hanson reported a 3% increase in efficiency compared to bowel designed for conventional diesel operation. Zoldak et al. [22] performed a computational CFD study on a heavy-duty RCCI engine running with natural gas and diesel. Their aim was to find tradeoffs of pollutant emissions, fuel consumption, peak cylinder pressure, and maximum pressure rise rate. They found that the RCCI combustion strategy had the potential to reduce NOx by 17.5%, soot by 78%, and fuel consumption by 24% compared to conventional diesel combustion. Their simulation found retarding diesel fuel. injection results in high soot emission and advancing diesel fuel results in premature combustion and loss of combustion control. Based on their simulation, they proposed double injection to maximize premixing diesel fuel and reduce soot emissions. They also proposed retarding the second injection to reduce maximum pressure rise rate and maximum pressure and NOx emissions. Nazemi and Shahbakhti [23] completed CFD combustion modeling of the RCCI engine in CONVERGE CFD and studied fuel injection parameters including spray angle, injection pressure, start of injection (SOI) timing, and premixed ratio (PR) on performance and emission characteristics in RCCI engine. Moreover, an extensive computational study was done to obtain optimum fuel injection parameters. They found that HC and CO emissions can decrease by

23% and 39% if spray angle 55, SOI = -53 aTDC, 580 bar injection pressure, and PR = 0.76 is used by the RCCI engine studied. Salahi et al. [24] simulated the RCCI engine with the goal of extending operating ranges by using prechamber. Their results show that pre-chamber can extend engine operating ranges to use lower intake temperatures such as 50 K lower in some cases. It can also increase the blending ratio by increasing natural gas and replacing diesel fuel. They found that using pre-chamber could result in incomplete combustion in low loads, but for higher engine loads pre-chamber results in better combustion. Li et al. [25] studied the effect of fuel chemical properties on combustion characteristics in RCCI engine using CFD study. They studied gasoline/diesel and methanol/diesel fuel combinations and found limits of RCCI operation for each case by considering fuel efficiency, RI (ringing intensity), and NOx emissions. Their work showed that methanol/diesel RCCI requires a more advanced CA50 to avoid excessive RI. They also found that methanol/diesel RCCI has higher fuel efficiency compared to gasoline/diesel RCCI because of the shortened combustion duration, reduced incomplete combustion, and lower heat transfer losses. Moreover, gasoline/diesel RCCI provides a more stable CA50 with smaller cyclic variations compared to methanol/diesel RCCI due to advanced CA50 and enhanced LTHR. In another study, Li et al.[26] conducted an energy and exergy study of CDC, HCCI, and RCCI engines. They found that exergy destruction has a close correlation with homogeneity of in-cylinder temperature and equivalence ratio during the combustion process, the combustion temperature, the chemical reaction rate, and

the combustion duration. Under the combined effect, HCCI and RCCI demonstrate lower exergy destruction than CDC at the same load. HCCI demonstrates the highest energy and exergy efficiency, and CDC performs the worst. Poorghasemi et al. [27] completed a CFD study on the effect of diesel injection strategies on light-duty RCCI engine. They studied the effect of the premixed ratio of NG, first and second start of injection (SOI) timing and fraction, injection pressure, and the spray angle on the engine performance and emission characteristics. Results show that by decreasing the first injection pressure from 450 to 300 bar, the gross indicated efficiency increases by 5%, and CA50 is retarded by 4 CAD. They also proposed that NOx emission can be reduced by means of increasing the NG fraction, advancing the SOI1, increasing the fuel fraction in the first DI injection with lower injection pressure, and employing a wider injector spray angle.

CFD modeling of the RCCI engine provided valuable information about the RCCI engine. However, these studies are time-consuming and expensive. To achieve fast simulation with acceptable simplification, multizone combustion modeling is a good option.

The first work done in RCCI multi-zone modeling was by Eichmeier et al.[28] They developed a phenomenological multi-zone model to predict the RCCI combustion which was validated against experimental and 3D-CFD data. Their multi-zone model was created from diesel particles and a homogeneous premixed mixture. Another

work in RCCI multi-zone modeling was done by Ates et al. [29] They completed a quasi-dimensional model for direct diesel injection and studied its combustion. They modeled spray and combustion events with up to six separate zones, representing different phenomenological sequences in the conceptual model. They used direct injection spray images obtained at Sandia to develop a quasi-dimensional model of a diesel engine. To summarize, the mentioned modeling studies show potential for improving the efficiency and emission of conventional diesel engines by implementing RCCI combustion mode. It also showed that RCCI can be optimized by controlling the input parameters of the engine. These modeling studies provide insights that are necessary in designing controllers and selecting desired values for RCCI engines.

1.3.1.2 Review of Experimental RCCI Studies

RCCI operation also has been experimentally studied. The first comprehensive experimental work was done by Kokjohn et. al. [14] They investigated dual fuel operation of gasoline diesel at two high loads, 6 and 11 bar IMEP operation. This experimental study demonstrated the advantages of an operation that was later named RCCI to meet US 2010 heavy-duty emissions regulations. They found that at the 11 bar operating point, NOx and soot were 0.01 g/kW-hr and 0.008 g/kW-hr, respectively. This study showed that RCCI operation can easily meet regulation limits after treatment while achieving 50% thermal efficiency. Doosje et al. [30]

completed another experimental study on heavy duty natural gas/diesel RCCI engine. They showed that RCCI operation has low emissions for NOx and PM at a range up to 10 bar IMEP. Their work shows that very advanced SOI results in very large variation for maximum pressure. Jia and Denbratt [31] experimentally studied the effect of diesel injection split and compression ratio in a heavy-duty RCCI engine performance and emissions. They varied the injection timing and duration of the first and second injections. They found the amount of fuel in the second injection could be reduced considerably smaller than the first injection without affecting the performance. They conclude that to increase the blending ratio, it is better to keep the first injection duration constant decrease the second injection duration, and replace diesel fuel with natural gas. Considering the effect of compression ratio, they found reducing the compression ratio from 17 to 14, improves indicated thermal efficiency but it has a negative effect on UHC emissions. Dahodwala et al.[32] studied the effect of adding natural gas to conventional heavy-duty diesel operation engines and its limitations. They found that replacing diesel with CNG is limited by high UHC levels, combustion instability, peak cylinder pressure, and exhaust gas temperature. They also conducted optimization on diesel injection timing and CNG substitution. They reported that low-load RCCI enables even higher CNG substitution and lower emissions. They observed a maximum of 50% net indicated thermal efficiency at 6 bar BMEP load point along with 75% reduction in both NOx and PM emissions. In another study, Dahodwala et al. [33] conducted another experimental study on RCCI

engines. They studied the effect of several control inputs such as CNG substitution, EGR rate, and injection strategy on RCCI combustion at 6 bar BMEP. They found that burn duration increased by increasing the amount of natural gas which resulted in delayed combustion phasing. Increasing natural gas is limited by higher THC and CO emissions although a more favorable CA50 could be achieved. They also found that the EGR rate can be used as a control variable for adjusting combustion phasing and burn duration. Increasing the EGR rate delayed combustion phasing and increased the combustion duration. Higher EGR rates result in higher thermal efficiency and therefore better fuel conversion efficiency was observed. Considering split injection, a higher injection quantity in the second injection results in advanced combustion phasing because late injection of a higher quantity of diesel fuel leads to an insufficiently mixed charge. Hanson [34] experimentally studied a light duty RCCI engine at transient operation. They compared the efficiency and emission of light-duty gasoline diesel RCCI engines with CDC during up speed and down speed. They used optimized intake conditions for the RCCI engine. They found that the emission behavior of RCCI engine at transient condition is similar to steady state condition RCCI engines has lower PM and NOx and higher UHC compared to CDC. Hanson et al. completed another experimental study on the effect of EGR on heavy-duty natural gas diesel RCCI engine [35]. They found that EGR results in lower combustion noise and 48% lower averaged NOx. However, the brake thermal efficiency of the RCCI engine decreased by 0.5, and soot emission increased slightly. They concluded that

EGR can reduce fluid consumption at a selective catalyst reduction system. They also found that EGR reduces CO and HC emissions of RCCI engines. A similar study was performed by Kalsi et. al. [36] and they reported similar trends for emissions. However, their experimental test reported brake thermal efficiency to be constant until 15% EGR addition.

These works completed in the experimental RCCI study was on heavy-duty RCCI engine. Ansari et al.[4] studied the light-duty operation of an RCCI engine with NG/diesel for the first time. They investigated brake thermal efficiencies, emissions, and combustion characteristics of a light-duty 1.9L, four-cylinder diesel engine operating in single-fuel diesel mode and in NG-diesel RCCI mode. They found that at low loads, the RCCI operating mode provided the same brake thermal efficiency (BTE) values as diesel or worse. Moreover, they noticed that the BTE of light-duty RCCI engines improves by increasing the engine speed and load. BTE reached to 39% for RCCI mode at 2500 RPM and 6 bar BMEP while BTE at complete diesel combustion (CDC) mode was 34% at the same condition. This work once again demonstrated the advantage of RCCI over CDC.

1.3.2 Review of control-oriented RCCI Engine modeling and combustion control

Researchers have been studying the development of control-oriented models and combustion controller design. A number of studies are found in control of combustion phasing in HCCI engines [37, 38, 39, 40, 41], but few studies are found in the literature for RCCI combustion control initial stages of this study. Figure 1.4 summarizes prior works on RCCI combustion controller design when this research was started. These works fall into two categories based on the platform for controller implementation and testing. The first category designed RCCI controllers which used high-fidelity RCCI models to verify controller performance, while the second category includes controllers which are validated on a real RCCI engine for controller validation.

Among simulation studies, Wu et al. [42] conducted the first RCCI combustion control based on a rule-based control design. They studied load transitions on a validated CFD model of an RCCI engine to investigate CA50 trends and developed a control strategy based on adjusting the PFI to DI fuel ratio. They found that during load-up transitions, CA50 was delayed by 7 to 15 CAD which was countered by decreasing PFI to DI fuel ratio by 10% to 15% for their simulated RCCI engine conditions. During load-down transitions, CA50 was observed to be advanced by 5 CAD which was compensated by increasing PFI to DI fuel ratio by 40% to 44%. They

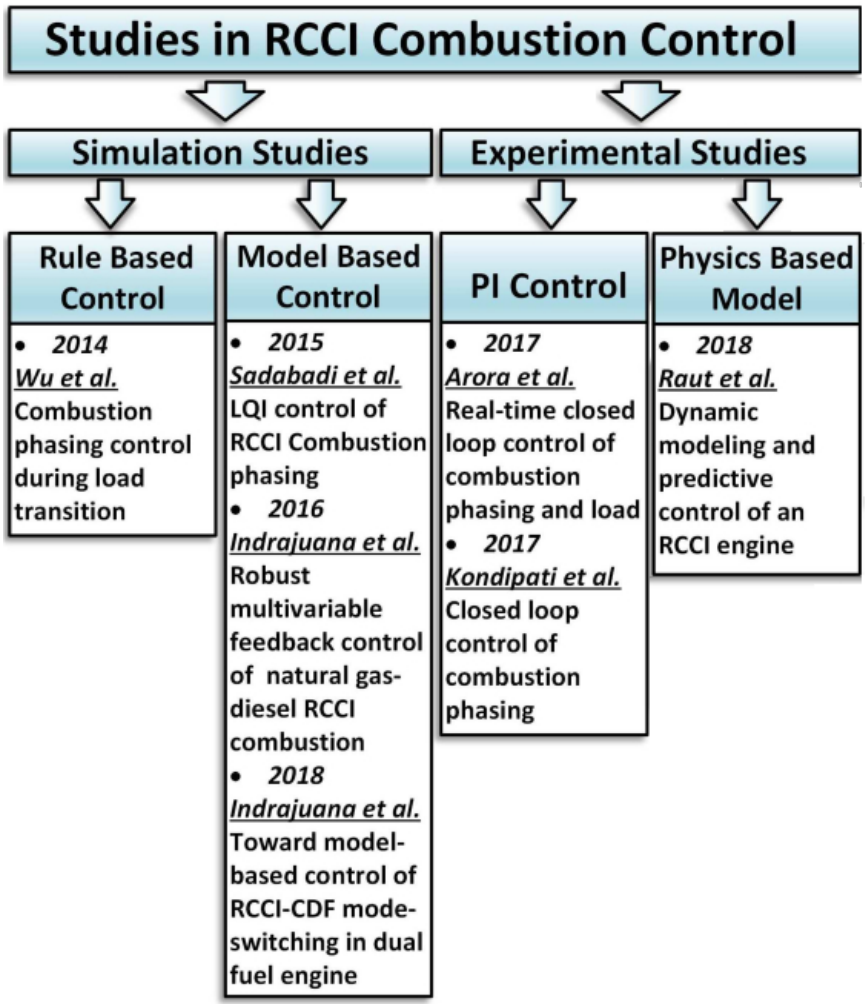

Figure 1.4: Summary of previous studies in RCCI combustion control

used an offline map to design a feedforward steady-state controller. Lack of online feedback caused an adverse effect on controller performance during transient RCCI operations. Sadabadi et al. [43] developed the first validated physics-based control-oriented model for RCCI combustion. The model in reference [43] could predict the start of combustion, burn duration, and CA50 with an average error of 2 CAD. In another simulation-based research, Indrajuana et al. [44] formed a function for ignition delay (τ_{id}), indicated mean effective pressure (IMEP), and premixed ratio

(PR) of a validated RCCI engine model that ran with diesel and natural gas fuels. Their function was dependent on diesel fuel start of injection (SOI), and diesel and natural gas fuel flow rates. They linearized this function and formed a multiple-input and multiple-output (MIMO) proportional controller to control τ_{id}, IMEP, and PR on a multi-zone model. Their results showed successful tracking of desired values within 5 engine cycles. The latter work [44] was the first study to use chemical kinetics to develop an RCCI combustion controller. Recently, Indrajuana et al. [45] developed a new controller for switching from conventional dual fuel (CDF) operation to RCCI operation. They used an RCCI engine model and proposed a model-based controller for switching from CDF to RCCI operation. Their simulation results indicated that RCCI operation can be controlled by adjusting air and fuel path flows.

Figure 1.4 also lists the second category of studies that include RCCI controller implementation on an engine experimental setup. As the first work in this category, Arora et al. [46] designed and implemented the first real-time transient combustion phasing and load controller for an RCCI engine. They developed two PI controllers to adjust CA50 and IMEP using real-time combustion phasing and IMEP calculation from a designed field programmable gate array (FPGA). For the CA50 control, they used a sensitivity map to choose between SOI and PR as the control variables. For IMEP control, fuel quantity was used as the control variable which was adjusted by a combined feedback and feedforward controller. Based on their experimental tests on the RCCI engine, the combustion controller was able to control CA50 at desired

values during load changes. The IMEP controller was also capable of reaching desired values within 2-4 engine cycles. In another study, Kondipati et al. [47] developed a PI controller for an RCCI engine and used a physics-based model to tune the PI controller. The tuned PI controller was tested on a real RCCI testbed for real-time combustion phasing control. Their experimental results proved the controller's capability to reach the desired CA50 in 2-3 cycles with an average tracking error of 1 CAD. In another study, Raut et al. [48],[49] designed and implemented the first online MPC on an RCCI engine based on a physics-based control-oriented model. Their controller was designed as a switched MPC controller based on PR values to extend controller range and used 5 engine cycles as prediction horizon to calculate optimal control variable. The MPC controller used SOI and FQ as control variables and was able to control CA50 with 1 CAD and IMEP with 19.6 kPa average tracking error, respectively.

1.3.3 Review of data-driven linear parameter varying identification

The linear parameter varying method deals with identifying nonlinear systems by describing them as parameterized linear systems with time-dependent parameters. In LPV control design, the goal is to design a global controller to satisfy stability and performance over the entire set of possible parameter values. This is the main

advantage of the LPV method to gain scheduling method which controls operating range by patching many controllers without guaranteeing stability over the entire range of operation[50].

The Linear parameter varying method originates in the gain scheduling control method [51]. The research community initially addressed the gain scheduling in the 1990s [52]. LPV method initially introduced by Shamma and Athans works [53, 54]. They introduced LPV models as linear state space models whose matrices depend on time-varying parameters. Therefore, the dynamics of LPV systems are linear but time-varying. They proposed considering the dynamic of the time-varying parameter as an exogenous independent parameter instead of modeling it. These two pieces of research formed the basis of LPV modeling.

Literature on LPV control and LPV identification have started growing in parallel from the beginning of the 1900s. The first attempt to solve the problem of LPV identification is related to a paper by Nemani [55]. which was based on state space and solving linear-fractional transformation (LFT) system identification problems. Lovera et al.[56] considered linear state space measurement of the LFT LPV system with a single time-varying block and Lee and Poolla [57] addressed the problem of identifying a discrete LPV model with an LFT structure. Previdi and lovera considered identifying LPV models with hybrid linear/nonlinear procedure [58]. The nonlinear part is identified through a neural network and the linear part is identified

through a least square algorithm. Finally, Bamieh and Giarre [59] solved the problem of identifying discrete-time LPV models of nonlinear time-varying systems of inputs, outputs, and the scheduling parameters are measured and a form of functional dependence of the coefficients on parameters is known. They showed how the identification problems can be reduced to linear regression so that a least mean square and recursive least square identification algorithm can be used. These works formed the science of modeling dynamic nonlinear systems by LPV modeling method.

On the application side, the LPV method found utility in many fields such as automotive, robotics, aerospace, traffic control, and web service systems. In this proposal, the literature review on the application of LPV will be confined to automotive applications, especially internal combustion engines. One of the initial applications of the LPV method in the automotive area was done by Gaspar [60]. They worked on applying the LPV method for modeling and control of an active suspension system and used three scheduling parameters which were linked to the load pressure of the hydraulic actuator, relative velocity, and relative displacement. They successfully designed a controller to handle the nonlinearities of the suspension system with the goal of minimizing vertical acceleration in case of small suspension travel and minimizing suspension deflection in case of large suspension travel. PoussotVassal et al. [61] worked on the same issue and reviewed some semi-active suspension control strategy's performance. One of the studied control strategies was the polytrophic-based linear parameter varying method. They conclude that the LPV-based control

strategy provides greater robustness compared to other methods. It also provides great flexibility in comfort and road handling performance. Gaspar et al. [62] and Szabó et al. [63] also used the LPV method to design global chassis control for controlling chassis altitude.

In the internal combustion engines, the LPV method found good application to address high nonlinearities in these engines. Wei et al [64] proposed data based linear parameter varying model of the air path system of diesel engine and used H_∞ technique for designing a controller for EGR regulation. They found that the designed LPV-based controller has better tracking performance compared to the standard production control unit without the need for calibration. They conclude that using LPV modeling and control is a promising approach for engine control. Jung et al. [65] performed a similar study on the air path of turbocharged diesel engines using the LPV method and considering intake manifold air pressure as a scheduling parameter. Their aim was controlling air mass flow and EGR. They highlighted the significant reduction in calibration efforts by using the LPV method and its surprising performance. Genc [66] worked to design robust control variable cam timing engines using linear parameter varying modeling. He developed an LPV model for air-fuel ratio (AFR) control in a gasoline port fuel-injected engine. He used LFT to approximate the developed AFR model which was used to develop the LPV controller. The experimental results of the controller showed that the LPV controller provides up to 50% better regulation on AFR compared to the LTI controller. White

[67] studied LPV controller design for internal combustion engines in his PhD studies. He applied the LPV method to air-fuel ratio control of port fuel injection systems and control of hydraulic and variable valve timing systems. His results on the engine show that LFT representation LPV systems have advantages for real-time implementation due to computational works and LFT/LPV controllers offer significant improvement in AFR regulation. Gauthier et al. developed a model for diesel engine common rail injection system [68]. which was used to design an LPV-based controller for diesel engine common rail injection system [69, 70]. The works mentioned above are some of the investigations related to LPV application in literature. To the best of the author's knowledge, there was no work in the literature for LPV modeling of the RCCI engine during the initial stages of this research.

1.3.4 Review of reactivity and stratification modeling

In this study, chemical reactivity is modeled using a data-driven approach. Chemical reactivity is the tendency of reacting substances to transform into reaction products. Ra et. al. ([71]) created a relative reactivity index for engine use. They established an inverse relationship relating reactivity and ignition delay (ID) and evaluated the ignition delay in a constant volume container for stoichiometric blends of primary reference fuels at 40 bar and 850 K. Later, the reactivity formula was tuned to equal the cetane number of different fuels. Jamali et al. ([72]) later used this concept

of reactivity to describe the reactivity of fuel blends. They described the reactivity of a fuel blend as the mass fraction-based average of the reactivity of every fuel component. These studies solely calibrated the defined relative reactivity index for ignition delays under fixed initial temperature and chemical settings. Because the initial temperature, pressure, and composition have a substantial impact on the ignition delay, it is needed to create a new reactivity metric for engine-relevant situations with varying thermal and chemical conditions. This study is trying to fill this gap. In this paper, complicated and highly nonlinear chemical kinetics are modeled, and reactivity is represented as a function of chemical and thermal settings that are pertinent to internal combustion engines. The dynamic state space reactivity model is later created by first creating a kernel canonical correlation analysis model and then training it using the modeled reactivity levels.

Stratification is the other study parameter that has been examined in this research. Modeling stratification is a difficult problem because of the complicated turbulent flow of injected fuel, intake airflow, and interaction of these fluxes. Researchers examined stratification within the combustion chamber and sought to understand how it affected both efficiency and emission. The majority of this research used brightness intensity imaging to detect stratification and used several methods to calculate the level of stratification. Yin et. al. ([73]) calculated stratification by dividing the maximum intensity across all regions by the intensity differential between adjacent regions. According to Vedharajet. al. ([74]) definition, stratification is the product

of a region's maximum and least intensity divided by their sum.

1.4 Limitations in state-of-the-art

Based on the review of literature review presented in the previous section, it can be understood that there are certain limitations in the current state-of-the-art for control-oriented combustion control of RCCI engines. These limitations are summarized as:

❶ Obtaining accurate and fast physics based control oriented model for RCCI engine phenomena is difficult and time consuming .

❷ Representing mixture reactivity for all engine relevant conditions using single formula is challanging.

❸ Determination of most effective states at RCCI engine's combustion dynamics is not easy.

❹ Computational Fluid Dynamics model of RCCI engine is computationally expensive and is not suitable for transient modeling investigation.

1.5 Contributions of this thesis

1.5.1 Development of a data-driven control-oriented RCCI model

Most of the studies about RCCI control-oriented combustion model development and implementation were conducted using a physics based modeling approach. While the physics-based approach is powerful, it requires accurate, control-oriented models which are hard, and time-consuming to develop. In this situation, data-driven modeling (DDM) approaches can be offered as an alternative. Data-driven approaches do not require a thorough knowledge of the underlying physics and can be developed based on available measured data and initial information about involved variables, internal states, and system structure [75]. Given the complexity and highly nonlinear nature of RCCI combustion, the DDM approach can be used to reduce model development costs for RCCI engine control. This paper will develop a new DDM for RCCI engine identification and will utilize the data-driven models in an MPC framework. While the DDM approach can be adapted using methods such as artificial neural networks (ANN), fuzzy rule-based systems (FRBS), and genetic algorithms (GA), our work uses support vector machine (SVM) as a model learning strategy. SVM is based on an extension of line (or surface) identification for separating two

classes of objects and can be extended to solving prediction problems. In this research, SVM is selected based on its predictive capacity [76]. Here, an SVM-based DDM is developed to identify linear parameter-varying (LPV) models for RCCI combustion control. The LPV platform is selected due to its capability to (i) simplify nonlinear RCCI dynamics into an array of linear models characterized by scheduling variables, and (ii) guarantee the stability of the controller for broad engine operations.

To the best of the authors' knowledge, this study was the first study undertaken to develop a data-driven LPV model to capture RCCI nonlinear dynamics by an easily implementable data-driven LPV model.

1.5.2 Development of a data-driven control-oriented MPRR model

Development and implementation of data-driven combustion phasing controller for RCCI engines encouraged to continue data-driven modeling approach to model and control maximum pressure rise rate (MPRR) at RCCI engines which is one of the contraining factors in expanding RCCI operation to high loads. High MPRR occurs at high loads due to the formation of multiple simultaneous auto-ignitions at multiple regions inside the combustion chamber. This issue generates high heat release rates and results in high MPRR values which are perceived by high combustion noise and high ringing intensity (RI). High MPRR restricts the high load operation range in

RCCI engines. This study addresses the high-load MPRR challenge and presents two control-oriented MPRR models for controlling MPRR at high loads. Several studies have been conducted to learn effective factors in reducing MPRR and expanding the high load range in RCCI engines. Zoldak et. al. [22] studied MPRR and a couple of other combustion parameters in an RCCI engine by a CFD model. They found that increasing the in-cylinder reactivity gradient with a late injection of high reactive fuel will limit MPRR in RCCI engines. This approach should be implemented cautiously due to the chance of incomplete combustion at a highly stratified charge. [77]. Hanson et. al. [78] found another method to control MPRR while researching the effects of biofuel blends on RCCI combustion. They found that MPRR can be reduced by decreasing DI fraction and decreasing PFI fuel reactivity level. These studies can only be used to design a passive controller by avoiding operational conditions that are prone to generate high MPRR. Active control of MPRR in RCCI requires a control-oriented MPRR model and a closed-loop control strategy which is addressed in this study.

Fig. 1.5 presents contributions of this section of research for RCCI combustion control studies. This study presents a study to model real RCCI engine MPRR via a data-driven KCCA-LPV model. To the best of the authors' knowledge, this research presents the first study to develop a data-driven KCCA-LPV MPRR model based on experimental MPRR data obtained from a real RCCI engine. Moreover, Fig. 1.5 presents a few additional new studies. One of these studies was conducted by Kakoee

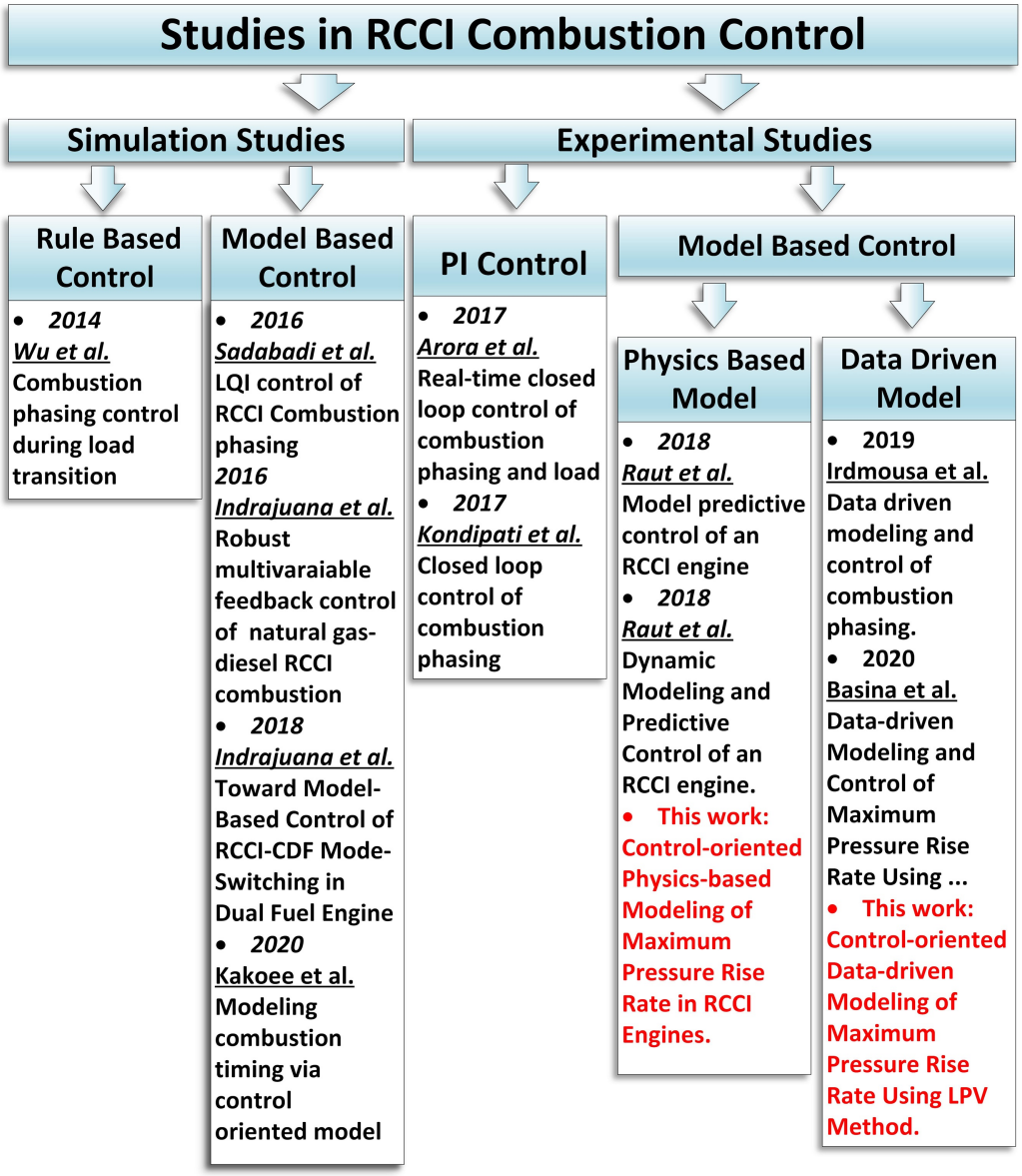

Figure 1.5: Summary of previous studies in RCCI combustion control and contributions of MPRR study highlighted in red.

et al. [79]. They developed a physics-based control-oriented model of an RCCI engine and used it to study the combustion timing of an RCCI engine. In another study, Sui et al. [80] developed a calibrated mean value combustion phasing model for a dual-fuel engine and implemented an adaptive closed-loop and an open-loop controller

to control combustion phasing. Basina et al. [81] also developed a physics-based model to predict MPRR in RCCI engines and used it to design a closed-loop MPRR controller at transient operations.

1.5.3 Development of an unknown states control-oriented RCCI combustion model and constrained MPC

These researchers used a known-states data-driven approach where the knowledge for selecting RCCI states is required and the structure of the RCCI model needs to be known. Due to the complexity of RCCI combustion, the optimal selection of relevant states to represent RCCI combustion dynamics is challenging. This issue is addressed in the current research and a novel Kernelized Canonical Correlation Analysis (KCCA) approach is implemented to develop a data-driven RCCI dynamic model based on unknown plant states. This approach automatically sets engine states based on experimental input-output data from the engine to identify a state-space LPV model. Moreover, this section of research developed a constrained MIMO MPC controller for combustion timing and IMEP control. To the best knowledge of the authors, this section of the study presents (i) the first RCCI combustion identification based on an input-output approach with an unknown model structure. (ii) the first constrained MPC controller design and implementation for an RCCI combustion. Contributions from this section of the study is highlighted in Fig. (1.6)

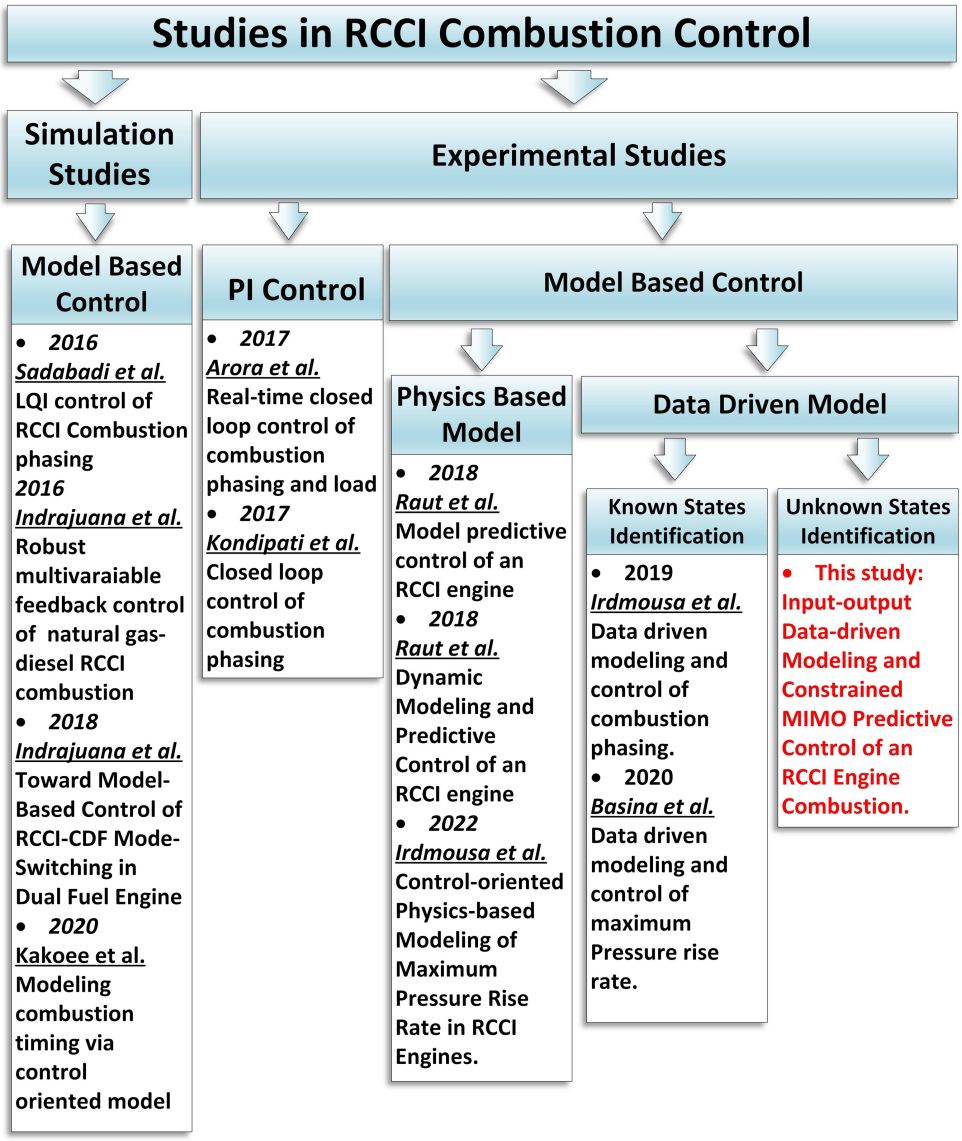

Figure 1.6: Summary of previous researches in RCCI combustion control and this research contribution highlighted in red.

1.5.4 Development of a data-driven reactivity and stratification dynamics model

These studies on control-oriented combustion model development for RCCI engines used experimentally measurable characteristics as the states for building the dynamic combustion model. This research added a novel approach to combustion dynamic identification and defined chemical reactivity and fuel stratification as new combustion dynamic states. Chemical reactivity is defined as the tendency of reacting materials to convert to reaction products. This conversion happens through the formation of hundreds of intermediate chemical compounds which interact through thousands of elementary reactions. This complex interaction between intermediate chemical compounds determines the direction of a reaction. High reactive mixture forms when the generation and consumption of intermediate compounds lead to the fast consumption of reacting materials and the creation of products. On the other hand, low reactive mixture's intermediate compounds regenerate the consumed starting materials and consequently slow the progress of conversion of starting materials to the products. Ra et. al ([71]) developed a relative reactivity index for engine applications. They defined an inverse correlation between reactivity and ignition delay (ID) and measured the ignition delay for a stoichiometric mixture of primary reference fuels at 40 bar and 850 K in a constant volume chamber. The reactivity equation was later

calibrated to match the cetane number of fuels. This defined reactivity was later used by Jamali et. al ([72])to define the reactivity of a mixture of fuels. They defined fuel mixture reactivity as mass fraction based average of and relative reactivity of each fuel. The defined relative reactivity index in these studies was only calibrated for ignition delays at fixed initial thermal and composition conditions. Since initial temperature, pressure, and composition has a significant effect on ignition delay, a new reactivity metric is necessary to be developed for engine-relevant condition with variable thermal and composition conditions. This study is addressing this need. In this study, a data-driven approach is used to model complex and highly nonlinear chemical kinetics and represent reactivity as a function of engine-relevant chemical and thermal conditions. Modeled reactivity levels are later used for training the Linear Parameter Varying (LPV) model to form a dynamic state-space reactivity model.

Stratification is the other studied parameter of this research. Stratification is determined by the mixing process between injected fuel and air. It depends on fuel injector characteristics and flow dynamics through the intake manifold and combustion chamber. Due to the complex turbulent flow of injected fuel, intake airflow, and interaction of these flows, modeling stratification is a complex task. Researchers evaluated stratification inside the combustion chamber and tried to find the effect of stratification on efficiency as well as the emission. Most of these studies measured stratification using luminosity intensity imaging and proposed different

formulas to quantify stratification levels. Yin et. al ([73]) quantified stratification based on the difference of intensity between adjacent regions divided by maximum intensity among all regions. Vedharajet. al ([74]) defined stratification as the sum of maximum and minimum intensity at a region divided by subtraction of them. In this study, a CFD model is developed to obtain fuel mass fraction distribution inside the combustion chamber. Stratification is defined based on the difference between the fuel mass fraction at each cell and the homogeneous fuel mass fraction. Later, a data-driven model is used to model the dynamics of stratification. Contributions from this section of the study are highlighted in Fig. (1.7). To the best of the authors' knowledge, this is the first study to present a data-driven dynamic state space model for reactivity and stratification at an internal combustion engine for the control applications. This study implemented its modeling approach on an RCCI since reactivity and stratification play a major role in its combustion initiation and propagation.

To summarize, this study focused on the development of fast and reliable control-oriented combustion models for RCCI engines. To accomplish this goal, it relies on two data-driven identification approaches based on known and unknown states. Identification and modeling results are tested by the development of a model predictive controller strategy and implementation on an actual RCCI engine or high-fidelity RCCI engine model. This process will be explained in detail in the following chapters.

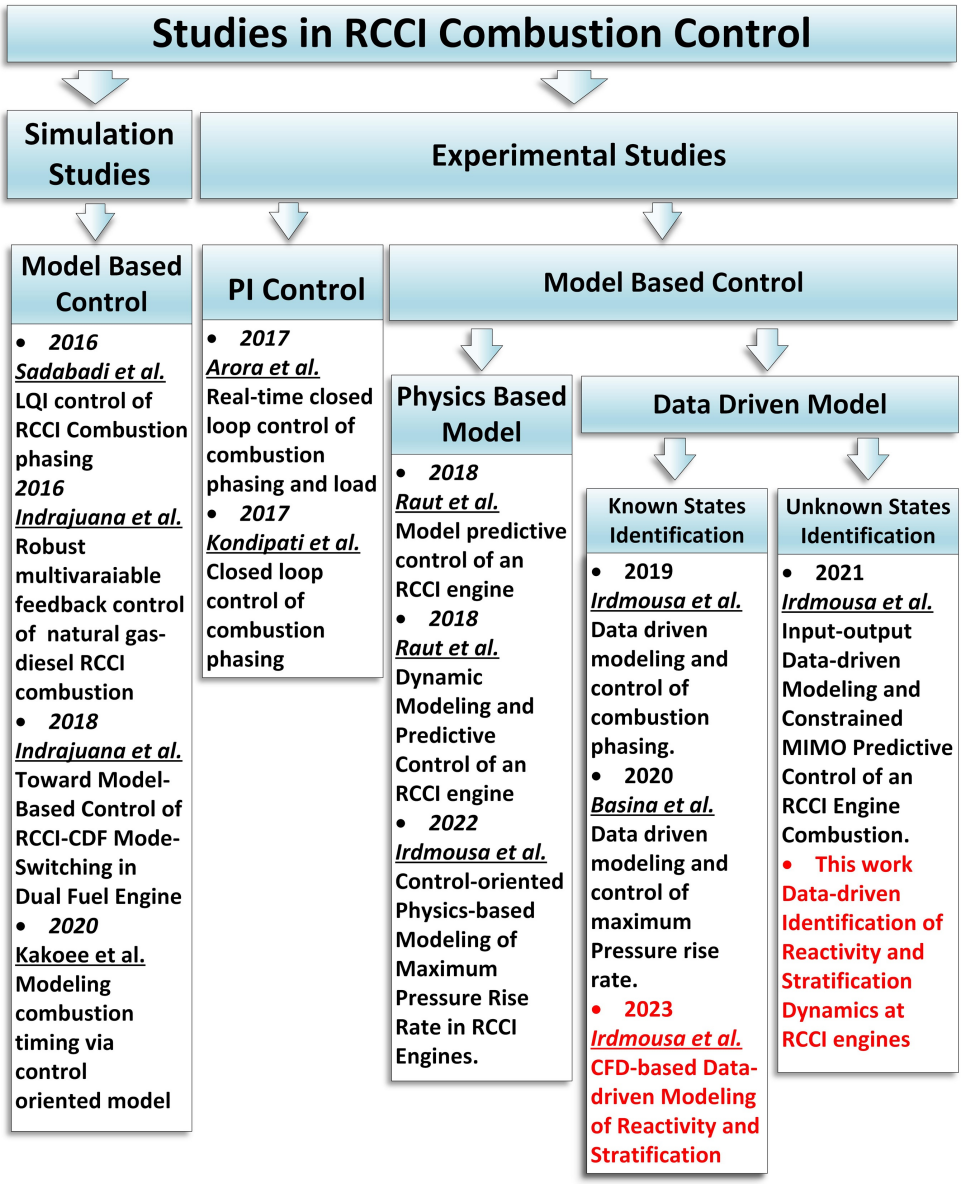

Figure 1.7: Summary of previous researches in RCCI combustion control and this research contribution highlighted in red.

1.6 Thesis Structure

This thesis is organized as follows:

Chapter 2 presents the identification of combustion dynamics for a reactivity-controlled compression ignition engine based on experimental data collected from the RCCI engine at the Energy Mechatronics (EML) Lab. The identified dynamics model used in the model predictive controller strategy. This chapter explains the implementation of the developed MPC controller to control crank angle for 50% of fuel burnt at an actual RCCI engine and controller results.

Chapter 3 uses an input-output-based approach to model RCCI combustion dynamics without requiring any state definition. This chapter also includes including identified input-output-based dynamic model at a constrained model predictive control strategy and the development of a MIMO controller to control combustion phasing and load at an RCCI engine.

Chapter 4 demonstrates the development physics-based and data-driven model for the maximum pressure rise rate model through using transient data from an RCCI engine. Control-oriented data-driven and Physics-Based Modeling of Maximum Pressure Rise Rate in Reactivity Controlled Compression Ignition Engines.

Chapter 5 presents the development of an open-cycle computational fluid dynamics model for the RCCI engine at EML Lab. Validation results of the CFD model based on steady-state and transient experimental data are also presented. Moreover, this chapter explains the reactivity index and stratification index development for engine-relevant conditions and dual fuel mixtures. Then two data-driven models

based on linear parameter varying method and input-output based Kernel Canonical Correlation Analysis (KCCA) methods are used to generate a data-driven chemical reactivity and stratification models for the RCCI engine.

1.7 Experimental Setup

Fig. 1.8 presents the layout for the experimental RCCI engine test bench in this work. A GM 2.0L Ecotec turbocharged Gasoline Direct Engine (GDI) was modified to run in RCCI mode. Engine specifications are listed in Table 1.2. During engine modification, low pressure fuel rail and port fuel injectors were added at intake ports to enable RCCI mode operation. *Iso*-octane is injected into intake ports as low reactive fuel and *n*-heptane is injected as high reactive fuel directly into the combustion chamber. Premixed ratio (PR) is defined as the ratio between low reactive fuel and high reactive fuel. It is defined according to Eq. (1.1) based on chemical energy from the low reactive fuel divided by the total chemical energy delivered by both fuels.

$$PR = \frac{m_{iso} LHV_{iso}}{m_{iso} LHV_{iso} + m_{nhep} LHV_{nhep}}, \tag{1.1}$$

where, LHV_{iso} represents lower heating value of *iso*-octane and LHV_{nhep} represents lower heating value of *n*-heptane. A controllable air heater was included at

intake air flow path to adjust intake air temperature for RCCI operation. The engine is coupled with an 460 AC hp dynamometer. A dSPACE MicroAutoBox (MABX) unit is programmed and used as the engine control unit (ECU). In addition, dSPACE RapidPro was used as power stage for actuators and signal conditioning for sensors. In-cylinder pressure is measured by PCB piezoelectric pressure transducer. A Spartan-6 field FPGA was programmed in Xilinx to use real-time pressure data to compute CA50, and IMEP to provide feedback to the ECU.

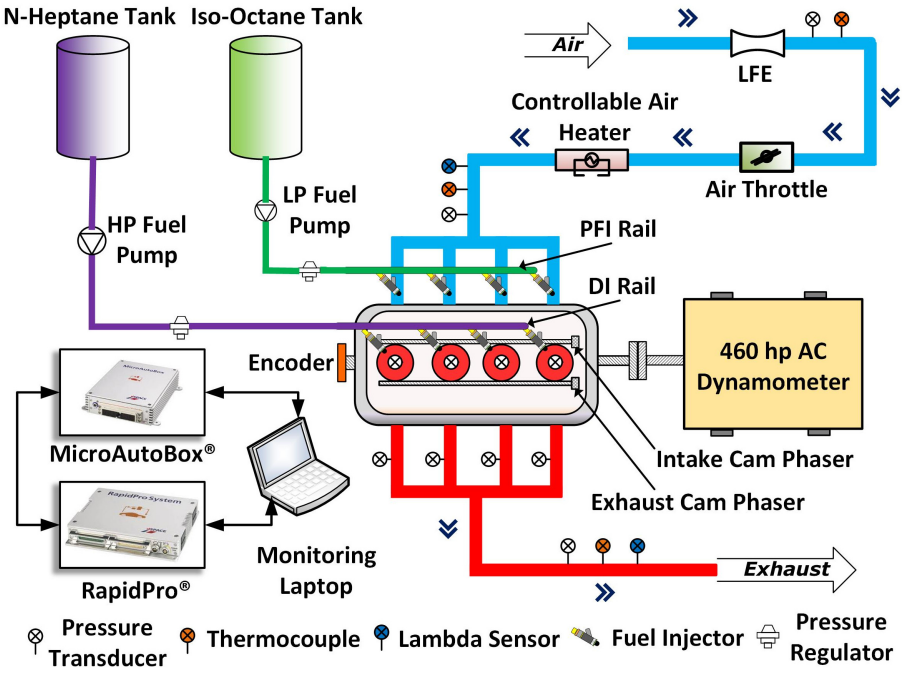

Figure 1.8: RCCI engine experimental layout

Figure 1.9 shows the RCCI experimental setup that includes a gasoline tank used to run the engine at SI mode prior to switching to RCCI mode.

Two sets of experiments were conducted in this research. First set of experiments

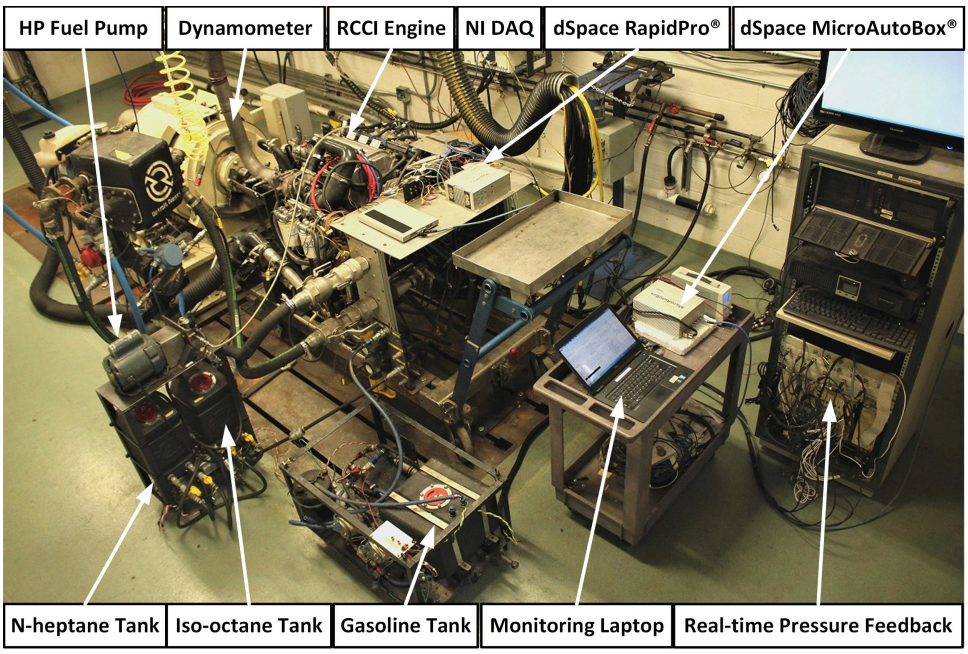

Figure 1.9: Real RCCI engine Overview

Description [Unit]	Operating Value
Bore [cm] × Stroke [cm]	8.6 × 8.6
Compression ratio	9.2:1
Displacement volume [cc]	1998
Max engine power [kW@rpm]	164@5300
Max engine torque [Nm@rpm]	353@2400
IVO, IVC [CAD bTDC]	25.5, 2
EVO, EVC [CAD bTDC]	36, 22
DI fuel rail pressure [bar]	100
PFI fuel rail pressure [bar]	3

Table 1.2
RCCI Engine Specification

were carried out to obtain training and test data for state space (SS) identification of the RCCI LPV model. In these identification experiments, fuel quantity (FQ) was defined as the scheduling variable since it is the main control variable to adjust engine load (IMEP). Thus, changing FQ leads to changing the engine load. Measured

inputs including PR, FQ, and n-heptane SOI were used along with CA50 as the output to develop linearized SS models. The LPV model from this work modifies the data-driven linear model when the scheduling variable (FQ) changes. The data-driven SS model was then used in conjunction with an MPC controller to form RCCI combustion controller. The second set of experiments were conducted to evaluate tracking performance of the MPC controller at transient operations. All tests in this research were conducted at 1500 RPM engine speed, without turbocharging and exhaust gas recirculation (EGR) while intake temperature was kept at 333 K (60°C).

Chapter 2

Data-driven Modeling and Predictive Control of Combustion Phasing for RCCI Engines

2.1 Introduction

The RCCI strategy relies on high reactive fuel-air mixture pockets to initiate the combustion. These pockets' formation depends on local chemical compositions and temperatures and in-cylinder pressure. Local compositions and temperatures are significantly dependent on in-cylinder flow patterns and DI injection characteristics.

Due to uncertainties in reactive pocket formations, optimal combustion control of RCCI is challenging for the transient engine operations. Therefore RCCI engines require a sophisticated combustion controller to reach their optimal operation where low PM and NOx emissions and high thermal efficiency benefits are obtained without high unburned hydrocarbon (UHC), carbon monoxide (CO) emissions, and high cyclic variability (COV_{IMEP}). [4]. This issue is addressed in the current research and a novel KCCA approach is implemented to develop a data-driven RCCI dynamic model based on unknown plant states. This approach automatically sets engine states based on experimental input-output data from the engine to identify a state-space LPV model.

2.2 State Space Model Identification

Development of a predictive model to capture RCCI engine combustion is essential for designing RCCI combustion controllers for transient operation. It is also important to have a model with low computational demand to be easily implemented on the ECU. DDM approaches can meet these requirements more efficently for less model development costs compared to physics-based approaches. Therefore, a data-driven approach is taken for developing a predictive RCCI combustion model in this research. Here, the data-driven SS identification algorithm from reference [82] is adapted for RCCI engine modeling.

Discrete-time LPV systems can be written as

$$X_{k+1} = A(p_k)X_k + B(p_k)U_k + K(p_k)E_k,$$
$$Y_k = C(p_k)X_k + E_k, \tag{2.1}$$

where, X_k, Y_k, and p_k represent the internal states, the outputs, and the time-varying scheduling variables at discrete-time instant k. Additive Gaussian white noise is denoted by E_k . Matrices $A(p_k) \in \mathbb{R}^{n\times n}$, $B(p_k) \in \mathbb{R}^{n\times n_u}$, $K(p_k) \in \mathbb{R}^{n\times n_y}$ and $C(p_k) \in \mathbb{R}^{n_y\times n}$ represent LPV-SS matrices with a functional dependency on the scheduling variables p_k. We can now re-write the LPV-SS model (2.1) as

$$X_{k+1} = \underbrace{(A(p_k) - K(p_k)C(p_k))}_{\widetilde{A}(p_k)} X_k + B(p_k)U_k + K(p_k)Y_k,$$
$$Y_k = C(p_k)X_k + E_k. \tag{2.2}$$

The objective here is to identify the functional matrix dependencies $\widetilde{A}(p_k)$, $B(p_k)$, $C(p_k)$ based on measured training data $\{X_k, U_k, p_k, Y_k\}_{k=1}^{N}$ from the plant. A Least-Squares Support Vector Machine (LSSVM) approach is taken, and the matrix functions are re-written as

$$X_{k+1} = W_1\Phi_1(p_k)X_k + W_2\Phi_2(p_k)U_k + W_3\Phi_3(p_k)Y_k,$$
$$Y_k = W_4\Phi_4(p_k)X_k + E_k. \tag{2.3}$$

where, $W_{1,2,3} \in \mathbb{R}^{n \times n_H}$ and $W_4 \in \mathbb{R}^{n_y \times n_H}$ are unknown weighting matrices, while $\Phi_1(p_k) \in \mathbb{R}^{n_H \times n}$, $\Phi_2(p_k) \in \mathbb{R}^{n_H \times n_u}$, $\Phi_3(p_k) \in \mathbb{R}^{n_H \times n_y}$, and $\Phi_4(p_k) \in \mathbb{R}^{n_H \times n}$ are unknown feature maps with possibly infinite dimension, n_H. Feature maps can be defined using a kernel function such polynomial, Gaussian, or sigmoid functions. The following least-squares (LS) objective function is minimized

$$\mathcal{J} = \frac{1}{2} \sum_{i=1}^{4} ||W_i||_{\mathrm{F}}^2 + \frac{1}{2} \sum_{k=1}^{N} {E_k}^{\top} \Gamma E_k, \tag{2.4}$$

where, $|| \cdot ||_{\mathrm{F}}$ represents Frobenius norm and Γ is the regularization matrix $\mathrm{diag}(\gamma_1, \gamma_2, ..., \gamma_{n_y})$ on estimation error E_k. The optimization parameters are the weighting matrices $W_{1,2,3,4}$. Dropping the notation for dependence on p_k for brevity, the problem can be written in the dual form and a Lagrangian function can be written as

$$\begin{aligned} &\mathcal{L}(W_1, W_2, W_3, W_4, \alpha, \beta, E) = \\ &\mathcal{J} - \sum_{j=1}^{N} \left(\alpha_j^{\top} \{ W_1 \Phi_1 X_j + W_2 \Phi_2 U_j + W_3 \Phi_3 Y_j - X_{j+1} \} \right) \\ &\quad - \sum_{j=1}^{N} \beta_j{}^{\top} \{ W_4 \Phi_4 X_j + E_j - Y_{j+1} \}, \end{aligned} \tag{2.5}$$

where $\alpha_j \in \mathbb{R}^n$, $\beta_j \in \mathbb{R}^{n_y}$ are Lagrange multipliers at discrete time j. Lagrangian function has convex form and its global optimum can be found where derivatives are

equal to zero.

$$\frac{\partial \mathcal{L}}{\partial \alpha_i} = 0 \Rightarrow$$

$$X_{j+1} = W_1 \Phi_1(p_j) X_j + W_2 \Phi_2(p_j) U_j + W_3 \Phi_3(p_j) Y_j, \tag{2.6a}$$

$$\frac{\partial \mathcal{L}}{\partial W_1} = 0 \Rightarrow W_1 = \sum_{j=1}^{N} \alpha_j {X_j}^\top \Phi_1^\top(p_j), \tag{2.6b}$$

$$\frac{\partial \mathcal{L}}{\partial W_2} = 0 \Rightarrow W_2 = \sum_{j=1}^{N} \alpha_j {U_j}^\top \Phi_2^\top(p_j), \tag{2.6c}$$

$$\frac{\partial \mathcal{L}}{\partial W_3} = 0 \Rightarrow W_3 = \sum_{j=1}^{N} \alpha_j {Y_j}^\top \Phi_3^\top(p_j), \tag{2.6d}$$

$$\frac{\partial \mathcal{L}}{\partial W_4} = 0 \Rightarrow W_4 = \sum_{j=1}^{N} \beta_j {X_j}^\top \Phi_4^\top(p_j), \tag{2.6e}$$

$$\frac{\partial \mathcal{L}}{\partial E_j} = 0 \Rightarrow \beta_j = \Gamma E_j, \tag{2.6f}$$

$$\frac{\partial \mathcal{L}}{\partial \beta_j} = 0 \Rightarrow Y_j = W_4 \Phi_4(\phi_j) X_j + E_j. \tag{2.6g}$$

Substituting (2.6) in (2.3), the model can be re-written as

$$\begin{aligned} X_{k+1} = & \underbrace{\sum_{j=1}^{N} \alpha_j {X_j}^\top \Phi_1^\top(p_j)}_{W_1} \Phi_1(p_k) X_k \\ & + \underbrace{\sum_{j=1}^{N} \alpha_j {U_j}^\top \Phi_2^\top(p_j)}_{W_2} \Phi_2(p_k) U_k \\ & + \underbrace{\sum_{j=1}^{N} \alpha_j {Y_j}^\top \Phi_3^\top(p_j)}_{W_3} \Phi_3(p_k) Y_k, \end{aligned}$$

$$Y_k = \underbrace{\sum_{j=1}^{N} \beta_j {X_j}^\top \Phi_4^\top(p_j)}_{W_4} \Phi_4(p_k) X_k + \underbrace{\Gamma^{-1}\beta_k}_{E_k}. \tag{2.7}$$

Inner product of the feature maps $\Phi_i^\top(p_k)\Phi_i(p_j)$ can be expressed by using the so-called kernel trick and defining the following Grammian matrices

$$[\Omega]_{j,k} = \sum_{i=1}^{3} Z_i^\top(j)\bar{k}^i(p_j, p_k)Z_i(k), \tag{2.8a}$$

$$[\Xi]_{j,k} = X_j^\top \bar{k}^4(p_j, p_k)X_k. \tag{2.8b}$$

where, $Z_i(k)$ is X_k, U_k, Y_k for $i = 1, 2, 3$. In this work, we choose the kernel function $\bar{k}^i(\cdot, \cdot)$ as

$$\bar{k}^i(p_j, p_k) = \exp\bigg(- \frac{||p_j - p_k||_2^2}{2\sigma_i^2}\bigg), \tag{2.9}$$

where, σ_i is the spread of the Gaussian function and $||\cdot||_2$ denotes $\mathcal{L}_2$ norm for the vector. We now express (2.7) in the matrix form as

$$\begin{aligned} \mathcal{X}_{k+1} &= \alpha\Omega, \\ \mathcal{Y} &= \beta\Xi + \Gamma^{-1}\beta. \end{aligned} \tag{2.10}$$

where, $\Omega \in \mathbb{R}^{N\times N}$ and $\Xi \in \mathbb{R}^{N\times N}$ are kernel matrices defined in (2.8) and $\alpha = [\alpha_1 \cdots \alpha_N] \in \mathbb{R}^{n\times N}$ and $\beta = [\beta_1 \cdots \beta_N] \in \mathbb{R}^{n_y\times N}$ are Lagrange multipliers. Variables $\mathcal{X}_{k+1} = [X_1 \cdots X_N] \in \mathbb{R}^{n\times N}$ and $\mathcal{Y} = [Y_1 \cdots Y_N] \in \mathbb{R}^{n_y\times N}$ are the states and outputs

for the N samples, respectively. Solving (2.10) for α and β, we obtain

$$\begin{aligned} \alpha &= \mathcal{X}_{k+1}\Omega^{-1}, \\ \mathrm{vec}(\beta) &= \left(I_N \otimes \Gamma^{-1} + \Xi^\top \otimes I_{n_y}\right)^{-1} \mathrm{vec}(\mathcal{Y}). \end{aligned} \tag{2.11}$$

where, $\otimes$ denotes the Kronecker product and $\mathrm{vec}(\cdot)$ represents the vectorization operator that vertically concatenates columns of a matrix. I_N and I_{n_y} are identity matrices of appropriate dimensions. Using training data $\{X_k, U_k, Y_k\}_{k=1}^N$, $\alpha = [\alpha_1 \cdots \alpha_N]$ and $\beta = [\beta_1 \cdots \beta_N]$ can be computed and the estimated LPV-SS matrices can be written as

$$\widetilde{A}_e(\cdot) = W_1\Phi_1(\cdot) = \sum_{k=1}^{N} \alpha_k X_k^\top \bar{k}^1(p_k, \cdot), \tag{2.12a}$$

$$B_e(\cdot) = W_2\Phi_2(\cdot) = \sum_{k=1}^{N} \alpha_k U_k^\top \bar{k}^2(p_k, \cdot), \tag{2.12b}$$

$$K_e(\cdot) = W_3\Phi_3(\cdot) = \sum_{k=1}^{N} \alpha_k Y_k^\top \bar{k}^3(p_k, \cdot), \tag{2.12c}$$

$$C_e(\cdot) = W_4\Phi_4(\cdot) = \sum_{k=1}^{N} \beta_k X_k^\top \bar{k}^4(p_k, \cdot). \tag{2.12d}$$

where, the subscript e denotes estimate. For the case of the RCCI engine, in order to identify the LPV-SS model, we define the states (X), inputs (U), and outputs (Y) as

$$X = \begin{bmatrix} CA50 & T_{soc} & P_{soc} & IMEP \end{bmatrix}^{\top}, \tag{2.13a}$$

$$U = \begin{bmatrix} PR & SOI & FQ \end{bmatrix}^{\top}, \tag{2.13b}$$

$$Y = \begin{bmatrix} CA50 \end{bmatrix}. \tag{2.13c}$$

As mentioned before, fuel injected per engine cycle, FQ, is chosen as the scheduling variable. The experimental data are collected and divided into training and test sets; 65% of the data is reserved for training the LSSVM and the remaining is used for testing the model. Lagrange multipliers α and β are computed and SS functional matrices are estimated. As an example, estimated LPV-SS model matrices for FQ=25

mg/cycle are reproduced below as

$$A = \begin{bmatrix} 0.6746 & -0.0028 & 0.007 & -0.0008 \\ -10.47 & 0.963 & 0.941 & -0.4036 \\ 0.5038 & -0.0175 & 0.8209 & 0.0206 \\ 0.684 & 0.0366 & 0.8209 & 0.0206 \end{bmatrix},$$

$$B = \begin{bmatrix} 0.0871 & -0.159 & 0.4867 \\ 158.7 & -1.736 & -129.1 \\ -2.163 & -0.0576 & 2.628 \\ -5.247 & 1.374 & 3.572 \end{bmatrix},$$

$$C = \begin{bmatrix} 1 & 0 & 0 & 0 \end{bmatrix}, \quad D = \begin{bmatrix} 0 \end{bmatrix}. \tag{2.14}$$

Using the computed α and β from Eq. (2.11), the trained model is validated using the test data set. The model is excited using the test inputs and scheduling variable, and CA50 is estimated. These estimated values of CA50 are compared with the measured $CA50$ for $PR = 20$, as shown in Figure 2.1. The results show that the developed model can predict CA50 with an average error of 1 CAD. Figure 2.2 show similar results for $PR = 40$. These results demonstrate the capability of the identified LPV-SS model to accurately model the dynamics of the RCCI combustion engine and capture the functional dependencies of the model on the FQ. The results show that the model can predict, to an acceptable degree of accuracy, the behavior of the RCCI

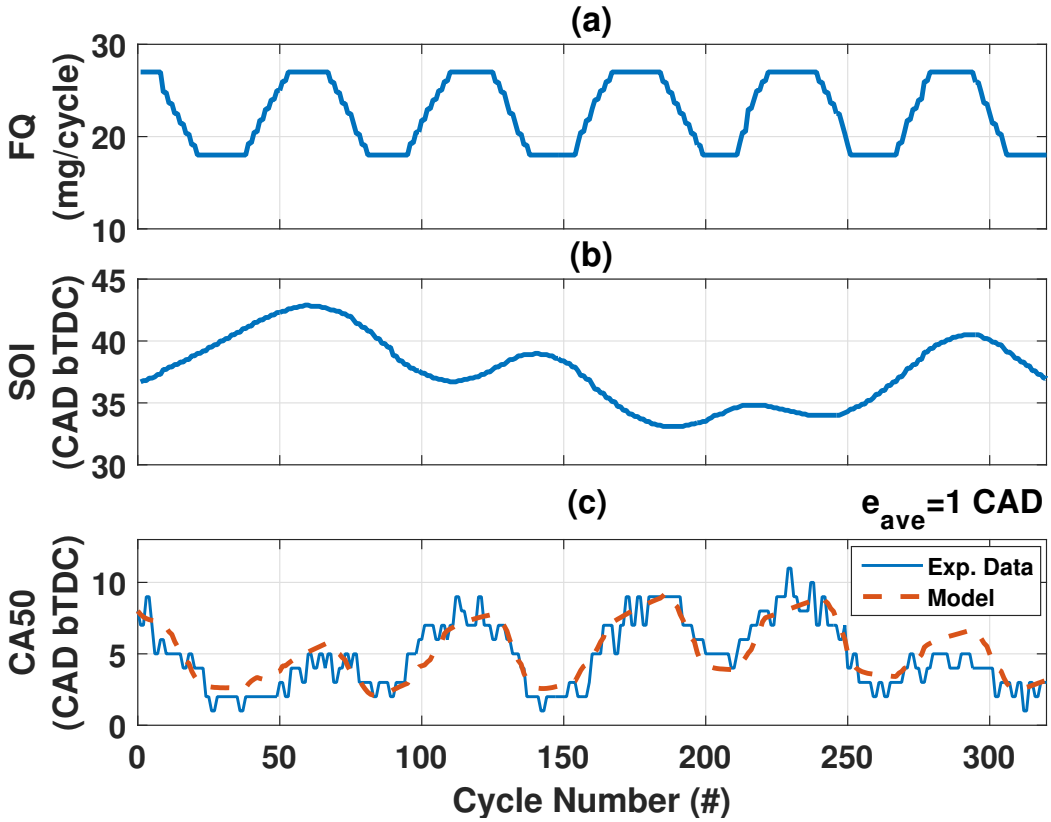

Figure 2.1: LPV-SS model validation for T_{in} = 333 K, N = 1500 rpm, P_{in} = 96.5 kPa, PR=20, 273 kPa<$IMEP$<771 kPa.

engine, and can thus be used for the synthesis of an LPV MPC control strategy.

2.3 Model-based Combustion Controller Design

In this work, MPC is chosen for the combustion control due to its capability to consider actuator and state constrains while performing online optimization. Here, an MPC is designed to track desired CA50 by considering 5 engine cycles as prediction horizon to compute optimal n-heptane SOI as the control variable. The state space

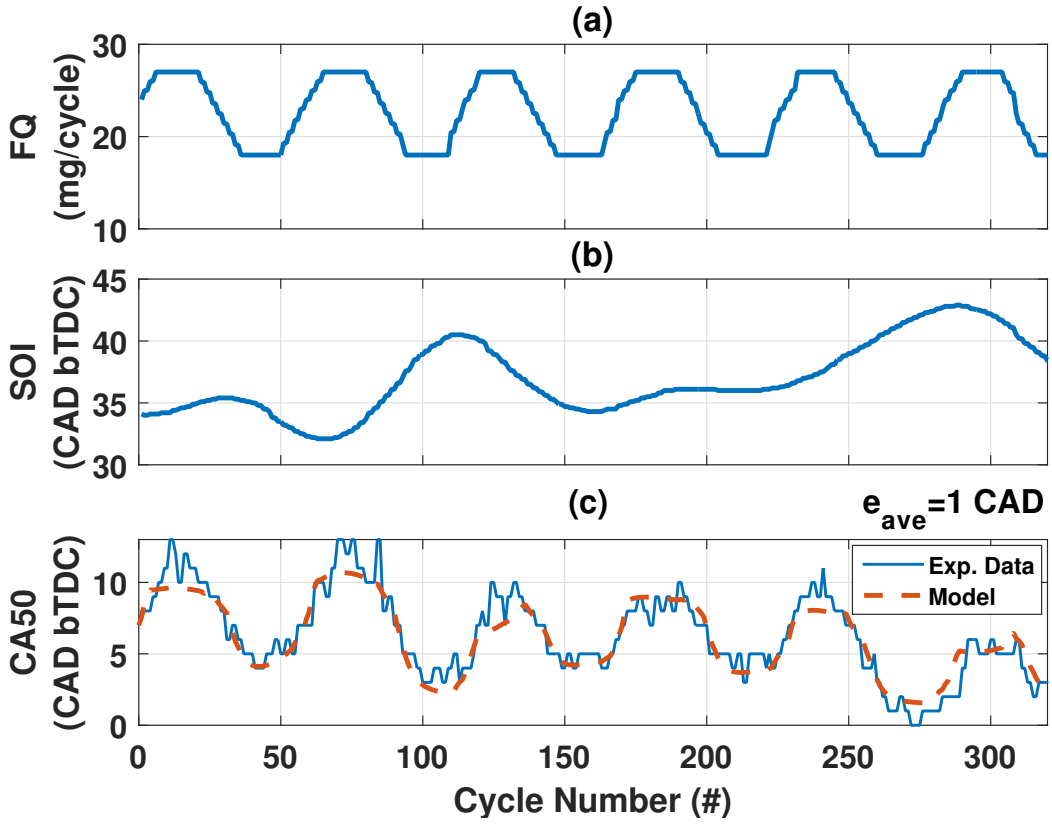

Figure 2.2: LPV-SS model validation for T_{in} = 333 K, N = 1500 RPM, P_{in} = 96.5 kPa, $\underline{PR}$=40, 442 kPa<$IMEP$<806 kPa.

dynamic model of the RCCI engine can be presented in discrete time as

$$X_{k+1} = A(FQ)X_k + B(FQ)U_k, \tag{2.15a}$$

$$Y_{k+1} = C(FQ)X_{k+1} + D(FQ)U_{k+1}, \tag{2.15b}$$

where, states (X), inputs (U), and output (Y) matrices were previously defined by Eq. (2.13). Based on an iterative calculation, the plant output at prediction horizon can be computed as [83]:

$$\mathbb{Y}_k = FX(k_i) + \Phi\mathbb{U}_k, \tag{2.16}$$

where,

$$\mathbb{Y}_k = [Y(k_i+1|k_i) \;\; Y(k_i+2|k_i) \;\; Y(k_i+3|k_i) \;\; Y(k_i+4|k_i) \;\; Y(k_i+5|k_i)]^\top, \tag{2.17}$$

$$\mathbb{U}_k = [U(k_i) \;\; U(k_i+1) \;\; U(k_i+3) \;\; U(k_i+3) \;\; U(k_i+4)]^\top, \tag{2.18}$$

and $Y(k_i+N|k_i)$ denotes the predicted output at step k_i+N with plant information at step k_i ; $U(k_i+N)$ denotes control variable at step k_i+N. F and Φ matrices in Eq. (2.16) are calculated based on A, B, and C matrices from Eq. (2.15) and are described as

$$F = \begin{bmatrix} CA \\ CA^2 \\ CA^3 \\ CA^4 \\ CA^5 \end{bmatrix} ; \Phi = \begin{bmatrix} CB & 0 & 0 & 0 & 0 \\ CAB & CB & 0 & 0 & 0 \\ CA^2B & CAB & CB & 0 & 0 \\ CA^3B & CA^2B & CAB & CB & 0 \\ CA^4B & CA^3B & CA^2B & CAB & CB \end{bmatrix} \tag{2.19}$$

where, notation for dependence on FQ was dropped for brevity. An MPC cost function is defined to minimize prediction tracking error and control action magnitude as

$$J = \sum_{i=1}^{N} [(\Psi_i - Y_i)^\top Q(\Psi_i - Y_i) + U_i^\top R U_i], \tag{2.20}$$

where, Ψ is defined as the matrix for reference outputs over the prediction horizon, Q is the weighting matrix on tracking errors and R is the weighting matrix on the

magnitude of control variables through the prediction horizon. The optimal solution to control variable matrix $\mathbb{U}$ to minimize cost function (2.20) can be derived as

$$\mathbb{U} = (\Phi^\top Q\Phi + R)^{-1}\Phi^\top Q(\Psi - FX_k). \tag{2.21}$$

The MPC cost function for constrained conditions can be expressed by

$$J = \frac{1}{2}\mathbb{U}^\top E\mathbb{U} + \mathbb{U}^\top H, \tag{2.22}$$

where, matrices E and H are determined by

$$E = (\Phi^\top Q\Phi + R), \tag{2.23}$$

$$H = \Phi^\top Q(\Psi - FX_k). \tag{2.24}$$

Constrains are defined by Eq. (2.25) for control commands to actuators and magnitude of output states to protect RCCI engine from receiving excessive control commands.

$$A_{cons}U \leqslant B_{cons}, \tag{2.25}$$

where,

$$A_{cons} = \begin{bmatrix} I_{10\times10} \\ -I_{10\times10} \end{bmatrix}; B_{cons} = \begin{bmatrix} U_{max} - u(k_i - 1) \\ U_{min} + u(k_i - 1) \end{bmatrix}. \tag{2.26}$$

The global optimum for cost function (2.22) subjected to inequality (2.25) is obtained by adapting quadratic programming algorithm from [84].

Figure 2.3 shows the LPV MPC controller schematic and its connections with the RCCI engine and the FPGA. The ECU is loaded with the LPV plant model, a Kalman filter, and the MPC controller. The MPC controller receives identified SS plant matrices as well as states and input values to compute optimal n-heptane SOI values based on Eq. (2.21) as the optimal MPC solution. SS matrices are provided to the MPC controller from the trained LPV model. SS models are dependent on FQ as the scheduling variable which is assigned based on the engine load. The Kalman filter is utilized to estimate T_{soc} and P_{soc} states which are difficult to measure. Only the first step value for calculated optimal n-heptane SOI is implemented and the rest of calculated SOIs are updated in the next time steps.

2.4 Experimental Results

In this section, the combustion controller performance is evaluated under transient conditions. Figure 2.4 presents CA50 tracking results for controller performance at a constant fuel quantity condition. It demonstrates the controller's capability to track desired CA50 with 0.7 CAD average error by adjusting SOI as the control variable. By comparing data-driven combustion control results with the physics-based combustion control results for the same engine which were presented by Raut

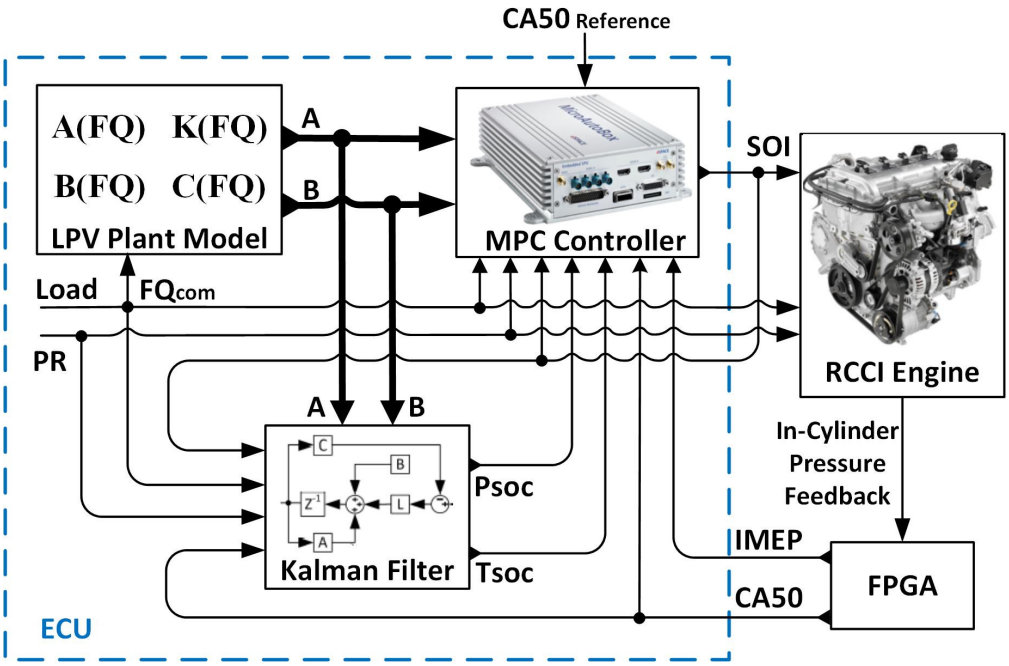

Figure 2.3: Schematic of the designed LPV MPC controller

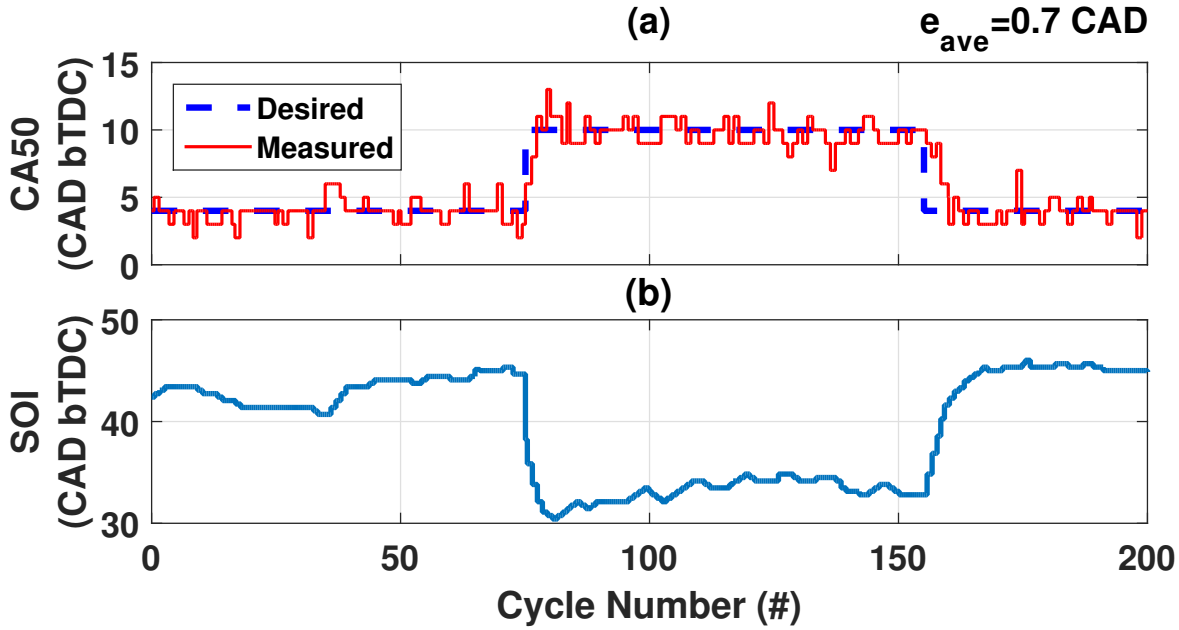

Figure 2.4: Controller performance in tracking desired combustion phasing with $T_{in} = 333$ K, $N = 1500$ RPM, $P_{in} = 96.5$ kPa, $FQ = 25$ mg/cycle.

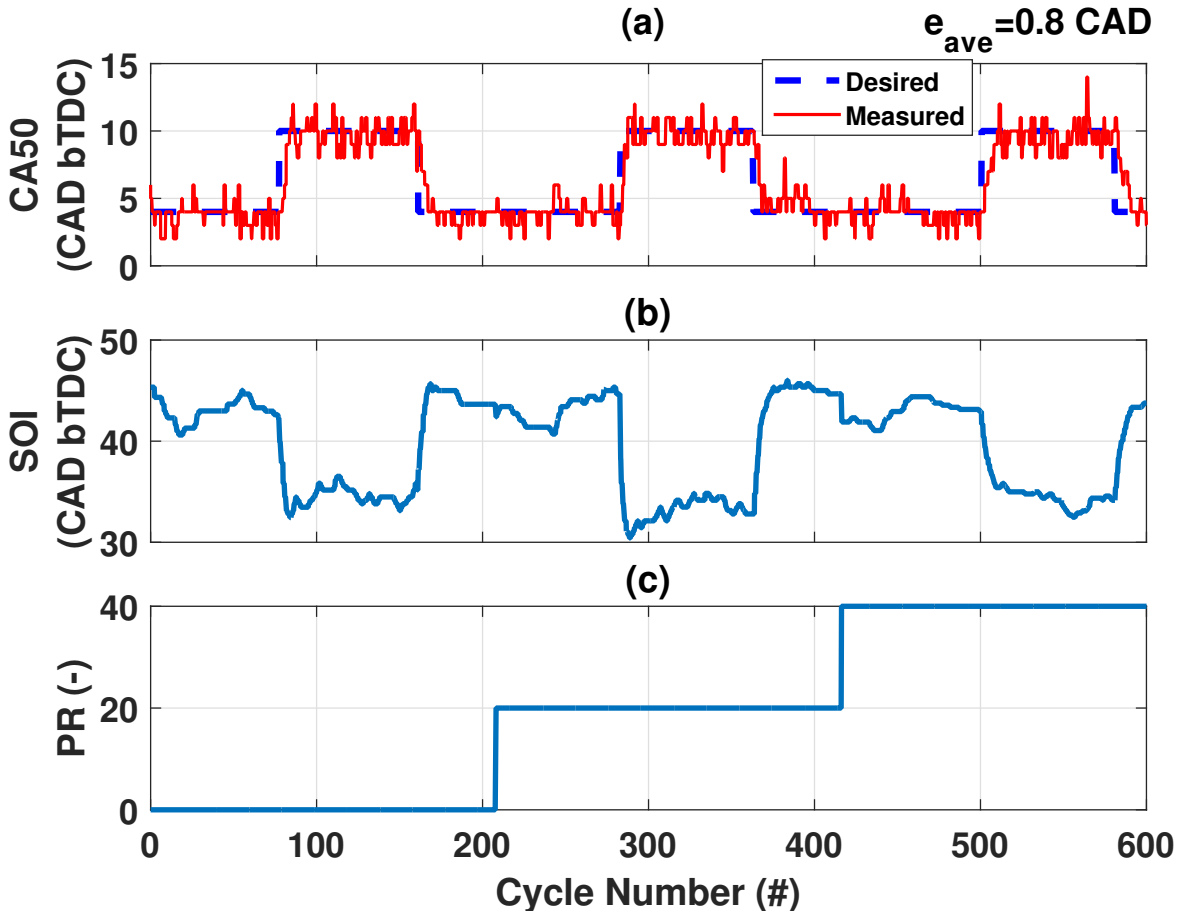

Figure 2.5: Combustion control performance with variable PR, constant FQ =25 mg/cycle, T_{in} = 333 K, N = 1500 RPM, and P_{in} = 96.5 kPa.

et al. [48], it can be observed that data-driven combustion phasing controller in this paper has similar average tracking error compared to the physics-based method in [48]. Considering the efforts required for developing physical control-oriented models, these results demonstrate the advantage of data-driven methods have over physics-based controller designs due to their shorter development time and similar tracking performance.

Figure 2.5 presents combustion control results at constant fuel quantity of 25 mg/cycle

and switching PR values. It shows controller's capability to track desired CA50 with 0.6 CAD average error. While RCCI SS models were identified at PR=20, these models can be used to control combustion phasing at adjacent PR values. This confirms selection of fuel quantity as the dominant scheduling variable to define the plant's linearization points.

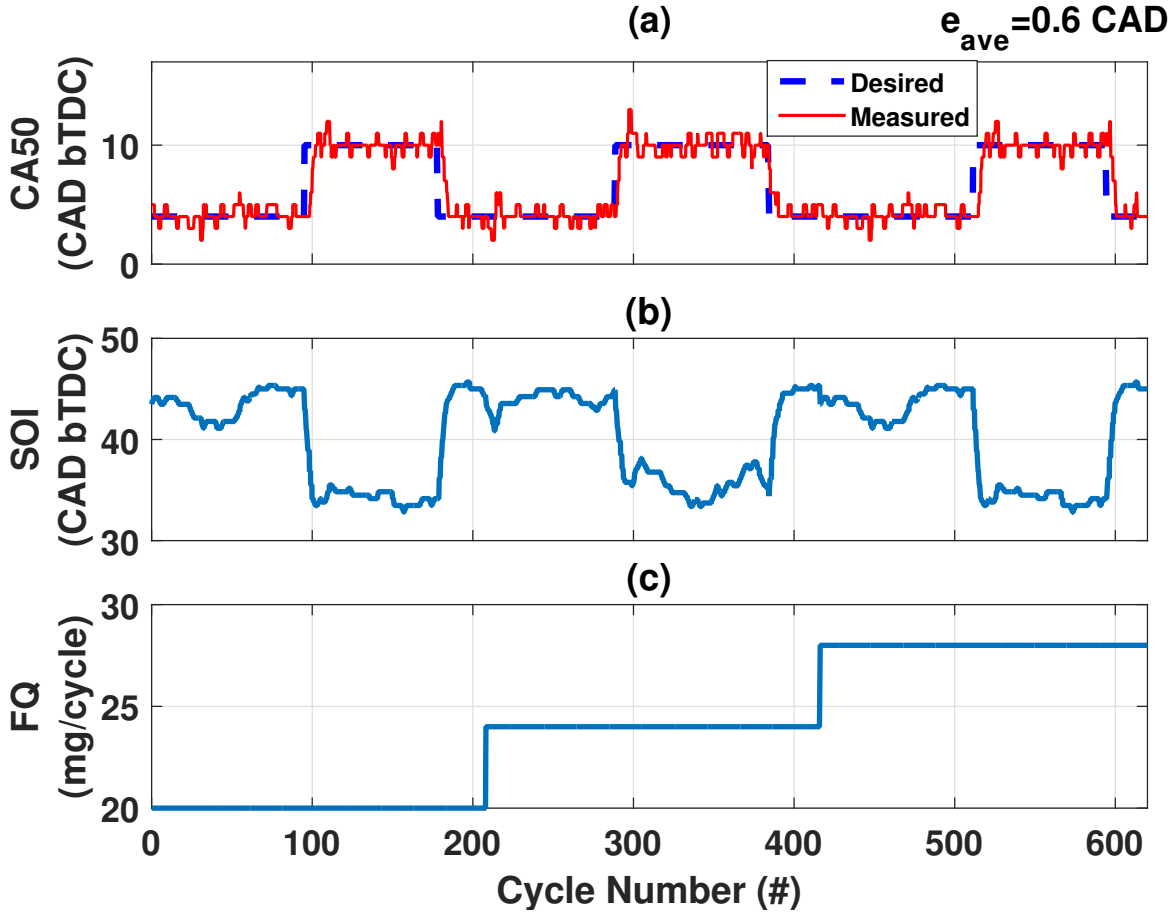

Figure 2.6: Combustion control performance with variable FQ, constant $PR = 20$, $T_{in} = 333$ K, $N = 1500$ RPM, and $P_{in} = 96.5$ kPa.

SOI variations at Figure 2.5(b) show a delay in responding for switching PR from 0 to 20 while switching PR from 20 to 40 results in faster response by the controller.

This response timing difference originates from the PFI fuel transport dynamics. Switching PR from 0 to 20 initiates PFI injectors and starts to form a liquid fuel puddle at intake ports walls. Evaporation of liquid PFI fuel and fuel film transport from intake port walls to cylinder causes combined delay and lag response for changing PR values, particularly when changing from PR=0 (i.e., no PFI) to higher PR that requires PFI injectors to begin to inject *iso*-octane fuel. However, during PR switch from 20 to 40, PFI fuel puddle already exists at intake ports, compared to the case starting from PR=0 that needs time until fuel puddle is formed and becomes steady. Therefore, combustion phasing starts to change faster and controller responds faster to PR change at values higher than 0.

Figure 2.6 presents controller tracking performance for varying FQ quantities. FQ is increased step-wise from 20 to 28 mg/cycle. The engine model is defined for combustion controller by the data-driven model at each step. Desired CA50 is also changed at each step and controller adjusts *n*-heptane SOI to track the desired CA50. Controller performance results show that desired CA50 is tracked with an average error of 0.6 CAD. Combustion controller results at Figure 2.6 demonstrate that LPV plant model can switch SS model correctly based on scheduling variable and the MPC controller is capable of reaching the desired CA50 with small tracking error within 3 engine cycles.

2.5 Summary and Conclusion

This paper introduced the first data-driven LPV model for an RCCI engine using a method of least-square support vector machine. Experimental measurements of the RCCI engine inputs (i.e., SOI, PR, FQ) and the desired output (i.e., CA50) were used to develop the LPV model. The LPV model was then incorporated into an MPC framework to control CA50 by modifying start of injection (SOI) of n-heptane as the DI fuel. Experimental results for the controller demonstrated that the LPV based MPC controller was able to track desired CA50 with maximum of 0.8 CAD average error for varying engine conditions.

Chapter 3

Input-output Data-driven Modeling and MIMO Predictive Control of an RCCI Engine Combustion

3.1 Introduction

Data-driven modeling (DDM) is a more recent approach in RCCI combustion controller design. This approach can reduce model development efforts significantly

while reaching similar estimation accuracy compared to the physics-based modeling approach. Khoshbakht Irdmousa et al. [85] developed and implemented the first validated data-driven RCCI dynamics model. The developed state-space model was used to design an MPC controller to control CA50 on a real RCCI engine. Basina [81] also developed the first data-driven model to estimate maximum pressure rise rate (MPRR) for RCCI engines based on the data obtained from a validated physics-based RCCI model. These researches used known-states data-driven approach where the knowledge for selecting RCCI states is required and structure of the RCCI model needs to be known. Due to the complexity of RCCI combustion, the optimal selection of relevant states to represent RCCI combustion dynamics is challenging. This issue is addressed in the current research and a novel KCCA approach is implemented to develop a data-driven RCCI dynamic model based on unknown plant states. This approach automatically sets engine states based on experimental input-output data from the engine to identify a state-space LPV model. To the best knowledge of authors, this study presents: (i) the first RCCI combustion identification based on input-output approach with unknown model structure. (ii) the first constrained MPC controller design and implementation for an RCCI combustion.

This study has following structure. The theory of KCCA based Linear Parameter Varying modeling is explained in Section 2, and the KCCA-LPV aplication into an RCCI engine is provided in Section 3. Section 4 discusses the physics-based RCCI

dynamic model. Finally, the model predictive controller design and results for input-output-based MPC combustion controller for RCCI combustion is presented in Section 5.

3.2 Kernelized Canonical Correlation Analysis Based Linear parameter Varying modeling

This study utilizes the state estimation approach developed by Rizvi et. al [86] to form an input-output based KCCA-LPV combustion model for an actual RCCI engine. A state-space dynamic model for an LPV system can be presented as shown in Eq. (3.1).

$$X_{k+1} = A(p_k)X_k + B(p_k)U_k + K(p_k)E_k, \tag{3.1a}$$

$$Y_k = C(p_k)X_k + E_k, \tag{3.1b}$$

where, U_k, Y_k, represent the inputs, the outputs, respectively. X_k denotes unknown states at discrete-time instant k. Matrices $A(p_k)$, $B(p_k)$, $K(p_k)$ and $C(p_k)$ denote LPV state-space matrices dependent on scheduling variables p_k. E_k notes additive Gaussian white noise. Eq. (3.1) can be updated by $E_k = Y_k - C(p_k)X_k$ to form state

space model presented by Eq. (3.2).

$$X_{k+1} = \widetilde{A}(p_k)X_k + \widetilde{B}(p_k)U_k + K(p_k)E_k, \tag{3.2a}$$

$$Y_k = C(p_k)X_k + E_k, \tag{3.2b}$$

where $\widetilde{A}(p_k)$ and $\widetilde{B}(p_k)$ are represented by $B(p_k) - K(p_k)D(p_k)$ and $A(p_k) - K(p_k)C(p_k)$, respectively. Identification of $\widetilde{A}(p_k)$, $\widetilde{B}(p_k)$, $K(p_k)$ and $C(p_k)$ requires estimation of states (X_k) associated with measured U_k, Y_k data. LPV-SS formulation at Eq. (3.2) can be used to obtain future outputs as presented in Eq. (3.3).

$$\begin{bmatrix} Y_k \\ Y_{k+1} \\ \vdots \\ Y_{k+d+1} \end{bmatrix} = (\mathcal{O}_f^d \diamond p)_k X_k + (\mathcal{H}_f^d \diamond p)_k \begin{bmatrix} U_k \\ U_{k+1} \\ \vdots \\ U_{k+d+1} \end{bmatrix} + (\mathcal{L}_f^d \diamond p)_k \begin{bmatrix} Y_k \\ Y_{k+1} \\ \vdots \\ Y_{k+d+1} \end{bmatrix} + \begin{bmatrix} e_k \\ e_{k+1} \\ \vdots \\ e_{k+d+1} \end{bmatrix} \tag{3.3}$$

where $(\mathcal{O}_f^d \diamond p)_k$, $(\mathcal{H}_f^d \diamond p)_k$ and $(\mathcal{L}_f^d \diamond p)_k$ are defined as

$$(\mathcal{O}_f^d \diamond p)_k = \begin{bmatrix} C(p_k) \\ C(p_{k+1})\widetilde{B}(p_k) \\ \vdots \\ C(p_{k+d+1}) \prod_{l=2}^{d} \widetilde{A}(p_{k+d-l}) \end{bmatrix} \tag{3.4}$$

$$(\mathcal{H}_f^d \diamond p)_k = \begin{bmatrix} D_k \\ C(p_{k+1})\widetilde{B}(p_k) \\ \vdots \\ C(p_{k+d+1}) \prod_{l=2}^{d} \widetilde{A}(p_{k+d-l})\widetilde{B}(p_k) \end{bmatrix} \tag{3.5}$$

$$\begin{bmatrix} 0 & \dots & 0 \\ D(p_{k+1}) & \dots & 0 \\ \vdots & \ddots & \vdots \\ C(p_{k+d+1}) \prod_{l=2}^{d} \widetilde{A}(p_{k+d-l})\widetilde{B}(p_k) & \dots & 0 \end{bmatrix}$$

$$(\mathcal{L}_f^d \diamond p)_k = \begin{bmatrix} 0 \\ C(p_{k+1})K(p_k) \\ \vdots \\ C(p_{k+d+1}) \prod_{l=2}^{d-1} \widetilde{A}(p_{k+d-l})K(p_k) \end{bmatrix}$$

(3.6)

$$\begin{bmatrix} 0 & \dots & 0 \\ 0 & \dots & 0 \\ \vdots & \ddots & \vdots \\ C(p_{k+d-1}) \prod_{l=2}^{d-2} \widetilde{A}(p_{k+d-l})K(p_{k+1}) & \dots & 0 \end{bmatrix}$$

$(\mathcal{O}_f^d \diamond p)_k$ is the observability matrix at time k along with the scheduling trajectory p. $(\mathcal{H}_f^d \diamond p)_k$ is a forward Toeplitz matrix, and $((\mathcal{L}_f^d \diamond p)_k$ is a lower triangle matrix. Future measured outputs, implemented inputs, white noise, and scheduling parameter vectors for time instant k are collected to form matrices presented in Eq. (3.7a) till Eq. (3.7d).

$$\bar{Y}_{k+d}^d := [Y_k^\top \ \dots \ Y_{k+d-1}^\top]^\top \tag{3.7a}$$

$$\bar{U}_{k+d}^d := [U_k^\top \ \dots \ U_{k+d-1}^\top]^\top \tag{3.7b}$$

$$\bar{E}_{k+d}^d := [e_k^\top \ \dots \ e_{k+d-1}^\top]^\top \tag{3.7c}$$

$$\bar{P}_{k+d}^d := [p_k^\top \ \dots \ p_{k+d-1}^\top]^\top \tag{3.7d}$$

where d represents future data window size. Eq. (3.3) can be updated to by implementing definitions at Eq. (3.7) to form Eq. (3.8)

$$\bar{Y}^d_{k+d} = (\mathcal{O}^d_f \diamond p)_k X_k + (\mathcal{H}^d_f \diamond p)_k \bar{U}^d_{k+d} + (\mathcal{L}^d_f \diamond p)_k \bar{Y}^d_{k+d} + \bar{E}^d_{k+d} \tag{3.8}$$

Unknown states at time step k based on future inputs and outputs are computed from Eq. (3.8) and presented in Eq. (3.9).

$$X_k = (\mathcal{O}^d_f \diamond p)_k{}^{\dagger} \left((I - (\mathcal{L}^d_f \diamond p)_k) \bar{Y}^d_{k+d} - (\mathcal{H}^d_f \diamond p)_k \bar{U}^d_{k+d} \right) - (\mathcal{O}^d_f \diamond p)^{\dagger} \bar{E}^d_{k+d} \tag{3.9}$$

Since E is an independent zero-mean process noise which is identically distributed at experimental data, $(\mathcal{O}^d_f \diamond p)^{\dagger} \bar{E}^d_{k+d}$ is expected to be zero and can be eliminated. State estimation represented at Eq. (3.9) is simplified to Eq. (3.10) by defining $\bar{Z}^d_{k+d} = \begin{bmatrix} \bar{U}^d_{k+d} \\ \bar{Y}^d_{k+d} \end{bmatrix}$ as the collection of future plant inputs and outputs .

$$X_k = (\mathcal{O}^d_f \diamond p)_k{}^{\dagger} \begin{bmatrix} -(\mathcal{H}^d_f \diamond p)_k & I - (\mathcal{L}^d_f \diamond p)_k \end{bmatrix} \bar{Z}^d_{k+d} \tag{3.10}$$

Future mapping matrix can be defined as Eq. (3.11)

$$\varphi_f(\bar{p}^d_{k+d}) = (\mathcal{O}^d_f \diamond p)_k{}^{\dagger} \begin{bmatrix} -(\mathcal{H}^d_f \diamond p)_k & I - (\mathcal{L}^d_f \diamond p)_k \end{bmatrix} \tag{3.11}$$

and state estimation at time step k can be simply expressed as:

$$X_k = \varphi_f(\bar{p}^d_{k+d})\bar{Z}^d_{k+d} \tag{3.12}$$

This approach is also applicable to past measurements to estimate unknown states at time step k based on stepwise output calculation from past d step measurement.

$$\begin{aligned} X_k = (\mathcal{X}^d_p \diamond p)_k X_{k-d} + (\mathcal{R}^d_p \diamond p)_k \begin{bmatrix} U_{k-d} \\ U_{k-d+1} \\ \vdots \\ U_{k-1} \end{bmatrix} \\ + (\mathcal{V}^d_p \diamond p)_k \begin{bmatrix} Y_{k-d} \\ Y_{k-d+1} \\ \vdots \\ Y_{k-1} \end{bmatrix} \end{aligned} \tag{3.13}$$

where $(\mathcal{X}^d_p \diamond p)_k$, $(\mathcal{R}^d_p \diamond p)_k$ and $(\mathcal{V}^d_p \diamond p)_k$ are defined as

$$(\mathcal{X}^d_p \diamond p)_k = \prod_{l=1}^{d} \widetilde{A}(p_{k-l}) \tag{3.14}$$

$$\begin{aligned} (\mathcal{R}^d_p \diamond p)_k = \Big[(\textstyle\prod_{l=1}^{d-1} \widetilde{A}(p_{k-l}))B(p_{k+1}) \quad \dots \\ \widetilde{A}(p_{k-l}))B(p_{k-2}) \quad B(p_{k-1} \Big] \end{aligned} \tag{3.15}$$

$$(\mathcal{V}_p^d \diamond p)_k = \Bigg[(\prod_{l=1}^{d-1} \widetilde{A}(p_{k-l}))K(p_{k+1}) \quad \dots \quad \widetilde{A}(p_{k-l}))K(p_{k-2}) \quad K(p_{k-1} \Bigg] \tag{3.16}$$

Past measured outputs, inputs, white noise, and scheduling parameter vectors for time instant k are denoted by $\bar{Y}_k^d$, $\bar{U}_k^d$, $\bar{E}_k^d$, and $\bar{P}_k^d$.

$$\bar{Y}_k^d := [Y_k^\top \ \ ... \ \ Y_{k+d-1}^\top]^\top \tag{3.17a}$$

$$\bar{U}_k^d := [U_k^\top \ \ ... \ \ U_{k+d-1}^\top]^\top \tag{3.17b}$$

$$\bar{E}_k^d := [e_k^\top \ \ ... \ \ e_{k+d-1}^\top]^\top \tag{3.17c}$$

$$\bar{P}_k^d := [p_k^\top \ \ ... \ \ p_{k+d-1}^\top]^\top \tag{3.17d}$$

Definitions at Eq. (3.17) can be used to rewrite state estimation at Eq. (3.13).

$$X_k = (\mathcal{X}_p^d \diamond p)_k X_{k-d} + (\mathcal{R}_p^d \diamond p)_k \bar{U}_k^d + (\mathcal{V}_p^d \diamond p)_k \bar{Y}_k^d \tag{3.18}$$

Choosing d such that $(\mathcal{X}_p^d \diamond p)_k \approx 0$ and defining $\bar{Z}_k^d = \begin{bmatrix} \bar{U}_k^d \\ \bar{Y}_k^d \end{bmatrix}$, state estimation at Eq. (3.18) is expressed as Eq. (3.19).

$$X_k = \Bigg[(\mathcal{R}_f^d \diamond p)_k \quad (\mathcal{V}_f^d \diamond p)_k \Bigg] \bar{Z}_k^d \tag{3.19}$$

State estimation at time step k based on the past data is simplified to Eq. (3.21) by defining $\varphi_p(\bar{P}_k^d)$ as the past mapping matrix.

$$\varphi_p(\bar{P}_k^d) = \begin{bmatrix} (\mathcal{R}_f^d \diamond p)_k & (\mathcal{V}_f^d \diamond p)_k \end{bmatrix} \tag{3.20}$$

$$X_k = \varphi_p(\bar{P}_k^d)\bar{Z}_k^d \tag{3.21}$$

The past data-based state estimation approach which is presented in Eq. (3.12) can be employed to obtain a collection of all estimated states at all time steps. This collection is named as Φ_p and defined in Eq. (3.22)

$$\Phi_p := \begin{bmatrix} \varphi_p(\bar{P}_1^d)\bar{Z}_1^d & \varphi_p(\bar{P}_2^d)\bar{Z}_2^d & ... & \varphi_p(\bar{P}_N^d)\bar{Z}_N^d \end{bmatrix}^\top \tag{3.22}$$

Φ_f is also defined as the collection of estimated states at all time steps based on the future data estimation method presented at Eq. (3.23).

$$\Phi_f = \begin{bmatrix} \varphi_p(\bar{P}_{1+d}^d)\bar{Z}_{1+d}^d & \varphi_p(\bar{P}_{2+d}^d)\bar{Z}_{2+d}^d & \dots \\ & & \varphi_p(\bar{P}_{N+d}^d)\bar{Z}_{N+d}^d \end{bmatrix}^\top \tag{3.23}$$

Due to the propagation of input and output measurement uncertainties, there will be uncertainties in the identified LPV state-space matrices at Eq. (3.1). This issue may cause a discrepancy between Φ_f and Φ_p. Maximizing correlation between future data-based estimated states and past data-based estimated states can be accomplished

by Canonical Correlation Analysis (CCA) method. CCA is a numerical approach employed to find projection vectors v_j and w_j along which two variable collections V and W have a maximum correlation. CCA objective is represented by the constrained optimization problem at Eq. (3.24) where constraints are defined to minimize v_j and w_j magnitudes.

$$\underset{v_j,w_j}{max} \;\; v_j^\top V^\top W w_j \quad s.t. \quad v_j^\top V^\top V v_j = w_j^\top W^\top W w_j = 1 \tag{3.24}$$

The CCA problem with respected past data based estimated states and future data based estimated states can be provided by the following description:

$$\underset{v_j,w_j}{max} \;\; v_j^\top \Phi_f^\top \Phi_p w_j \quad s.t. \quad v_j^\top \Phi_f^\top \Phi_f v_j = w_j^\top \Phi_p^\top \Phi_p w_j = 1 \tag{3.25}$$

Eq. (3.26) presents CCA optimization problem in a regularized version based on LS-SVM formation.

$$\begin{aligned} &\underset{v_j,w_j}{max} \;\; \mathcal{J}(v_j, w_j, s, r) = \\ &\quad \underset{v_j,w_j}{max} \;\; \gamma \sum_{k=1}^{N} (s_k r_k - v_f \frac{1}{2} s_k^2 - v_p \frac{1}{2} s_k^2) - \frac{1}{2} v_j^\top v_j - \frac{1}{2} w_j^\top w_j, \\ &\quad s.t. \quad s_k = v_j^\top \varphi_f(\bar{P}_{k+d}^d) \bar{Z}_{k+d}^d \quad r_k = w_j^\top \varphi_p(\bar{P}_k^d) \bar{Z}_k^d \end{aligned} \tag{3.26}$$

Solution for the regularized CCA formation can be obtained by Lagrangian formation represented by Eq. (3.27).

$$\begin{aligned}\mathcal{L}(v_j, w_j, s, r) = \\ \mathcal{J}(v_j, w_j, s, r) - \sum_{k=1}^{N} \eta_j^k (s_k - v_j^\top \varphi_f(\bar{P}_{k+d}^d)\bar{Z}_{k+d}^d) - \\ \sum_{k=1}^{N} \kappa_j^k (s_k - v_j^\top \varphi_f(\bar{P}_k^d)\bar{Z}_k^d)\end{aligned} \tag{3.27}$$

where $\eta_j = [\eta_j^1 \quad ... \quad \eta_j^N]^\top$ and $\kappa_j = [\kappa_j^1 \quad ... \quad \kappa_j^N]^\top$ are Lagrangian multipliers. The global minimum is computed where derivatives with respect to Lagrangian function variables are zero. Lagrange problem can be converted to the following generalized eigenvalue problem.

$$K_p p \kappa_j = \lambda_j (v_f K_f f + I)\eta_j \tag{3.28a}$$

$$K_f f \eta = \lambda_j (v_f K_f f + I)\kappa_j, \tag{3.28b}$$

where $K_{pp} = \Phi_p \Phi_p^\top$ and $K_{ff} = \Phi_f \Phi_f^\top$. Lagrangian multipliers are the solution of the generalized eigen value problem presented in Eq. (3.29).

$$\begin{bmatrix} o & K_{pp} \\ K_{ff} & 0 \end{bmatrix} \begin{bmatrix} \eta_j \\ \kappa_j \end{bmatrix} = \lambda_j \begin{bmatrix} v_{ff} K_{ff} + I & 0 \\ 0 & v_p K_{pp} + I \end{bmatrix} \begin{bmatrix} \eta_j \\ \kappa_j \end{bmatrix} \tag{3.29}$$

Finally, Lagrangian multipliers are used to compute the estimated states as

$$x_k^j = \kappa_j \begin{bmatrix} (\bar{Z}_1^d)^T \bar{k}(\bar{P}_1^d, \bar{P}_k^d) \\ (\bar{Z}_2^d)^T \bar{k}(\bar{P}_2^d, \bar{P}_k^d) \\ \vdots \\ (\bar{Z}_N^d)^T \bar{k}(\bar{P}_N^d, \bar{P}_k^d) \end{bmatrix} = \eta_j \begin{bmatrix} (\bar{Z}_{1+d}^d)^T \bar{k}(\bar{P}_{1+d}^d, \bar{P}_{k+d}^d) \\ (\bar{Z}_{2+d}^d)^T \bar{k}(\bar{P}_{2+d}^d, \bar{P}_{k+d}^d) \\ \vdots \\ (\bar{Z}_{N+d}^d)^T \bar{k}(\bar{P}_{N+d}^d, \bar{P}_{k+d}^d) \end{bmatrix} \tag{3.30}$$

Estimated states through the KCCA method can be used along with measured inputs and outputs to obtain a state-space dynamic model of the RCCI engine. This research utilizes least-squared SVM (LS-SVM) to determine matrices $\tilde{A}(p_k), B(p_k), C(p_k)$, and $K(p_k)$ at Eq. (3.2). These state-space matrices are defined based on support vector weighting matrices and feature maps using Eq. (3.31):

$$\tilde{A}(p_k) = W_1 \Phi_1(p_k); B(p_k) = W_2 \Phi_2(p_k) \tag{3.31a}$$

$$K(p_k) = W_3 \Phi_3(p_k); C(p_k) = W_4 \Phi_4(p_k) \tag{3.31b}$$

where unknown support vector weighting matrices are shown by $W_{1,2,3,4}$ and unknown feature maps are represented by $\Phi_{1,2,3,4}$. A SVM based discrete-time state-space model can be represented by Eq. (3.32).

$$X_{k+1} = W_1 \Phi_1(p_k) X_k + W_2 \Phi_2(p_k) U_k + W_3 \Phi_3(p_k) Y_k, \tag{3.32a}$$

$$Y_k = W_4 \Phi_4(p_k) X_k. \tag{3.32b}$$

State-space matrices can be obtained from feature maps and weighting matrices as presented at Eq. (3.33). [82]

$$\tilde{A}_e(\cdot) = W_1\Phi_1(\cdot) = \sum_{k=1}^{N} \alpha_k x_k^T \bar{k}^1(p_k, \cdot) \tag{3.33a}$$

$$B_e(\cdot) = W_2\Phi_2(\cdot) = \sum_{k=1}^{N} \alpha_k u_k^T \bar{k}^2(p_k, \cdot) \tag{3.33b}$$

$$K_e(\cdot) = W_3\Phi_3(\cdot) = \sum_{k=1}^{N} \alpha_k y_k^T \bar{k}^3(p_k, \cdot) \tag{3.33c}$$

$$C_e(\cdot) = W_4\Phi_4(\cdot) = \sum_{k=1}^{N} \beta_k x_k^T \bar{k}^3(p_k, \cdot) \tag{3.33d}$$

where α and β are Lagrangian multipliers and $\bar{k}^i(p_j, p_k)$ is Gaussian kernel function presented at Eq. (3.34).

$$\bar{k}^i(p_j, p_k) = exp(-\frac{||p_j - p_k||_2^2}{2\sigma_i^2}), \tag{3.34}$$

σ_i denotes the standard deviation and $||.||_2$ is representing the l_2 norm. The defined Gaussian function is used in this LPV modeling approach to perform kernel trick. Computed $\tilde{A}_e(.), B_e(.), K_e(.)$, and $C_e(.)$ matrices at Eq. (3.33) can be included in Eq. (3.2) to represent the data driven state space dynamic model of the plant.

3.3 KCCA-LPV modeling of an RCCI Engine

The presented method from section 2 is used to develop a control-oriented combustion model for an RCCI engine. Experimental data were obtained from a 2-liter 4-cylinder RCCI engine. Inputs to the engine and measurable outputs from the engine are defined in Eq. (3.35) and (3.36), respectively.

$$U = \begin{bmatrix} PR & SOI & FQ \end{bmatrix}^T, \tag{3.35}$$

$$Y = \begin{bmatrix} CA50 & IMEP \end{bmatrix}^T. \tag{3.36}$$

Input *n*-heptane SOI, PR, and FQ were varied and CA50, IMEP were computed from acquired pressure traces. Scheduling variable was considered to be fuel quantity as it is the primary parameter to affect engine load (IMEP) and affects the RCCI engine dynamics. Fig. 3.1 presents a sample of acquired experimental data at PR=10 and varied FQ and SOI values. The collected experimental data were split into training data and test data sets. Training data set which includes 65% of the data is used by KCCA-LPV approach to estimate unknown states. This leads finding Lagrangian multipliers α and β for the representation of the RCCI combustion dynamics. Computed Lagrangian multipliers are used to estimate state space at Eq. (3.33). The developed LPV representation is then used to estimate the plant

output at the remaining 35% of the data which was reserved as the test data.

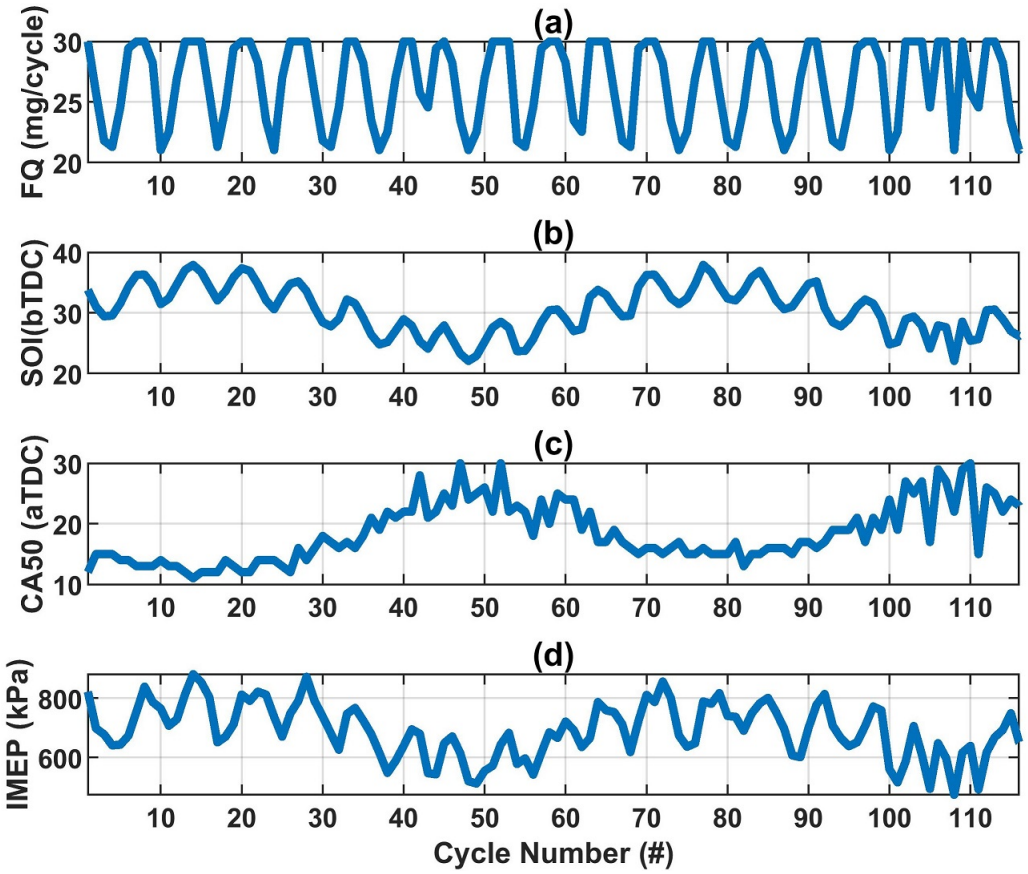

Figure 3.1: Training data from the RCCI engine at $T_{in} = 333$ K, $N = 1200$ RPM, $P_{in} = 96.5$ kPa, $PR = 10$.

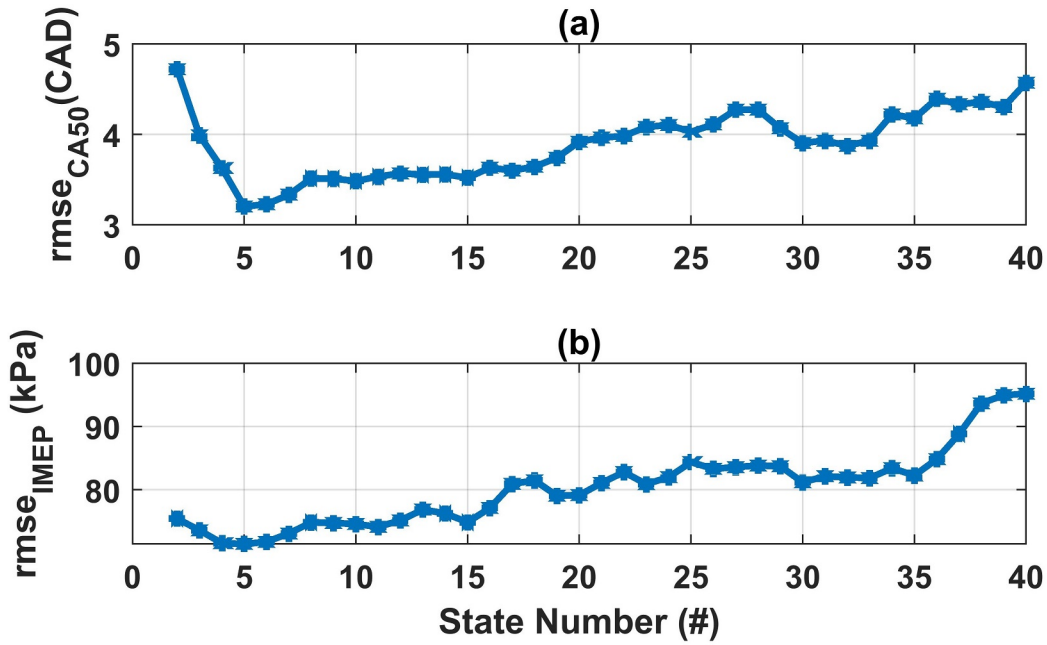

Figure 3.2: The effect of unknown states number on model identification accuracy.

$$\begin{bmatrix} X_1 \\ X_2 \\ X_3 \\ X_4 \\ X_5 \end{bmatrix}_{k+1} = A(FQ) \begin{bmatrix} X_1 \\ X_2 \\ X_3 \\ X_4 \\ X_5 \end{bmatrix}_{k} + B(FQ) \begin{bmatrix} SOI \\ FQ \\ PR \end{bmatrix}_{k}, \tag{3.37a}$$

$$\begin{bmatrix} CA50 \\ IMEP \end{bmatrix}_{k+1} = C(FQ) \begin{bmatrix} X_1 X_2 X_3 X_4 X_5 \end{bmatrix}^{T}_{k+1}, \tag{3.37b}$$

The KCCA-LPV modeling approach allows states to be independent of outputs and consequently states numbers can be varied to obtain the best estimation accuracy for the test data. Fig. 3.2 presents the effect of estimated state size on estimation

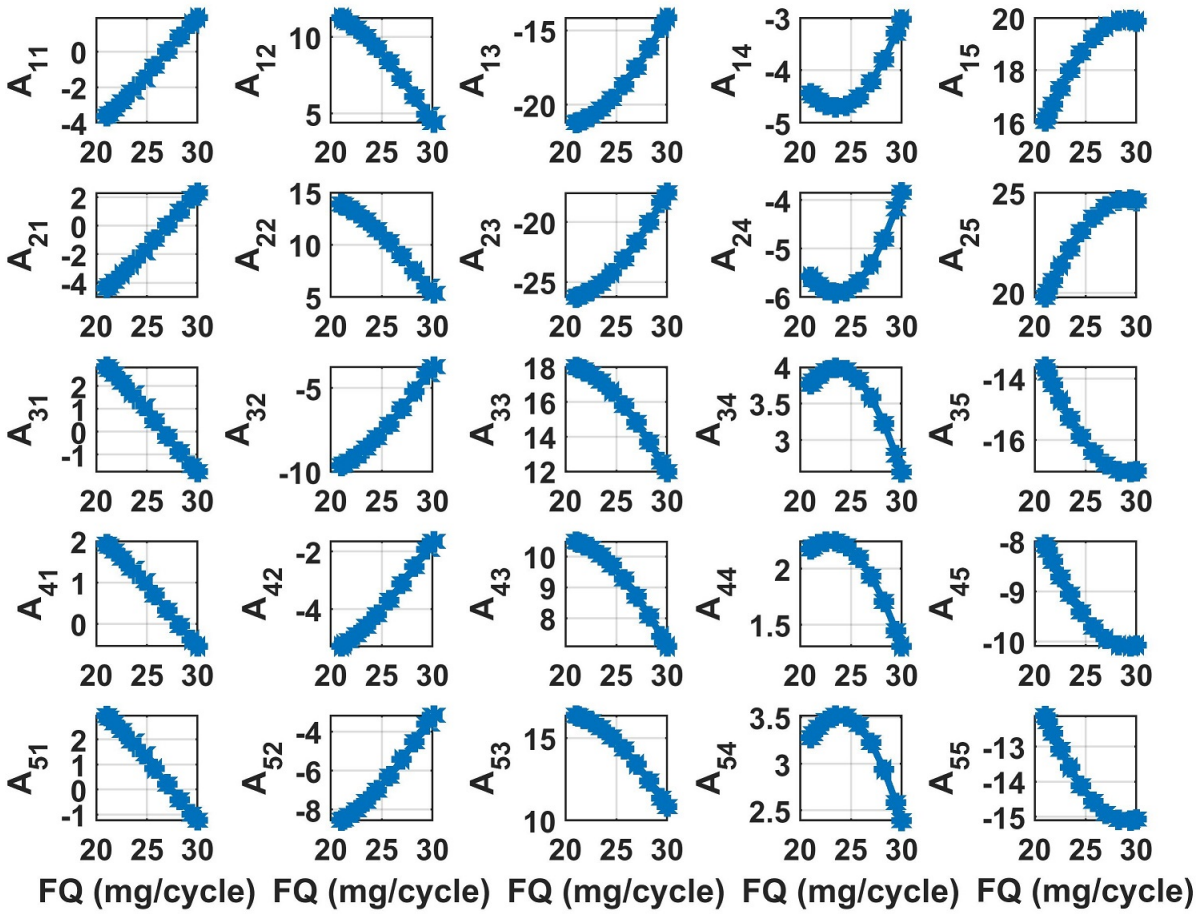

Figure 3.3: LPV representaion of "A" matrix by KCCA identification, representing RCCI dynamics in a state-space model.

accuracy for CA50 and IMEP. The KCCA-LPV model accuracy reaches the highest accuracy when KCCA uses five unknown states at each time step. Therefore, state numbers are selected to be five, and state-space representation of the RCCI combustion is represented as Eq. (3.37). Fig. 3.3 shows dependency of identified A matrix elements on fuel quantity as the scheduling variable. It can be observed that these elements vary significantly with the scheduling variable variation as we expect from a typical LPV system. Fig. 3.4 verifies performance of the KCCA-LPV model to estimate CA50 and IMEP with 2.4 CAD and 51.7 kPa estimation error,

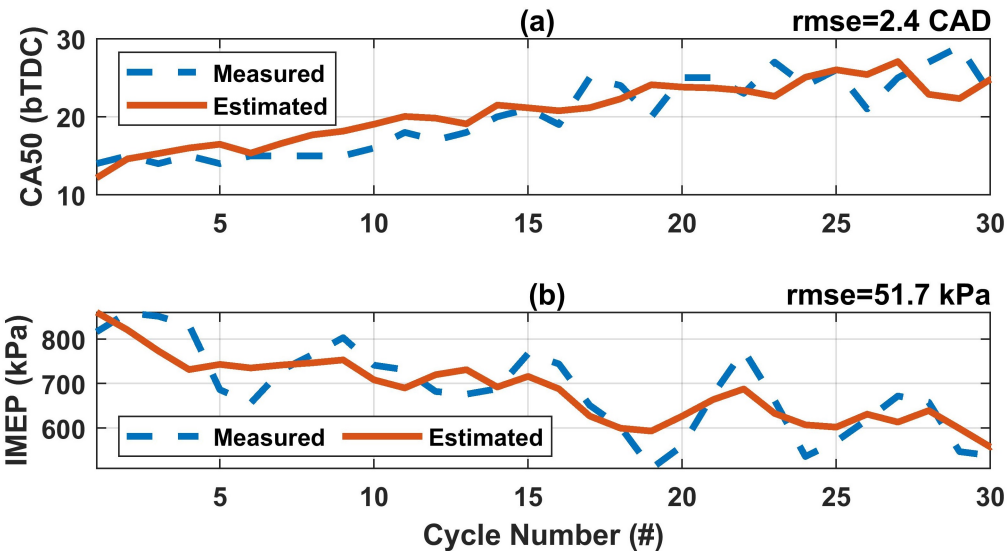

Figure 3.4: Performance of the identified input-output LPV model at $T_{in} =$ 333 K, $N = 1200$ RPM, $P_{in} = 96.5$ kPa, $PR = 14$.

respectively. The developed LPV model is later used to control CA50 and IMEP on a experimentally validated physics-based RCCI model. [81].

3.4 Data-driven Model-based Predictive Combustion Controller Design

This study utilizes the MPC strategy because of its capacity to handle states and actuators' constraints and to predict future plant outputs and consider them during MPC optimization process. Here, a constrained MPC platform (Fig. 3.5) is developed to follow the referenced CA50 and IMEP through five engine cycles as the prediction horizon while computing optimum n-heptane SOI, injected fuel

quantity, and PR as the control variables. The designed MPC controller uses the KCCA-LPV RCCI combustion model to obtain system dynamics. The data-driven

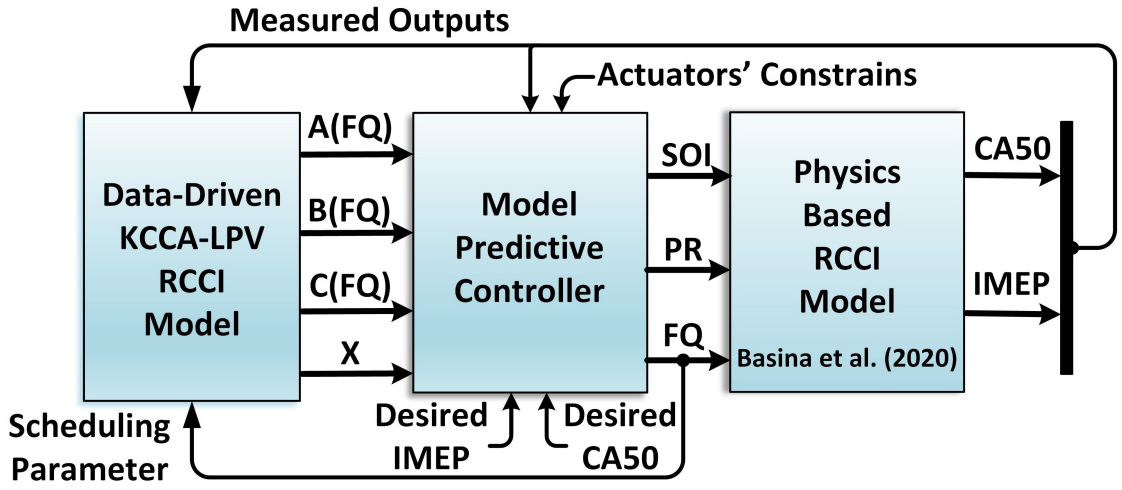

Figure 3.5: Schematic of the designed data-driven input-output identified MIMO model predictive controller.

KCCA-LPV model adjusts the RCCI dynamics based on changing fuel quantity as the scheduling parameter. It also receives measured plant outputs and computes the unknown plant states. The computed state-space matrices and unknown states are provided to the MPC controller to compute optimized control actions based on desired outputs, measured outputs, and actuators' constraints. The decided control actions are then implemented on the validated physics-based RCCI model to test the controller efficiency of the KCCA based constrained MIMO MPC controller.

The discrete time state-space dynamic model of an RCCI combustion which is presented at Eq. (3.37), can be used to iteratively compute plant output through the prediction horizon. Eq. (3.38) represents the predicted plant output through

prediction horizon based on plant information at beginning of the horizon.

$$\mathbb{Y}_k = \Omega X(k_i) + \Phi \mathbb{U}_k, \tag{3.38}$$

$\mathbb{Y}_k$ and $\mathbb{U}_k$ are vectors denoting plant outputs and plant inputs at prediction horizon.

$$\begin{aligned}\mathbb{Y}_k = [&Y(k_i+1|k_i) \;\; Y(k_i+2|k_i) \;\; Y(k_i+3|k_i) \\ &Y(k_i+4|k_i) \;\; Y(k_i+5|k_i)]^\top,\end{aligned} \tag{3.39}$$

$$\begin{aligned}\mathbb{U}_k = [&U(k_i) \;\; U(k_i+1) \;\; U(k_i+3) \\ &U(k_i+3) \;\; U(k_i+4)]^\top,\end{aligned} \tag{3.40}$$

$Y(k_i + N|k_i)$ represents the forecasted plant output at step $k_i + N$ using plant knowledge at step k_i; $U(k_i + N)$ represents control action at step $k_i + N$. Prediction matrices Ω and Φ are computed based on state-space $A(FQ)$, $B(FQ)$, and $C(FQ)$ matrices from Eq. (3.37).

$$\Omega = \begin{bmatrix} CA \\ CA^2 \\ CA^3 \\ CA^4 \\ CA^5 \end{bmatrix}; \Phi = \begin{bmatrix} CB & 0 & 0 & 0 & 0 \\ CAB & CB & 0 & 0 & 0 \\ CA^2B & CAB & CB & 0 & 0 \\ CA^3B & CA^2B & CAB & CB & 0 \\ CA^4B & CA^3B & CA^2B & CAB & CB \end{bmatrix} \tag{3.41}$$

MPC optimization strategy considers to minimize prediction tracking error with minimized control action efforts. This strategy is formulated by the cost function

presented at Eq. (3.42).

$$J = \sum_{i=1}^{N} [(\Psi_i - Y_i)^\top Q(\Psi_i - Y_i) + U_i^\top R U_i], \tag{3.42}$$

where desired outputs through the prediction horizon are denoted by Ψ. The weighting matrices through the prediction horizon on tracking errors and magnitude of control variables are shown by Q and R, respectively. The cost function from Eq. (3.42) is used to generate MPC cost function.

$$\begin{aligned} J = (\Psi - \Omega x(k_i))^\top (\Psi - \Omega x(k_i)) \\ -2\Delta\mathbb{U}^\top \Phi^\top (\Psi - \Omega x(k_i)) + \Delta\mathbb{U}^\top (\Phi^\top \Phi + R)\Delta\mathbb{U}, \end{aligned} \tag{3.43}$$

Constraints on the rate and magnitude of control action can be represented by Eq. (3.44).

$$M\Delta\mathbb{U} \leq \gamma, \tag{3.44}$$

where M, $\Delta\mathbb{U}$ and γ are defined as

$$\Delta\mathbb{U} = \begin{bmatrix} \Delta U(k_i) \\ \Delta U(k_i+1) \\ \Delta U(k_i+2) \\ \Delta U(k_i+3) \\ \Delta U(k_i+4) \end{bmatrix}; \Delta U = \begin{bmatrix} \Delta FQ \\ \Delta SOI \\ \Delta PR \end{bmatrix} \tag{3.45}$$

$$M = \begin{bmatrix} I_3 & 0_{3,3} & 0_{3,3} & 0_{3,3} & 0_{3,3} \\ 0_{3,3} & I_3 & 0_{3,3} & 0_{3,3} & 0_{3,3} \\ 0_{3,3} & 0_{3,3} & I_3 & 0_{3,3} & 0_{3,3} \\ 0_{3,3} & 0_{3,3} & 0_{3,3} & I_3 & 0_{3,3} \\ 0_{3,3} & 0_{3,3} & 0_{3,3} & 0_{3,3} & I_3 \\ -I_3 & 0_{3,3} & 0_{3,3} & 0_{3,3} & 0_{3,3} \\ 0_{3,3} & -I_3 & 0_{3,3} & 0_{3,3} & 0_{3,3} \\ 0_{3,3} & 0_{3,3} & -I_3 & 0_{3,3} & 0_{3,3} \\ 0_{3,3} & 0_{3,3} & 0_{3,3} & -I_3 & 0_{3,3} \\ 0_{3,3} & 0_{3,3} & 0_{3,3} & 0_{3,3} & -I_3 \\ I_3 & 0_{3,3} & 0_{3,3} & 0_{3,3} & 0_{3,3} \\ I_3 & I_3 & 0_{3,3} & 0_{3,3} & 0_{3,3} \\ I_3 & I_3 & I_3 & 0_{3,3} & 0_{3,3} \\ I_3 & I_3 & I_3 & I_3 & 0_{3,3} \\ I_3 & I_3 & I_3 & I_3 & I_3 \\ -I_3 & 0_{3,3} & 0_{3,3} & 0_{3,3} & 0_{3,3} \\ -I_3 & -I_3 & 0_{3,3} & 0_{3,3} & 0_{3,3} \\ -I_3 & -I_3 & -I_3 & 0_{3,3} & 0_{3,3} \\ -I_3 & -I_3 & -I_3 & -I_3 & 0_{3,3} \\ -I_3 & -I_3 & -I_3 & -I_3 & -I_3 \end{bmatrix}; \gamma = \begin{bmatrix} \Delta U_{max} \\ \Delta U_{max} \\ \Delta U_{max} \\ \Delta U_{max} \\ \Delta U_{max} \\ -\Delta U_{min} \\ -\Delta U_{min} \\ -\Delta U_{min} \\ -\Delta U_{min} \\ -\Delta U_{min} \\ U_{max} - U \\ U_{max} - U \\ U_{max} - U \\ U_{max} - U \\ U_{max} - U \\ U_{min} + U \\ U_{min} + U \\ U_{min} + U \\ U_{min} + U \\ U_{min} + U \\ U_{min} + U \end{bmatrix} \tag{3.46}$$

Lagrangian optimization process is used to minimize MPC cost function at Eq. (3.43)

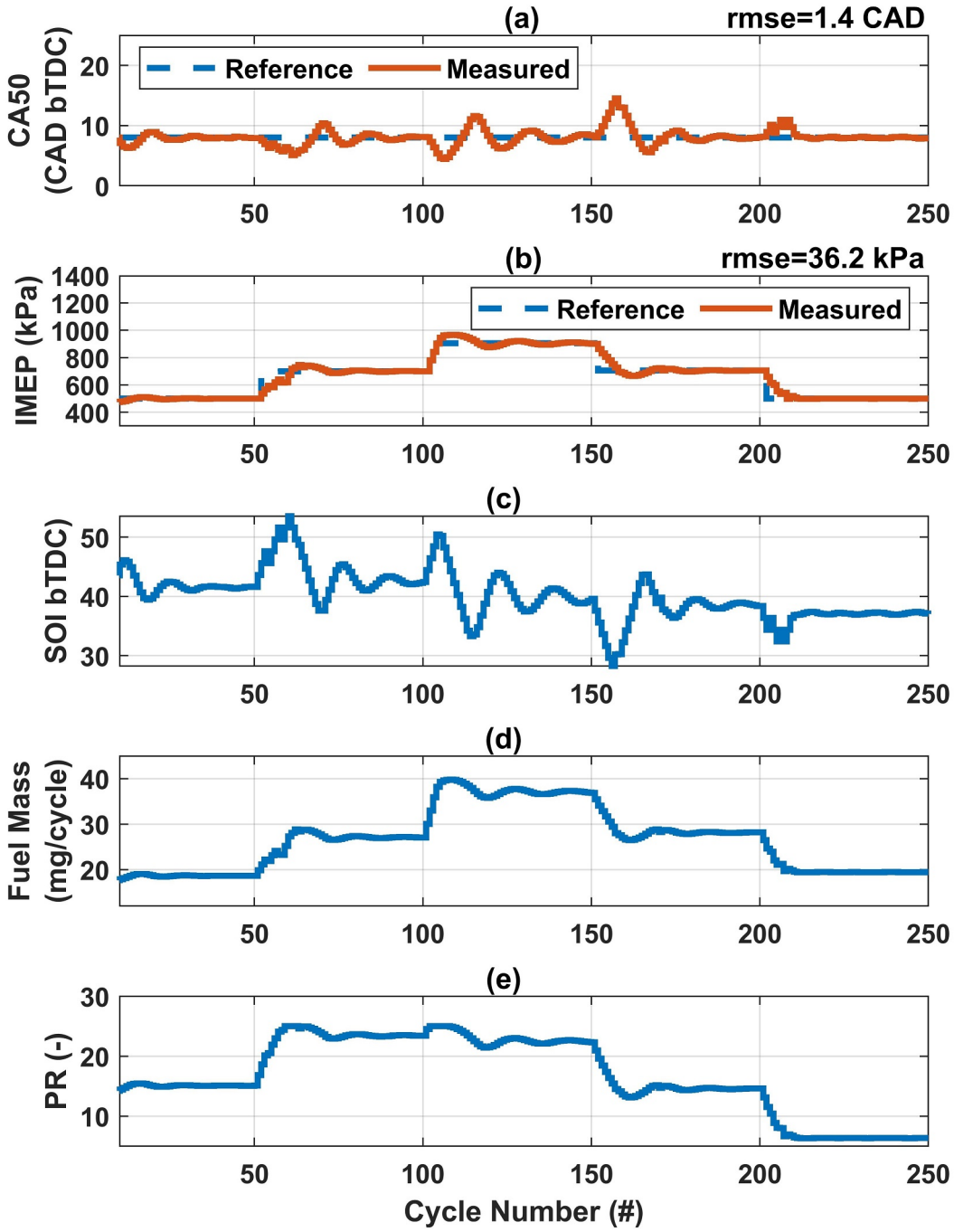

Figure 3.6: Constrained MIMO MPC results at T_{in} = 333 K, N = 1200 RPM, P_{in} = 96.5 kPa. (a) maintaining desired CA50 tracking, (b) load trajectory tracking, control actions: (c) start of injection timing, (d) fuel quantity , (e) premixed ratio.

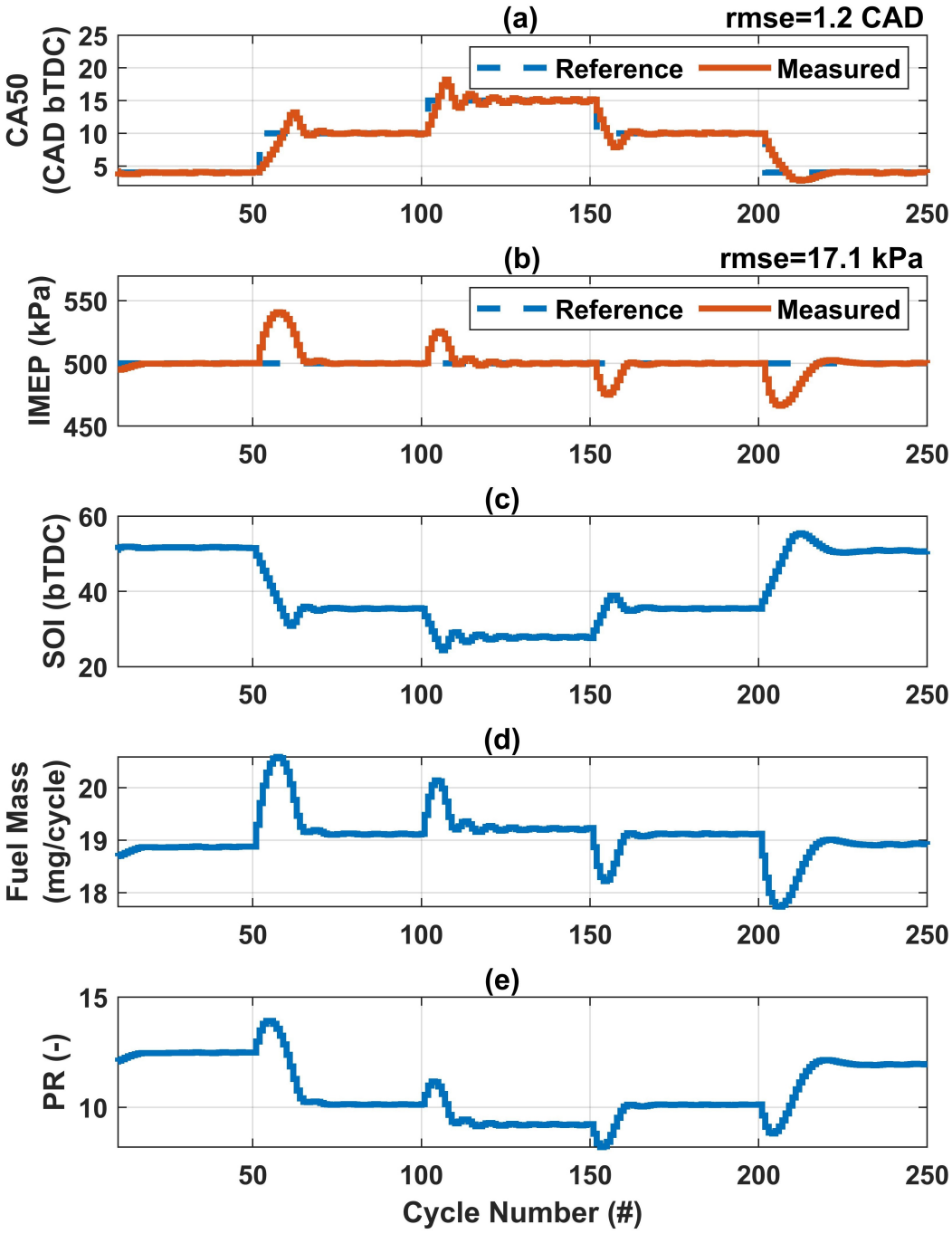

Figure 3.7: Constrained MIMO MPC results at $T_{in} = 333$ K, $N = 1200$ RPM, $P_{in} = 96.5$ kPa (a) CA50 trajectory tracking, (b) Maintaining desired load tracking, control actions: (c) start of injection timing, (d) fuel quantity, (e) premixed ratio variations.

while considering constraints on rate and magnitude of control action represented at Eq. (3.44). Lagrangian optimization can be represented as

$$\underset{\lambda \geq 0}{max} \underset{\Delta \mathbb{U}}{min} [\frac{1}{2} \Delta \mathbb{U}^T E \Delta \mathbb{U} + \Delta \mathbb{U}^T F + \lambda^T (M \Delta \mathbb{U} - \gamma)] \tag{3.47}$$

E and F matrices are defined as:

$$E = 2(\Phi^\top \Phi + R) \tag{3.48}$$

$$F = 2(\Phi^\top \Phi + R) \Phi^\top (\Psi - \Omega x(k_i)) \tag{3.49}$$

The optimal solution is derived to be

$$\Delta \mathbb{U} = -E^{-1} F - E^{-1} M^T \lambda^* \tag{3.50}$$

where λ^* is the solution for the Lagrangian multiplier. This research utilizes Hildret quadratic programming method to perform the following iterative method to compute λ^*

$$\lambda_i^{m+1} = max(0, w_i^{m+1}) \tag{3.51}$$

where w_i^{m+1} is computed as

$$w_i^{m+1} = -\frac{1}{l_{ii}} [k_i + \sum_{j=1}^{i-1} l_{ij} \lambda_j^{m+1} + \sum_{j=i+1}^{n} l_{ij} \lambda_j^m] \tag{3.52}$$

where l_{ij} is the ijth entry in the L matrix and k_i is the ith element in the K matrix. L and K matrices are defined as

$$L = ME^{-1}M^T \tag{3.53}$$

$$K = \gamma + ME^{-1}F \tag{3.54}$$

Fig. 3.6 presents the MPC controller performance to track step changes at IMEP and fixed desired CA50. The controller was able to track desired values with 1.4 CAD and 36.2 kPa errors respectively. A similar test was conducted for fixed desired IMEP and step changes at desired CA50. Fig. 3.7 shows tracking performance and computed control actions. The controller followed the desired IMEP and CA50 with 1.2 CAD and 17.1 kPa tracking errors, respectively.

3.5 CONCLUSIONS

This paper introduced the first Kernelized Canonical Correlation Analysis based LPV state-space dynamic model for an RCCI engine combustion and the first constrained MPC controller for RCCI combustion. The developed controller results showed that the KCCA-LPV based constrained MPC controller followed the referenced CA50 and IMEP with a less than 1.4 CAD and 37 kPa average tracking errors, respectively. Future work includes implementation of the designed controller on the RCCI engine

experimental platform.

Chapter 4

Control-Oriented Data-Driven and Physics-Based Modeling of Maximum Pressure Rise Rate in Reactivity Controlled Compression Ignition Engines

4.1 Introduction

RCCI combustion is a relatively new form of LTC regime which is designed to operate with a mixture of two fuels with different reactivity levels. These fuels are injected

at adjustable rates by two sets of injectors to adjust reactivity levels and control the combustion process inside the combustion chamber. Port Fuel Injectors (PFI) are used to deliver a low reactivity fuel to the airflow at the intake manifold while a high reactivity fuel is directly injected inside the combustion chamber via Direct Injectors (DI). RCCI combustion initiates at high reactive fuel-air mixture pockets inside the combustion chamber and then advances to burn low reactive regions. High reactive pockets formation depends on fuel concentration and local temperature and in-cylinder pressure. Therefore, it is difficult to control RCCI combustion due to difficulties to control reactive pockets formation. Consequently, it is challenging to control combustion in RCCI engines to achieve its low emission and high thermal efficiency benefits. Inadequately controlled RCCI engine may generate high Carbon Monoxide (CO) and Unburned Hydrocarbon (UHC) emissions and runs with high cyclic variability (COV_{IMEP}) [4].

In this paper, the RCCI engine at EML lab was used to obtain necessary experimental data for physics-based and data-driven MPRR model development. Fig. 4.1 presents a sample experimental data obtained by operating the RCCI engine with a combination of input FQ, SOI, and PR. Pressure trace and encoder output were recorded and used to compute MPRR for the RCCI engine.

This paper is organized as follows. The experimental RCCI engine setup is described in Section II. Then, the first control-oriented MPRR model based on physics modeling

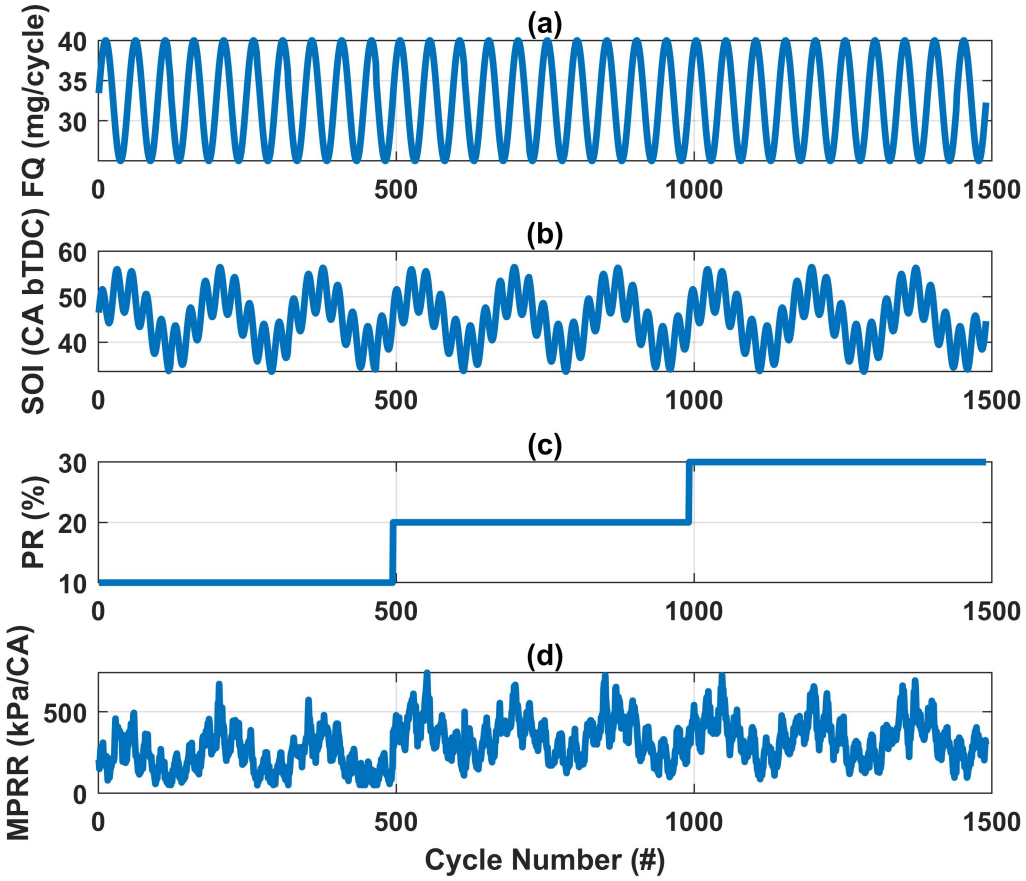

Figure 4.1: Experimental data from RCCI engine at $T_{in} = 333$ K, $N = 1200$ RPM, $P_{in} = 96.5$ kPa.

is described in Section III. Subsequently, the algorithm to develop a data-driven KCCA-LPV model for MPRR estimation is illustrated in section IV and data-driven estimation results are also presented. Finally, a summary of research results and comparison between the two MPRR models is discussed at the summary section.

4.2 Physics based MPRR Dynamic Model

Physics-based MPRR modeling is adapted as the first approach to developing a control-oriented MPRR model. MPRR model requires the development of an in-cylinder pressure rise rate model. Pressure rise rate can be computed through implementing the first law of thermodynamics which is presented in Eq. (4.1).

$$\frac{dP}{d\theta} = \frac{\gamma - 1}{V}\left(\frac{dQ}{d\theta} - \frac{dQ_w}{d\theta}\right) - \frac{\gamma P}{V}.\frac{dV}{d\theta} \tag{4.1}$$

where $\frac{dQ}{d\theta}$ represents the rate of heat release, γ is the adiabatic coefficient of compression, P are the instantaneous pressure, V is the instantaneous volume, and $\frac{dQ_w}{d\theta}$ is the heat transfer to the wall which is computed through the Woschni heat transfer model.

Heat release from the fuel is linearly correlated with mass fraction burn (MFB) of the fuel. MFB can be modeled using a double term or a single term Wiebe function. Fig.4.2 presents a comparison between a single term and a double term Wiebe function. Double term Wiebe functions estimate experimental MFB accurately for the entire combustion process. However single term Wiebe functions accuracy is limited to angles close to TDC. They also tend to overestimate MFB at the later stages of combustion. Since MPRR happens very close to the TDC moment, either a

single term or a double term Wiebe function can be used to represent experimental MFB. The single term Wiebe function as shown in Eq. (4.2) is preferred in this research due to the simplicity of its calibration compared to a double term Wiebe function.

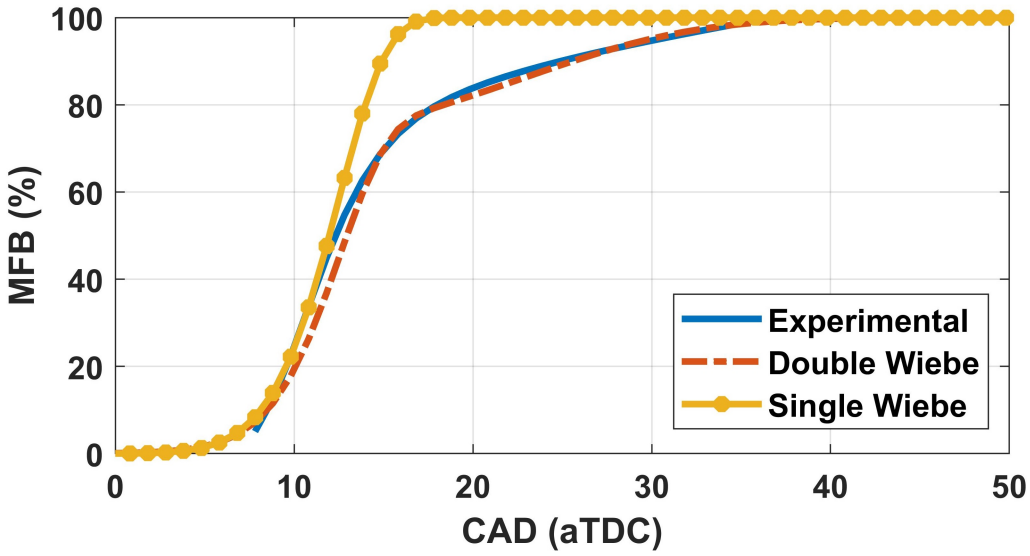

Figure 4.2: Experimental Mass Fraction Estimation, FQ= 17 mg/cycle, SOI=40 CAD bTDC.

$$X_b(\theta) = 1 - exp\left[-\left(\frac{\theta - \theta_{soc}}{\alpha\Delta\theta}\right)^m\right] \tag{4.2}$$

The Wiebe function combined with the LHV of the fuels is used to derive the fuel heat release rate form as shown in Eq. (4.3).

$$\frac{dQ}{d\theta} = LHV_{eff}\frac{m}{\alpha\Delta\theta}\left(\frac{\theta - \theta_{soc}}{\Delta\theta}\right)^{(m-1)} exp\left[-\left(\frac{\theta - \theta_{soc}}{\alpha\Delta\theta}\right)^m\right] \tag{4.3}$$

where the instantaneous crank angle is provided by θ and crank angle at SOC is considered by θ_{soc} and α is the scaling factor which is considered based on extend of burn duration (such as 10% or 90%). The effective lower heating value of fuels is denoted by LHV_{eff} and is calculated by Eq. (4.4).

$$LHV_{eff} = (1 - PR).LHV_{DI} + PR.LHV_{PFI} \tag{4.4}$$

where LHV_{DI} represents Lower Heating Value of the DI injected fuel, in this case, *n*-heptane and LHV_{PFI} is the Lower Heating Value of the PFI injected fuel, in this case *Iso*-octane.

Accurate MPRR estimation requires calibration of the Eq. (4.2) as the Wiebe function used for mass fraction burn estimation. Calibration parameters are m as the shape factor and $\Delta\theta$ as the burn duration which are represented at Eq. (4.5) and Eq. (4.6) respectively.

$$m = C_1' + C_2'.(1 + K).SOI + C_3'.K \tag{4.5}$$

$$\Delta\theta = C_1 + K(C_2.\phi_{di} + C_3.\phi_{pfi} + C_4.SOI + C_5) + C_4.SOI \tag{4.6}$$

where K is defined based on Eq. (4.7)

$$K = exp[-(SOI - C_6)^{C_7}] \tag{4.7}$$

The calibration process was conducted by transient experimental data acquisition at from the RCCI engine. 500 consecutive cycles and 65% of these points, i.e. 325 data points were used to parametrize the Wiebe function while the rest 35%, i.e. 175 data points were used to test the calibrated Wiebe function.

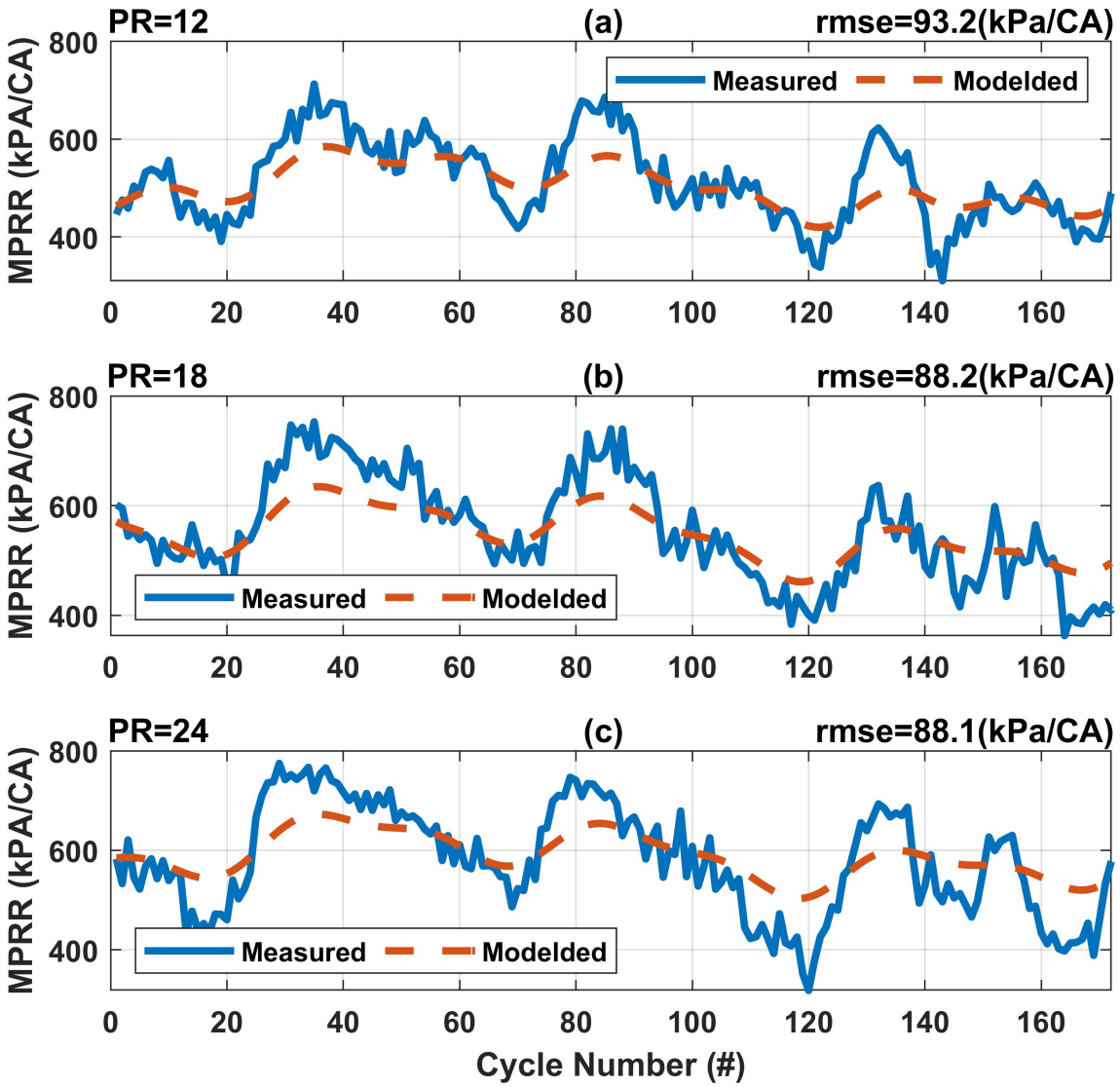

Figure 4.3: Estimation performance of the physics-based MPRR model at N = 1000 RPM, T_{in} = 60° C, (a) PR=12, (b) PR=18, (c) PR=24

Calibrated MPRR model was used to estimated MPRR at the test data set. Fig. 4.3 shows the experimental test data set and modeled MPRR for three experimental data set. It can be observed that the MPRR model was able to predict experimental MPRRs with 86.9.5 kPa/CAD as the mean error.

4.3 Data-Driven MPRR Dynamic Model Development

This section presents the second approach to model MPRR at RCCI engines using a data-driven modeling. Data-driven modeling approaches can provide a reasonably accurate estimations without any knowledge of underling physics. This will significantly accelerate the modeling process compared to physics based approach since the development of high-fidelity physical equations requires tedious calibration. Therefore, a data-driven approach based on Keneralized Canonical Correlation Analysis (KCCA) is employed in this section. This approach is explained in details at Section 3.2 and presents a state-space dynamic model for an LPV system as shown in Eq. (4.8).

$$X_{k+1} = A(p_k)X_k + B(p_k)U_k + K(p_k)E_k, \tag{4.8a}$$

$$Y_k = C(p_k)X_k + E_k, \tag{4.8b}$$

where, U_k, Y_k, represent the inputs, the outputs, respectively. X_k denotes unknown states at discrete-time instant k. Matrices $A(p_k)$, $B(p_k)$, $K(p_k)$ and $C(p_k)$ denote LPV state-space matrices dependent on scheduling variables p_k. E_k notes additive Gaussian white noise. Eq. (4.8) can be updated by $E_k = Y_k - C(p_k)X_k$ to form state space model presented by Eq. (4.9).

$$X_{k+1} = \widetilde{A}(p_k)X_k + \widetilde{B}(p_k)U_k + K(p_k)E_k, \tag{4.9a}$$

$$Y_k = C(p_k)X_k + E_k, \tag{4.9b}$$

where $\widetilde{A}(p_k)$ and $\widetilde{B}(p_k)$ are represented by $B(p_k) - K(p_k)D(p_k)$ and $A(p_k) - K(p_k)C(p_k)$, respectively. $\widetilde{A}(p_k)$, $\widetilde{B}(p_k)$, $K(p_k)$ and $C(p_k)$ can be defined based on support vector weighting matrices and feature maps:

$$\tilde{A}(p_k) = W_1\Phi_1(p_k); B(p_k) = W_2\Phi_2(p_k) \tag{4.10a}$$

$$K(p_k) = W_3\Phi_3(p_k); C(p_k) = W_4\Phi_4(p_k) \tag{4.10b}$$

where unknown support vector weighting matrices are shown by $W_{1,2,3,4}$ and unknown feature maps are represented by $\Phi_{1,2,3,4}$. A SVM based discrete-time state-space model can be represented by Eq. (4.11).

$$X_{k+1} = W_1\Phi_1(p_k)X_k + W_2\Phi_2(p_k)U_k + W_3\Phi_3(p_k)Y_k, \tag{4.11a}$$

$$Y_k = W_4\Phi_4(p_k)X_k. \tag{4.11b}$$

State-space matrices can be obtained from feature maps and weighting matrices as presented at Eq. (4.12). [82]

$$\tilde{A}_e(\cdot) = W_1\Phi_1(\cdot) = \sum_{k=1}^{N} \alpha_k x_k^T \bar{k}^1(p_k, \cdot) \tag{4.12a}$$

$$B_e(\cdot) = W_2\Phi_2(\cdot) = \sum_{k=1}^{N} \alpha_k u_k^T \bar{k}^2(p_k, \cdot) \tag{4.12b}$$

$$K_e(\cdot) = W_3\Phi_3(\cdot) = \sum_{k=1}^{N} \alpha_k y_k^T \bar{k}^3(p_k, \cdot) \tag{4.12c}$$

$$C_e(\cdot) = W_4\Phi_4(\cdot) = \sum_{k=1}^{N} \beta_k x_k^T \bar{k}^3(p_k, \cdot) \tag{4.12d}$$

where α and β are Lagrangian multipliers and $\bar{k}^i(p_j, p_k)$ is Gaussian kernel function presented at Eq. (4.13).

$$\bar{k}^i(p_j, p_k) = exp(-\frac{||p_j - p_k||_2^2}{2\sigma_i^2}), \tag{4.13}$$

σ_i denotes the standard deviation and $||.||_2$ is representing the l_2 norm. The defined Gaussian function is used in this LPV modeling approach to perform kernel trick. Computed $\tilde{A}_e(.), B_e(.), K_e(.)$, and $C_e(.)$ matrices at Eq. (4.12) can be included in Eq. (4.1) to represent the data driven state space dynamic model of the plant.

The explained data-driven algorithm was implemented to experimental data from the RCCI engine. Input PR, FQ, and *n*-heptane SOI were varied and MPRR was computed from acquired pressure traces. Fig. 4.1 presents a sample of the

experimental data obtained from the RCCI engine. The collected experimental data were divided into training and test data sets. The training data set which consists of 65% of data is used to train the KCCA-LPV model and the remaining 35% is reserved as the test data. Since the number of unknown states is a parameter that can be adjusted to obtain the best results, a study was conducted to learn the effect of the number of states on the estimation accuracy. Fig. 4.4 presents the effect of unknown state number on estimation accuracy. It can be observed that by an increasing number of states, estimation error decreases and reaches an almost constant value. In this research, the number of unknown states is selected to be six where high estimation accuracy can be achieved while avoiding the high computational costs associated with higher state numbers.

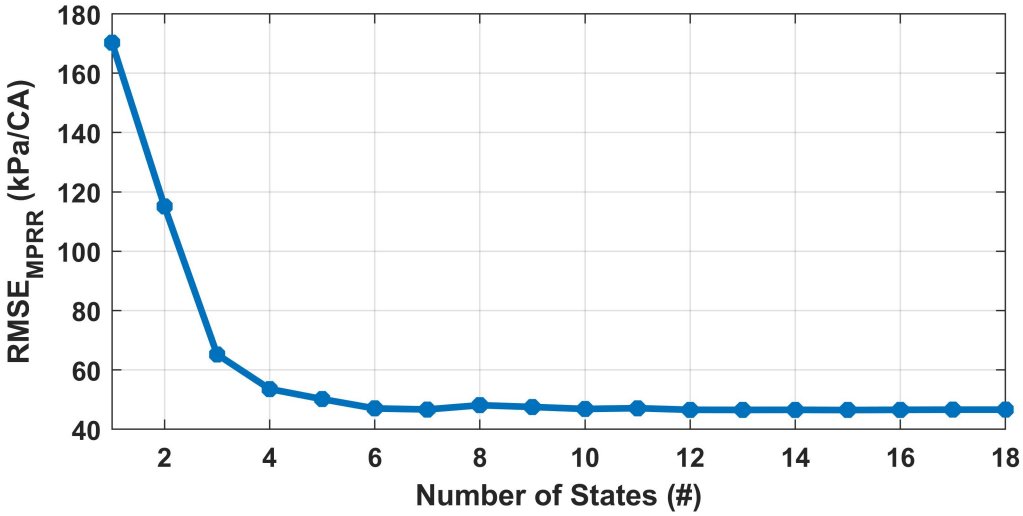

Figure 4.4: Effect of unknown states number on KCCA MPRR model prediction accuracy.

The state-space dynamic model of the MPRR is structured and presented at Eq.

(4.14). Dependency of identified $\tilde{A}_e$ and B_e matrices' on the fuel quantity as the scheduling parameter are presented at Fig. 4.5. Variation of elements proves that the identified model is an LPV representation of the RCCI dynamics.

$$\begin{bmatrix} X_1 \\ X_2 \\ X_3 \\ X_4 \\ X_5 \\ X_6 \end{bmatrix}_{(k+1)} = \tilde{A}_e(FQ) \begin{bmatrix} X_1 \\ X_2 \\ X_3 \\ X_4 \\ X_5 \\ X_6 \end{bmatrix}_{(k)} + B_e(FQ) \begin{bmatrix} FQ \\ SOI \\ PR \end{bmatrix}_{(k)} \tag{4.14a}$$

$$[MPRR]_{(k+1)} = C(FQ) \begin{bmatrix} X_1 X_2 X_3 X_4 X_5 X_6 \end{bmatrix}^T_{(k+1)}, \tag{4.14b}$$

The developed KCCA-LPV model is then used to estimate the experimental MPRR values. Fig. 4.6 presents estimation results for the KCCA-LPV model at three PR values. It demonstrates that the developed KCCA-LPV model can estimate the experimental MPPRs with an average estimation error equals to 45.4 kPa/CA which is significantly lower than the physics-based estimation error. Fig. 4.7 presents the comparison between MPRR estimation of the two models at PR=14, PR=20, and PR=12. The root mean square error of the physics-based model is 63.8 kPa/CA, 66.9 kPa/CA, and 87.1kPa/CA for PR=14, PR=20, and PR=28, respectively. On the

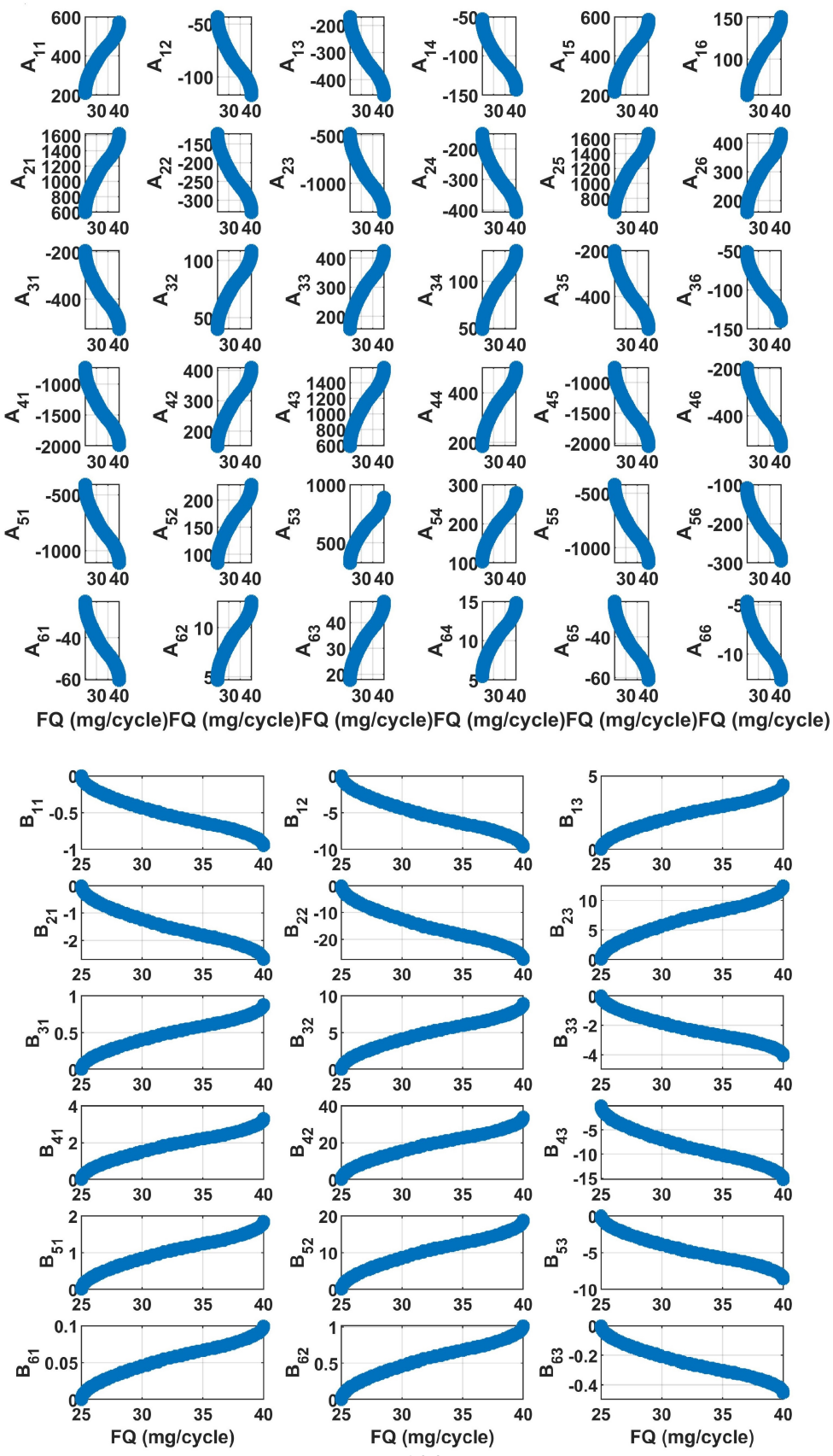

Figure 4.5: Dependency of identified A and B matrices elements at KCCA-LPV method on scheduling parameter

other hand, the data-driven model could estimate the experimental data at PR=14, PR=20, and PR=28 with an average error of 27.9 kPa/CA 28.3 kPa/CA ,and 47.6 kPa/CA. It can be observed that the data-driven method can estimate the measured MPRR values with better accuracy compared to the physics-based method while requiring less development time.

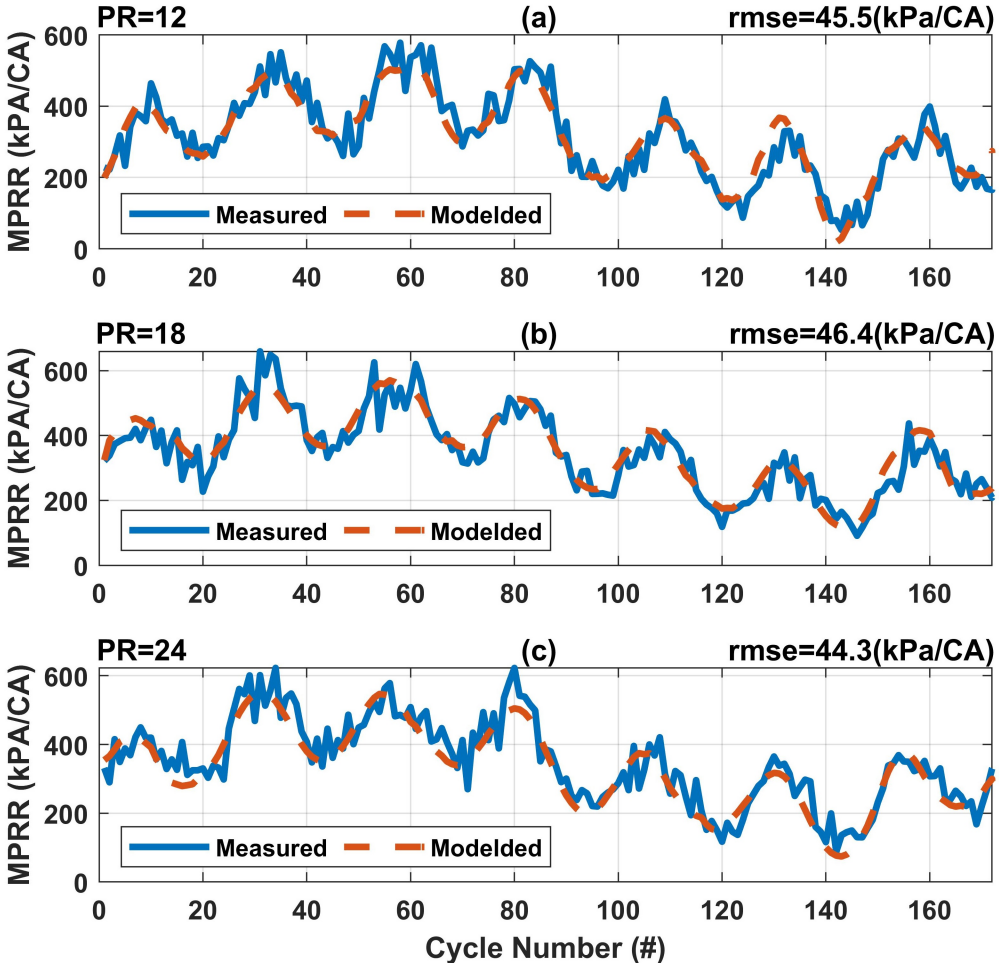

Figure 4.6: MPRR prediction performance of the identified KCCA-LPV model at $T_{in} = 333$ K, $N = 1200$ RPM, $P_{in} = 96.5$ kPa and (a) PR=12, (b) PR=18, (c) PR=24.

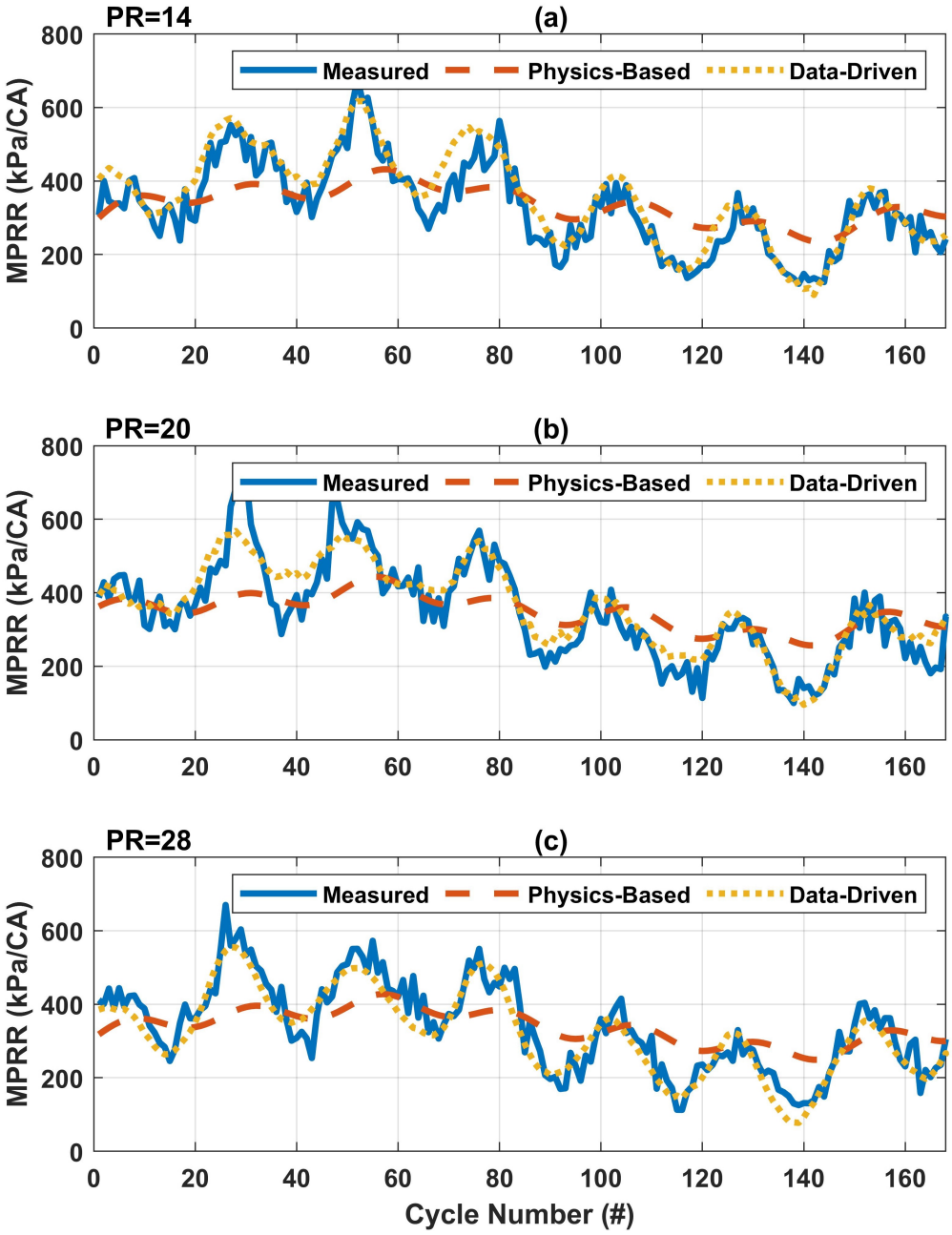

Figure 4.7: Estimation performance of the physics-based and data-driven MPRR models at $T_{in} = 333$ K, $N = 1200$ RPM, $P_{in} = 96.5$ kPa (a) PR=14, RMSE Physics-Based=63.8 kPa/CA, RMSE Data-Driven=27.9 kPa/CA (b) PR=20, RMSE Physics-Based=66.9 kPa/CA, RMSE Data-Driven=28.3 kPa/CA. (c) PR=28, RMSE Physics-Based=87.1 kPa/CA, RMSE Data-Driven=47.6 kPa/CA.

4.4 Summary and CONCLUSIONS

This research developed and validated two control-oriented MPRR models for an RCCI engine at APS labs. The first MPRR model is developed based on a physics-based method while the second model is obtained through a data-driven modeling approach. Test results showed that the physics-based MPRR model can estimate experimental MPRR with a mean estimation error equals to 87 kPa/CAD. The second MPRR model was developed through a data-driven KCCA-LPV identification approach. In this method, unknown states are estimated by the KCCA method and state-space representations of the RCCI combustion dynamics are computed by the LPV method. The developed data-driven MPRR model could estimate the experimental MPRR values with an average error equal to 47 kPa/CAD. This research can be advanced by the implementation of the designed control framework on the engine experimental setup.

Chapter 5

Data-driven Identification of Reactivity and Stratification Dynamics at RCCI Engines Based on Kernel Canonical Correlation Analysis

5.1 Introduction

it is difficult to run RCCI engines at their optimal conditions due to dependency of their combustion on reactivity formation. The reactive pockets formation at

these engines is determined by fuel, oxygen, and temperature stratification which are difficult be measured and controlled experimentally. Computational Fluid Dynamic (CFD) models coupled with chemical kinetics solvers can be used to model those stratification and consequently reactivity formation. These CFD models can provide in-depth understanding about combustion processes, however, they are not appropriate for real-time control applications due to constraints on real-time processing power and their computationally expensive nature. Data-driven methods can be used to address this challenge by learning from the CFD-chemical kinetics models' results and providing computationally fast models. This study aims to model stratification and reactivity in RCCI engines using a data-driven learning approach, implemented on an experimentally validated CFD model. The developed model can be used to control reactivity and run RCCI engines at their optimal operational points.

This study has the following structure. The experimental setup is explained in Section 2, and the development and validation of the CFD model of the RCCI engine is explained in Section 3. Section 4 discusses the reactivity metric development. Section 5 explains the stratification index quantification method. Section 6 provides the overview of data driven method which is used to model reactivity and stratification dynamics. Finally, Section 7 summarizes this study and presents the conclusions.

5.2 CFD Model Development

A computational fluid dynamic model for the RCCI engine was created and verified in this work. The RCCI engine's surface geometry was 3D scanned and CATIA software was utilized to develop the 3D geometry model from the scanner's point clouds. Fig. 5.1 illustrates the RCCI engine's developed geometry. After being verified using the engine's compression ratio, the geometry was imported into CONVERGE CFD software. Engine specifications, which are shown in Table 1.2 were used as the basis for the CFD model's creation at CONVERGE CFD software. The initial conditions were established using intake manifold pressure gauge and thermocouples measurements. The CFD model and its sub-models are described in the Table 5.1.

Table 5.1
CFD Model Specifications

Chemical Mechanism	Chalmars,171 Species
Number of Regions	5
Number of Boundaries	17
Solver Type	Successive Over Relaxion
Time Step Type	Variable
Spray Model	Kelvin-Helmholtz, Rayleigh-Taylor
Evaporation Model	Frossling
Collision Model	NoTime Counter
Fuel, Wall interaction	Rebound, Slide
Combustion Model	SAGE
Turbulence Model	RNG k-ϵ
Wall Heat Transfer model	O'rouke, Amesden
Base Grid Size	1 [mm]

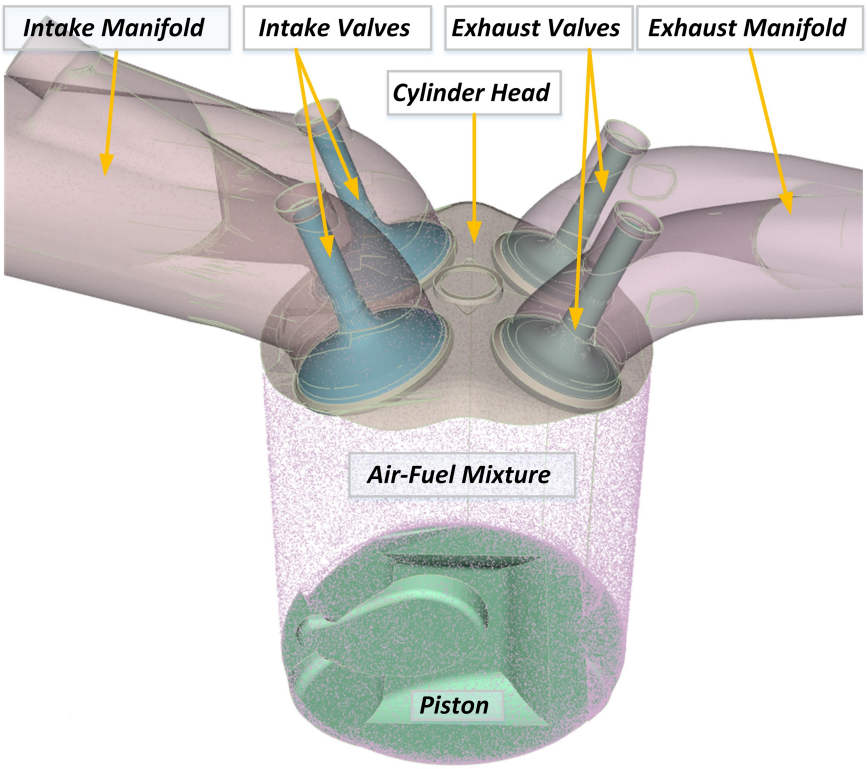

Figure 5.1: Open cycle CFD model geometry of the RCCI engine

Using experimental pressure trace data from the RCCI engine, the CFD model was subsequently validated. The validation procedure was carried out for eight RCCI operating points in steady state mode. Validated steady state points are shown in the Table 5.2. Eight steady state points were chosen to cover the CFD model's validation plan. Fig. 5.2 shows the sample validation outcome for matching in-cylinder gas pressure trace of one of the the steady state points. The validation result demonstrates that simulation pressure trace could capture the experimental pressure trace with root mean square error (rmse) of 89.2 (kPa) which is reasonably close estimation. The rmse values for the other validation points are presented in Table

5.3.

Point	FQ (mg/cycle)	SOI (CAD bTDC)	PR (-)
1	39.2	55.0	30
2	25.7	55.0	30
3	27.3	55.0	10
4	39.6	55.0	10
5	40.3	34.5	30
6	25.6	34.5	30
7	39.3	35.0	10
8	25.6	34.7	10

Table 5.2
Fuel Quantity (FQ), Start of Injection (SOI) and Premixed Ratio (PR) of Steady State Validation Points

Table 5.3
Root Mean Square Error of Steady State Validation Points

Point	RMSE (kPa)
1	89.2
2	67.7
3	102.3
4	75.6
5	77.3
6	81.6
7	98.3
8	82.6

Transient engine cycles were also used to evaluate the CFD model. The operational conditions of these transient cycles are listed in Table 5.4. Results for transient verification of five continuous engine cycles are displayed in Fig. 5.3 which shows that the transient experimental pressure traces can be properly predicted by the CFD model with rmse of estimation equal to 96.3 (kPa). Later, this verified CFD model is utilized to get the data from inside the combustion chamber that is not feasible

to collect using experimental techniques. These data will be utilized to develop the data-driven model and estimate the reactivity and stratification levels.

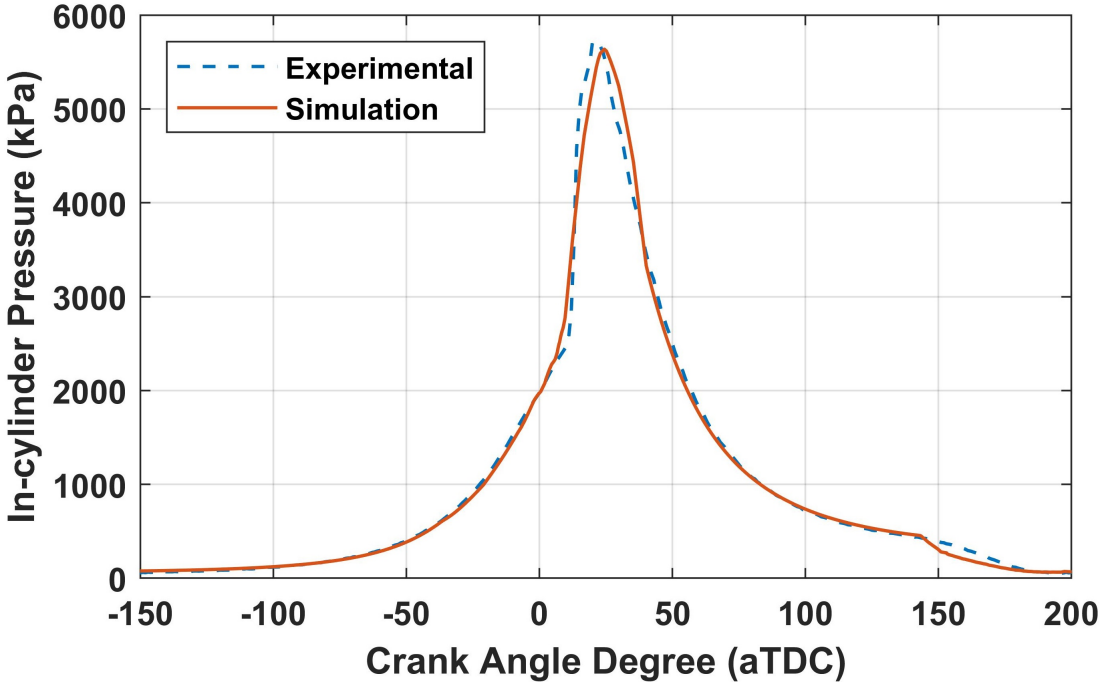

Figure 5.2: Steady state open cycle CFD model validation, PR=30 , SOI=55 CAD bTDC, FQ=39.2 mg/cycle

Cycle	FQ (mg/cycle)	SOI (CAD bTDC)	PR (-)
1	39.6	36	18
2	31.6	39.6	18
3	29.7	41.9	18
4	27.4	53.3	18
5	25.7	55.0	18

Table 5.4
Transient Validation Test Points

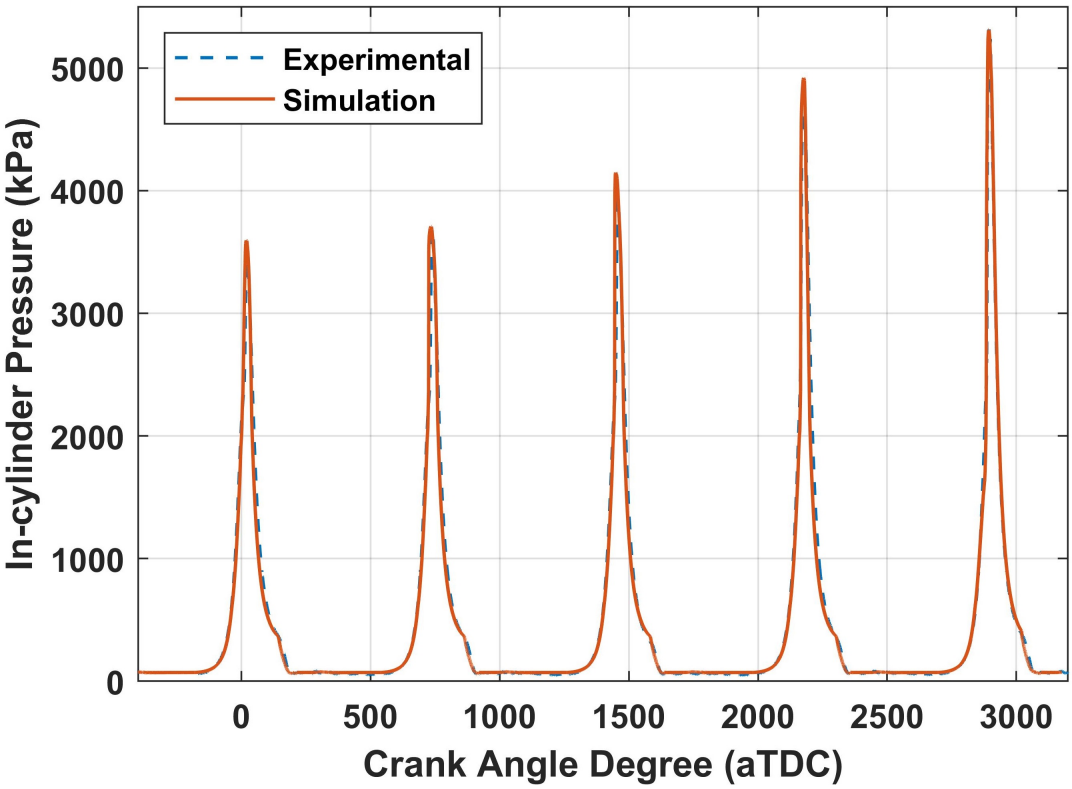

Figure 5.3: Transient open cycle CFD model validation for engine cycles listed in Table 5.4

5.3 Reactivity Metric Development

In this paper, a reactivity model for iso-octane, n-heptane, and air mixtures under engine-relevant circumstances is established. The relationship between reactivity and ignition delay is inverse. In this work, reactivity is modeled as an inverse function of observed ignition delay using this connection. To create a constant volume homogeneous reactor for measuring ignition delay, CONVERGE CFD software is used. This model is simulated for a cube with 1 mm-long edges. Table 5.5 provides

the reactor model's details. The reactor charge is defined as a fuel-air mixture with the desired starting condition, and the hydroxyl content is tracked.

Table 5.5
Reactor Model Specifications

Combustion Model	SAGE
Turbulance Model	RNG-ϵ
Chemical Mechanism	Chalmers C_7H_{16}
Boundary Condition	Stationary
Heat Transfer Condition	Adiabatic

The the start of combustion is marked by a rise observed in the concentration of hydroxyl. Fig. 5.4 depicts the hydroxyl concentration trace during a sample course of the reactor simulation. After the simulation begins, the hydroxyl content stays at zero until abruptly rising to 1.2 (ppm) at 11 (msec). The ignition delay is the length of time from the beginning of the simulation until this point, when there is a sudden increase caused by the ignition of combustion. Later, the produced hydroxyl interacts with other intermediary spices and slowly diminishes.

Experimental shock tube ignition delay data obtained by Ciezki et. al. ([2]) were used to validate the established reactor model in this study. The comparison of experimental shock tube ignition delays and ignition delay prediction using the CONVERGE reactor model is shown in Fig. 5.5. It demonstrates that an experimental ignition delay could be estimated using the reactor model with the root mean square error of 0.891 msec in . The estimation error at the lower temperature

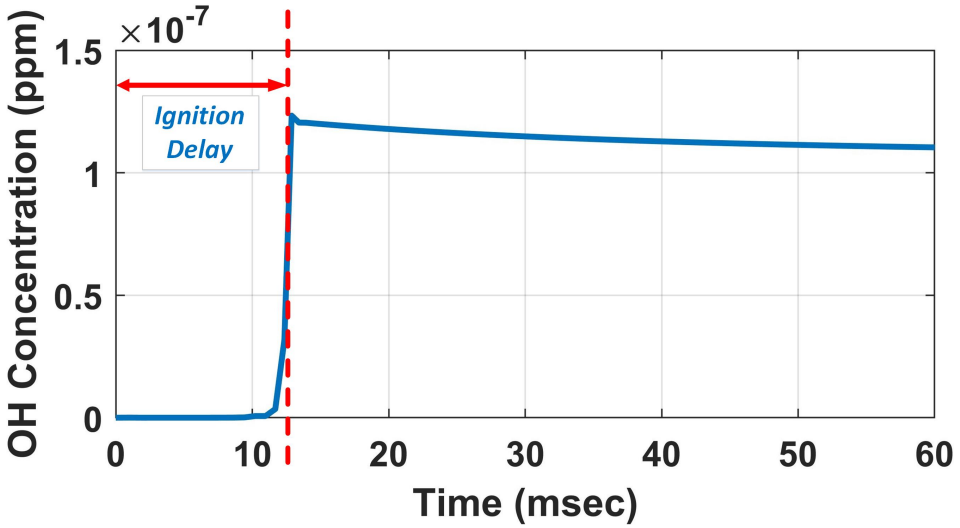

Figure 5.4: Hydroxyl concentration trace during homogeneous reactor simulation for initial pressure and temperature at $P_{initial}$=14 bar, $T_{initial}$=700 K, respectively and initial mixture mass fraction concentrations of y_{N_2}=0.73, y_{O_2}=0.22, $y_{C_8H_{18}}$=0.0.008, $y_{C_7H_{16}}$=0.0.028

part is 0.271 msec. The established ignition delay model will be accurate enough to predict ignition delay for the RCCI combustion regime because the RCCI engine has a low temperature combustion regime. It was required to run this model for numerous combinations of input conditions because the goal of this research is to generate a reactivity model for a broad range of engine-relevant chemical and temperature variables. To automate the simulation procedure in this investigation, the CONVERGE CFD reactor model was connected with MATLAB. For updating the reactor's initial conditions, beginning reactor simulation, and figuring out ignition delay based on simulated hydroxyl trace, a MATLAB script code was created. Engine conditions near to the TDC moment are considered to be relevant initial conditions. 25,000 examples using various temperatures, pressures, fuels, and air concentrations were tested using the CONVERGE CFD model. Ignition delay measurements were

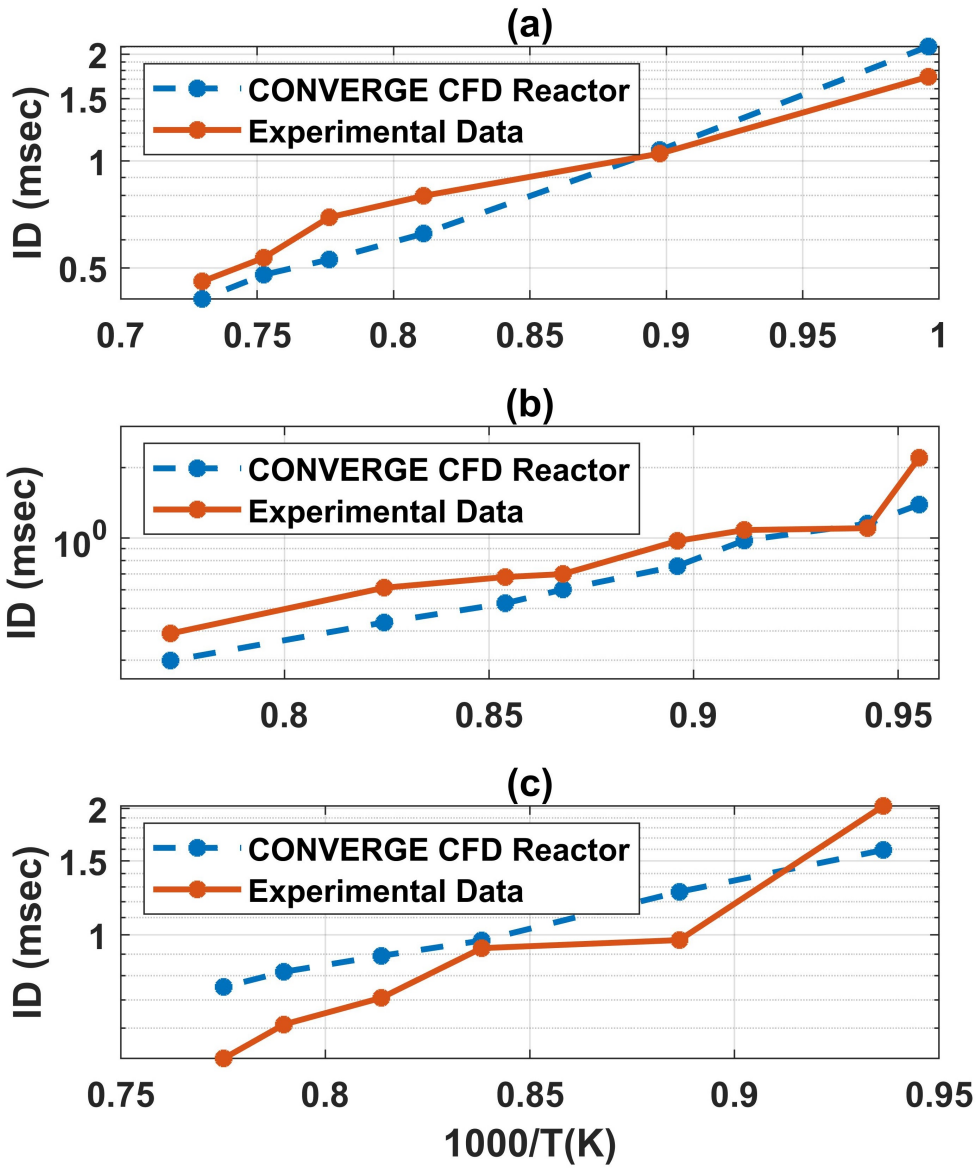

Figure 5.5: Ignition delay (ID) validation at $P_{initial}$=10 bar and three different fuel-air equivalence ratios at (a) ϕ=0.7, (b) ϕ=1, (c) ϕ=1.3, based on experimental data reported by the study in [2]

taken as a function of iso-octane, n-heptane, oxygen concentrations, and mixture temperature and pressure to create an ignition delay model.

The simulated ignition delay (ID) values from the reactor model are shown in Fig.

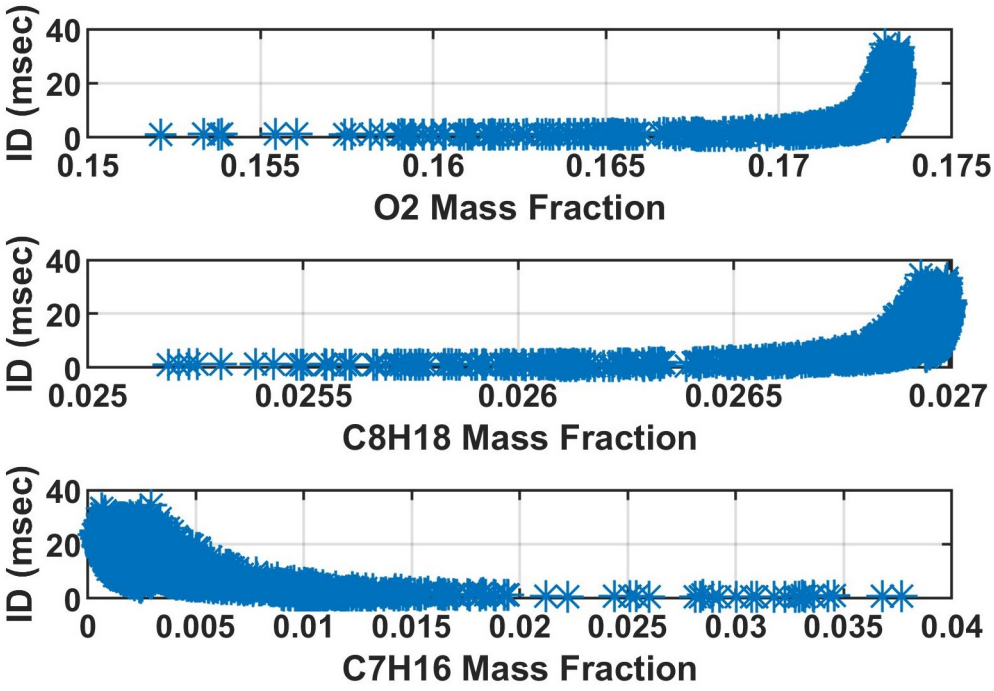

Figure 5.6: Simulated Reactor model Ignition Delay (ID) for operating condition

5.6. They are based on the variation of reacting species concentrations. This figure indicates that mixtures with lower oxygen and iso-octane concentrations or greater n-heptane concentration will have reduced ignition delays, compared to other conditions. Additionally, it shows that there is a nonlinear relationship between ignition delay and the mass fraction of reacting species. To this end, the multi-linear regression (MLR) method by Ryan et. al.'s [87] multiple linear regression method is used to generate RCCI ignition delay equations. Using this method, the ignition delay (ID) is represented by Eq. (5.1).

$$ID = b_0(y_{O_2})^{b_1}(y_{fuel})^{b_2}(P)^{b_3}e^{(b_4/T)} \tag{5.1}$$

Where y_{O_2}, and y_{fuel} indicate the mixture mass fraction of oxygen and fuel, respectively. P and T denote mixture pressure and temperature, respectively. The MLR approach was used to derive the equation coefficients as b_0, b_1, b_2, b_3, and b_4 from the collected ignition delays from the reactor model results at Fig. 5.6. It was discovered that it would be difficult to represent all engine-relevant conditions using a single equation. As a result, two ignition delay equations based on the association between temperature and n-heptane mass fraction values were established. Eq. (5.2) presents the resulting ignition delay correlations.

$$if\ y_{C7H16} > 1.4 \times 10^{-5}T + 0.035$$

$$ID = e^{-2.86}(y_{O_2})^{-1.96}(0.062{\times}y_{C8H18} + 0.937{\times}y_{C7H16})^{-1.78}$$

$$(P)^{-0.94}e^{(11405/T)}, \tag{5.2a}$$

$$if\ y_{C7H16} \leq 1.4{\times}10^{-5}T + 0.035$$

$$ID = e^{197.7}(y_{O_2})^{1443.7}(0.062{\times}y_{C8H18} + 0.937{\times}y_{C7H16})^{823.49}$$

$$(P)^{-0.60}e^{(12092/T)} \tag{5.2b}$$

Fig. 5.7 compares the ignition delay estimation of Eq. (5.2) to the ignition delay results of the reactor model. It demonstrates that the ignition delays of the reactor model can be predicted by MLR equations with a high estimation accuracy of 0.97 as the coefficient of determination (R^2). To avoid computationally expensive simulation

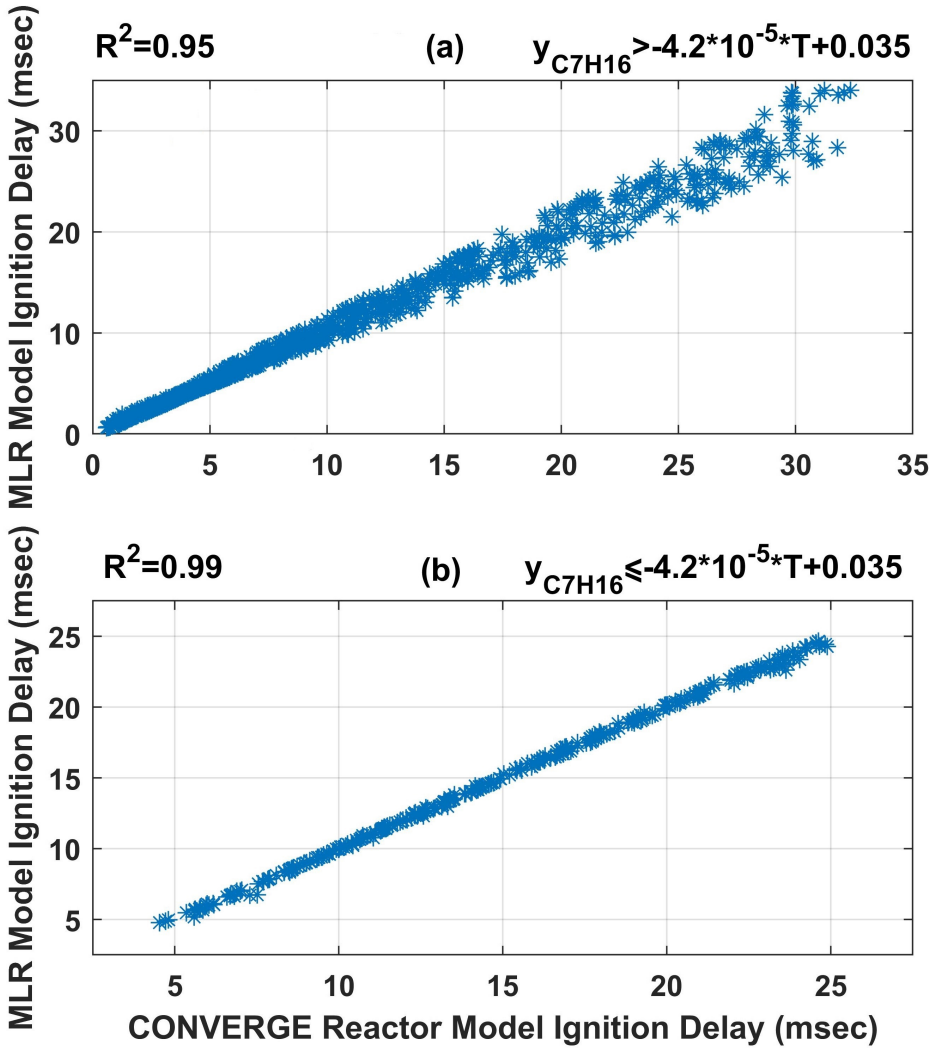

Figure 5.7: Validation for multiple linear regression (MLR) ignition delay two Equations at $P_{initial}$=10 bar

of the reactor model, the fast MLR ignition delay equations were implemented using thermal properties of the CFD model cells which determined the distribution of ignition delays inside the combustion chamber.

In this study, a new metric denoted as the relative relativity index (RRI) is defined based on the comparison between the ignition delay and the RCCI engine's earliest

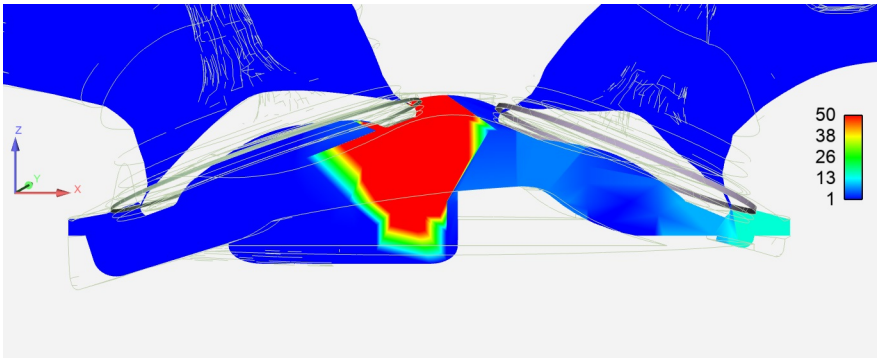

Figure 5.8: Relative reactivity index distribution inside combustion chamber at 2 CAD bTDC, PR=20 , SOI=40 bTDC, FQ=3.5 mg/cycle

injection timing, i.e. 55 CAD bTDC. This earliest injection timing can vary from one combustion mode to another and can be used adjust the RRI correlation to each operation. The RRI for the RCCI engine is given in Eq. (5.3).

$$RRI = \frac{55}{6\times10^{-6}\times N\times ID} \tag{5.3}$$

Where the N is engine's rotational speed, and the predicted ignition delay is shown by ID which is obtained from Eq. (5.2). In this research, the combustion chamber's reactivity status is measured using the relative reactivity index. The RRI distribution inside the RCCI CFD model is shown in Fig. 5.8. Reactivity is substantially higher in the middle of the combustion chamber than in the nearby areas, which indicates at what locations the combustion is about to occur.

Figures 5.9, 5.10, and 5.11 present effect of control actions on reactivity distribution within the combustion chamber. Effect of fuel quantity on reactivity distribution is shown in Fig. 5.9 for three different fuel quantities. Increasing fuel quantity from 2

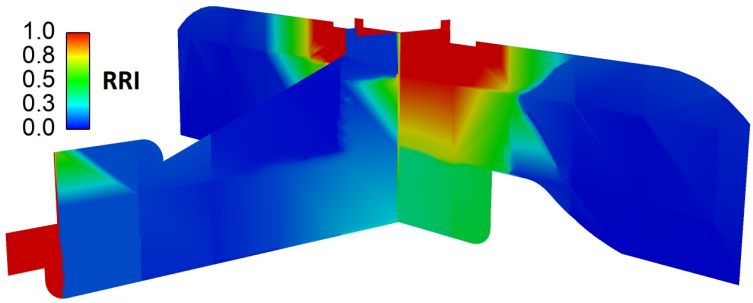

(a) FQ=2 mg/cycle

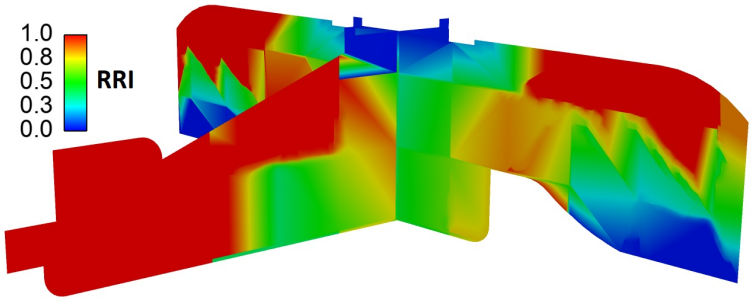

(b) FQ=4 mg/cycle

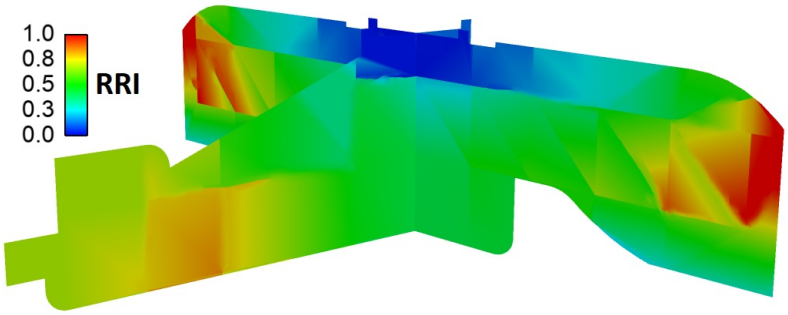

(c) FQ=6 mg/cycle

Figure 5.9: Relative Reactivity Index (RRI) distribution at PR=20, SOI=55 CAD bTDC, and (a) FQ=2 mg/cycleC, (b) FQ=4 mg/cycle, (c) FQ=6 mg/cycle

to 4 mg/cycle increases the overall reacivity inside the combustion chamber, however increasing to 6 mg/cycle decreases the reactivity levels. This is indication that reacivity depends on appropriate ratio between fuel and air. Lower fuel quantities will leave mixture with more oxygen and consequently reduces reactivity levels. Higher

fuel quantities replaces oxygen and the air-fuel mixture will not have adequate oxygen to form a reactive mixture. Fig. 5.10 demonstrates effects of varying SOI timing for the DI injected fuel on reactivity distribution. This effect can be explained by considering the location of direct injector which is positioned at the left side of the combustion chamber and directed at piston and wall corner at the other side of the combustion chamber. Fig 5.10(a) shows reactivity distribution for a late injection timing at 15 CAD bTDC. This shows high reactive mixture formation at left side of the view and very low reactive regions at the far right regions. The injected fuel had a limited time to penetrate and evaporate inside the combustion chamber and consequently only the regions close to the injector received adequate fuel to form a reactive mixture. Regions at far right are not reactive since the injected fuel could not reach to them within the short available time. Fig 5.10(b) presents reactivity distribution for the SOI at 35 CAD bTDC. Advancing SOI timing to 35 CAD bTDC provides the injected fuel with an extra 20 CAD to penetrate and evaporate inside the combustion chamber. The effect of this extra time can be observed in Fig 5.10(b) though expanded reactive regions at the left side of the combustion, formation of reactive rigions at the core of chamber and shrinkage of non-reactive rigions at the far right side. Fig. 5.10(c) demonstrates reacivity distribution for an advanced injection timing at 55 CAD bTDC. Injecting DI fuel at a very advanced timing provides ample time for the fuel to be evenly distributed inside the combustion chamber and also alwyas for the fuel to reach far right rigions within the combustion

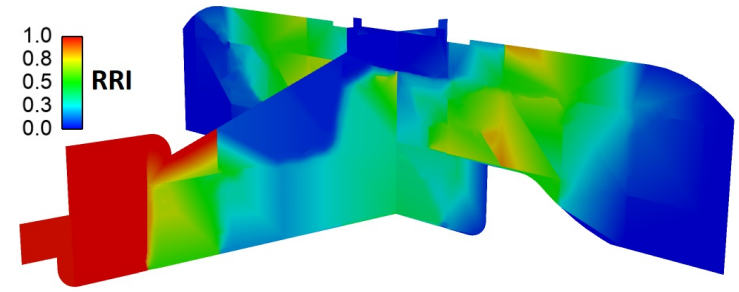

(a) SOI=15 CAD bTDC

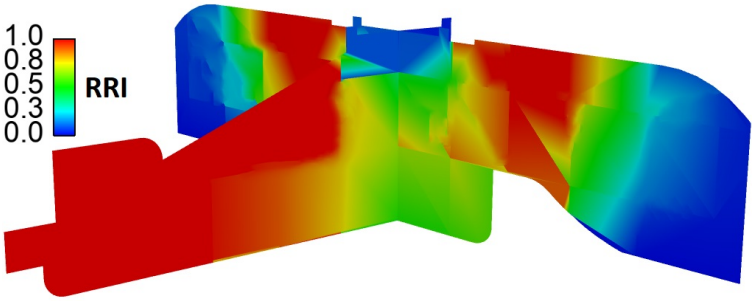

(b) SOI=35 CAD bTDC

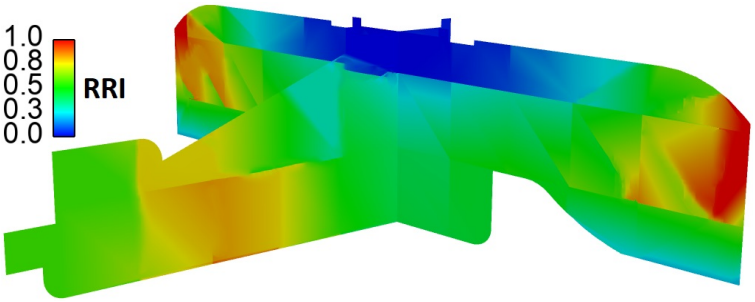

(c) SOI=55 CAD bTDC

Figure 5.10: Relative Reactivity Index (RRI) distribution at PR=20, FQ=4 mg/cycle, and (a) SOI=15 CAD bTDC, (b) SOI=35 CAD bTDC, (c) SOI=55 CAD bTDC

chamber. This condition can be observed in Fig. 5.10(c) where most rigions show an averaged reacivity level. Moreover, a high reactive rigion at the far right side of the combustion chamber is visible since advanced injection timing (i.e. SOI=55 CAD bTDC) facilitated fuel delivery to far right regions.

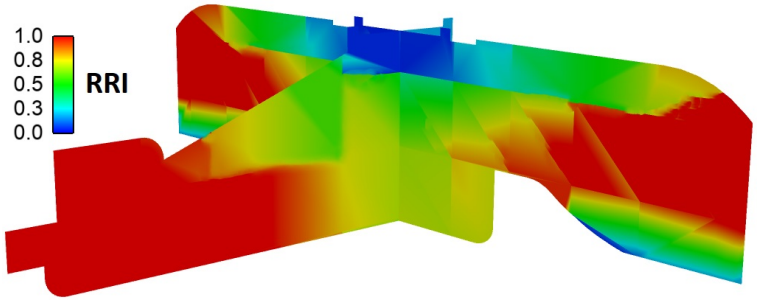

(a) PR=00

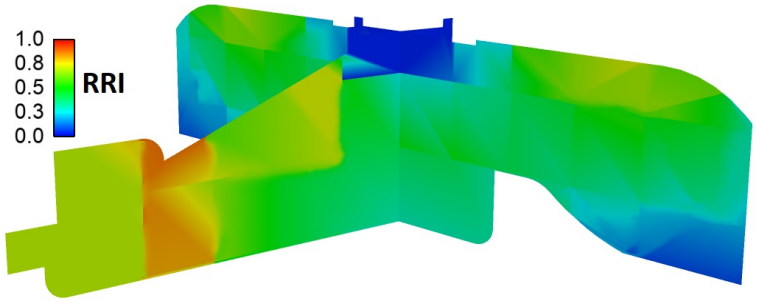

(b) PR=30

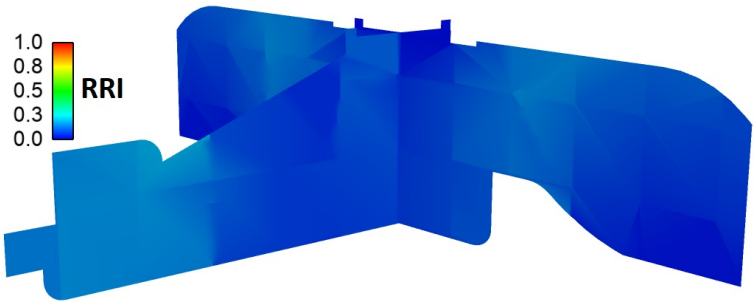

(c) PR=50

Figure 5.11: Relative Reactivity Index (RRI)distribution at SOI=45 CAD bTDC, FQ=4 mg/cycle, and (a) PR=0, (b) PR=30, (c) PR=50

Fig. 5.11 demonstrates the effect of adjusting premixed ratio on reactivity levels within the combustion chamber. Increasing premixed ratio, reduces the injected high reactive fuel quantity and increases the low reactive fuel quantity. It is expected that overall reacivity of mixture to decrease due to the increase of premixed ratio. Reactivity contour result at Fig. 5.11 confirm this expectation. Fig. 5.11(a) shows the

reactivity distribution inside the combustion chamber for PR=0 which includes very high reactive regions. Fig. 5.11(b) presents reactivity distribution results for PR= 30. It is clear that increasing PR to 30 resulted in significantly reduced high reactive regions and caused an increase in moderately reactive regions and low reactive regions sizes. This is because reduced injection of high reactive fuel resulted in reduced chamber reactivity. This reactivity reduction trend is also visible at Fig. 5.11(c) where PR is increased to 50 and reactivity levels are significantly dropped due to replacement of high reactive fuel with the low reactive fuel.

5.4 Stratifiction Metric Development

The second parameter examined in this study was fuel stratification. In the combustion chamber, this parameter measures the fuel-air mixture gradients. The least stratified engines are homogenous charge compression ignition (HCCI) engines, which also operate with almost homogeneous fuel-air mixtures [88]. On the other hand, mixing controller combustion engines operate with the largest stratifications [88].The mixing level is quantified in this study by using a stratification index (SI) based on the distribution of fuel mass fractions. In accordance with Eq. (5.5), the SI for the combustion chamber is determined as the volumetric average of the fuel mass

fraction differential between the cells and the homogenous mixture.

$$SI_i = |(y_{fuel,i} - y_{fuel,homogenous})| \tag{5.4}$$

$$SI = \sum_{n=1}^{n_{tot}} \frac{V_i}{V_{tot}} SI_i \tag{5.5}$$

Where the cell's volume and fuel mass fraction are v_i and $y_{fuel,i}$, respectively. The total number of cells in the combustion chamber is n_{tot}, and the volume of the combustion chamber is V_{tot}. The symbol $y_{fuel,homogenous}$ stands for the fuel mass fraction for a virtual homogeneous cell and Eq.(5.6) provides its definition.

$$y_{fuel,homogenous} = \frac{m_{C_8H_{18}} + m_{C_7H_{16}}}{m_{C_8H_{18}} + m_{C_7H_{16}} + m_{air}} \tag{5.6}$$

Where $m_{C_8H_{18}}$, $m_{C_7H_{16}}$, and m_{air} represent the total mass of iso-octane, n-heptane, and air inside the combustion chamber. Fig. 5.12 depicts the distribution of local stratification throughout the combustion chamber at 180 CAD bTDC. This crank angle is selected to represent a stratified mixture before the mixing process occurs during the compression stage. It is obvious that the stratification values are higher in the areas around the intersection of the piston and cylinder wall. In comparison to homogenous conditions, these areas receive less fuel, resulting in stratified mixtures. In contrast, the core of the combustion chamber has less stratification since there is fuel available from injection and the mixture has become homogeneous.

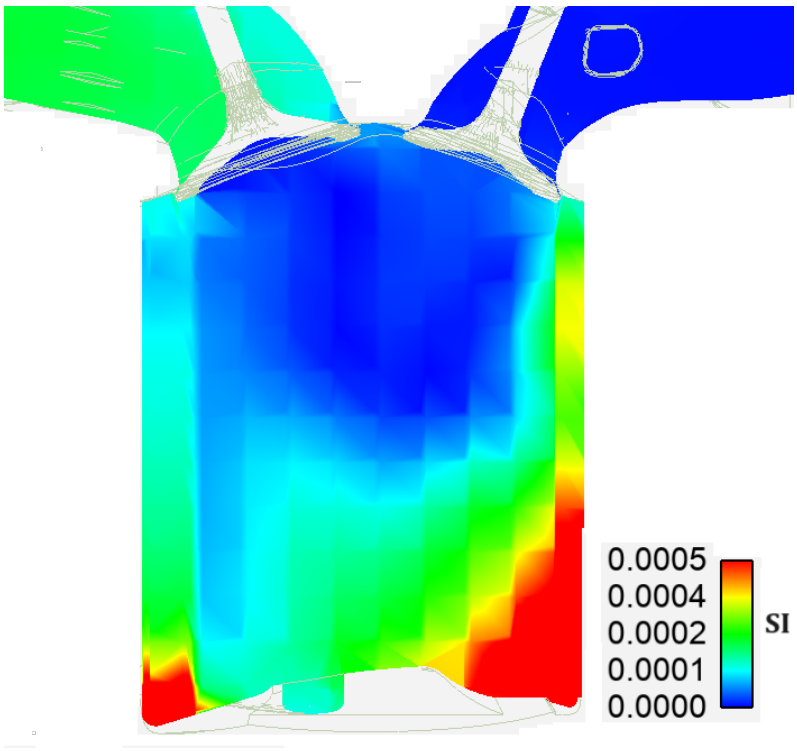

Figure 5.12: Local Stratification index distribution inside combustion chamber at 180 CAD bTDC, PR=20, SOI=40 bTDC, FQ=3.5 mg/cycle

In this study, effect of adjusting fuel quantity, injection timing of high reactive fuel, and premixed ratio on fuel stratification inside the combustion chamber is studied. Fig. 5.13 shows local stratification contours for three fuel quantity levels. Higher fuel quantities require more time to form a homogeneous mixture with the air. This is due to increased evaporation and mixing time of the injected fuel. Fig. 5.13(a) shows the local stratification distribution for FQ=2 mg/cycle. Lower values of the stratification index demonstrate a low stratified mixture. Fig. 5.13(b) demonstrates the stratification results for FQ=4 mg/cycle operation. It is clear that stratification levels are higher compared to the FQ=2 mg/cycle which is expected based on higher required mixing and evaporation time. The stratification level is even higher at

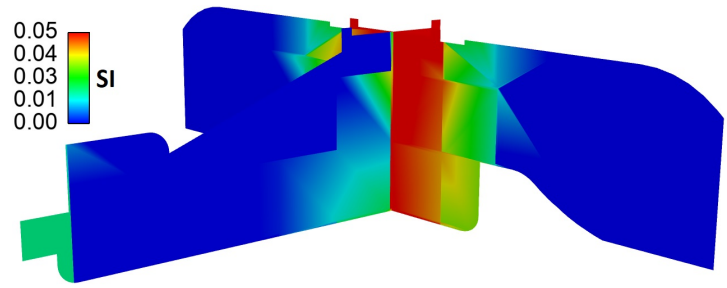

(a) FQ =2 mg/cycle

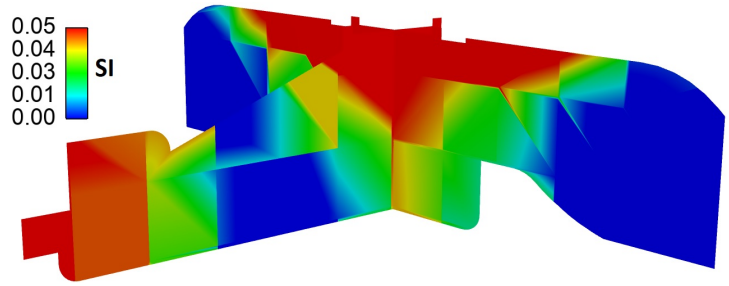

(b) FQ =4 mg/cycle

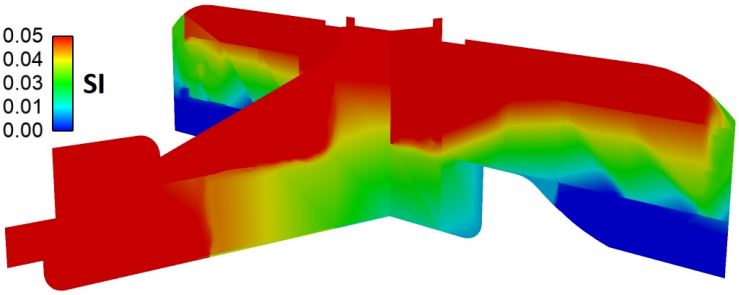

(c) FQ =6 mg/cycle

Figure 5.13: Stratification distribution at PR=20, SOI=55 CAD bTDC, and (a) FQ=2 mg/cycle, (b) FQ=4 mg/cycle, (c) FQ=6 mg/cycle

FQ=6 mg/cycle which is shown at Fig. 5.13(c). These results demonstrate that increasing fuel quantity will result in higher stratified mixture inside the combustion chamber. Another series of simulations were study was conducted to understand effect of injection timing of high reactive fuel on stratification levels. Results for these simulations are presented in Fig. 5.14. The results show advancing injection timing provides more mixing time for the fuel and consequently leading to less stratified

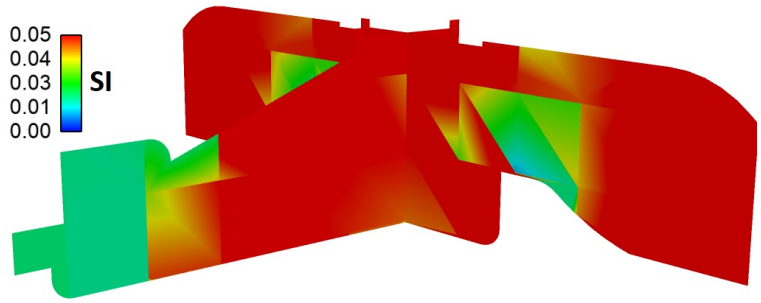

(a) SOI=15 (CAD bTDC)

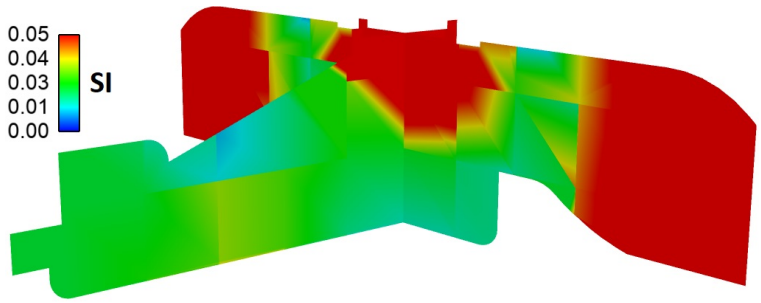

(b) SOI=35 (CAD bTDC)

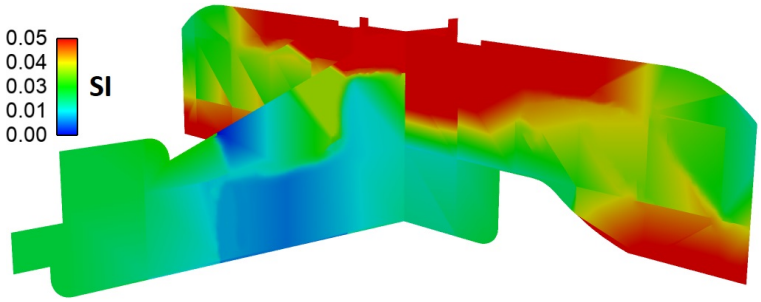

(c) SOI=55 (CAD bTDC)

Figure 5.14: Stratification distribution at PR=20, FQ=4 mg/cycle, and (a) SOI=15 CAD bTDC, (b) SOI=35 CAD bTDC, (c) SOI=55 CAD bTDC

mixture. Fig. 5.14(a) shows local stratification index distribution for SOI=15 CAD bTDC case. Higher values of SI are due to short available mixing time for the injected fuel which results in accumulation of fuel at some regions and inadequate fuel in another regions. These high and low fuel regions deviate from homogeneously mixed mixture and demonstrated by high SI values in Fig. 5.14(a). Advancing injection

timing provides more mixing time for the fuel and combustion chamber mixture. This yields to a homogeneously mixed condition. Fig. 5.14(b) shows the SI distribution for SOI=35 CAD bTDC condition which has lower stratification values compared to SOI=15 CAD bTDC. A similar trend can be observed for the very advanced SOI=55 CAD bTDC which is shown at Fig. 5.14(c). Effect of premixed ratio on fuel

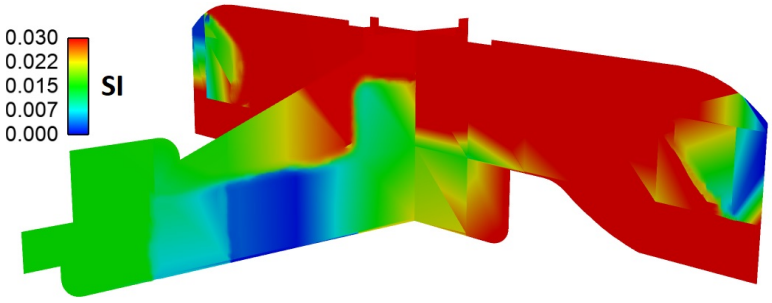

(a) PR =00

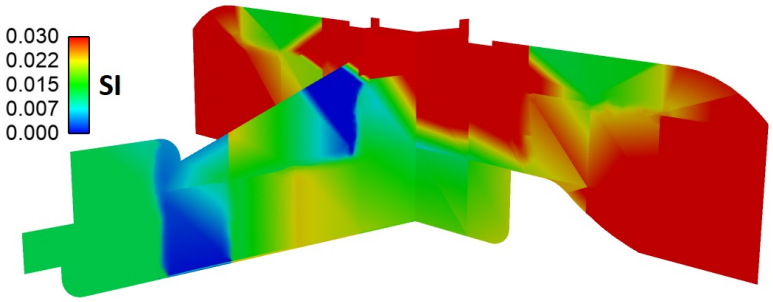

(b) PR =20

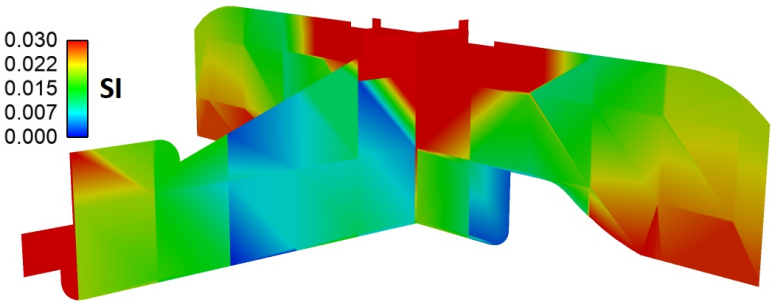

(c) PR =40

Figure 5.15: Stratification distribution at SOI=45 CAD bTDC, FQ=4 mg/cycle, and (a) PR=0, (b) PR=30, (c) PR=50

stratification is also studied in this work and presented at Fig. 5.15. Increasing PR increases the amount of premixed fuel and consequently leads to higher percentage of fuel received long mixing time of premixed injection. Therefore, it is expected that higher PR values result in lower SI values which represent close to homogeneous mixtures. This trend can be confirm based on results shown in Fig. 5.15. Using PR=0 at RCCI engine means not using the premixed injection and all fuel quantity is injected via direct injection. This reduces available mixing time and causes a substantial deviation from the homogeneous condition which is shown by high SI values at Fig. 5.11(a). Increasing PR value decreases DI injected fuel and results in better mixing of fuel air and consequently leads to lower SI values which are visible at Fig. **??** and Fig. **??** for PR=20 and PR=40, respectively.

These results demonstrated the effects of fuel quantity, DI injection timing, and premixed ratio on reactivity and stratification distributions and levels separately. In this study combined effect of the control actions on reactivity and stratification are also investigated. This was accomplished through running of the transient open cycle CFD model of the RCCI engine though a test plan where FQ, SOI, and PR are varied. Fig. 5.16 demonstrates the variations of FQ, SOI, and PR as the inputs for the CFD model for 300 transient engine cycles. The CFD results for chemical composition and thermal distribution at 10 CAD bTDC were processed for each cycle and RRI and SI values for the test plan are presented at Fig. 5.16. These results demonstrate an inverse relation between RRI and SI parameters. Increased SI leads to lower RRI

values and lower SI values correlate with higher RRI levels. Lower SI values are associated with close to homogeneous mixture conditions. As the mixture reaches a homogeneous condition, fuel is well distributed inside the combustion chamber. This reduces the likelihood of too lean or too rich mixture formation which results in low reactivity levels. Therefore, low stratified mixtures provide higher reactivity levels and have more tendency for auto-ignition.

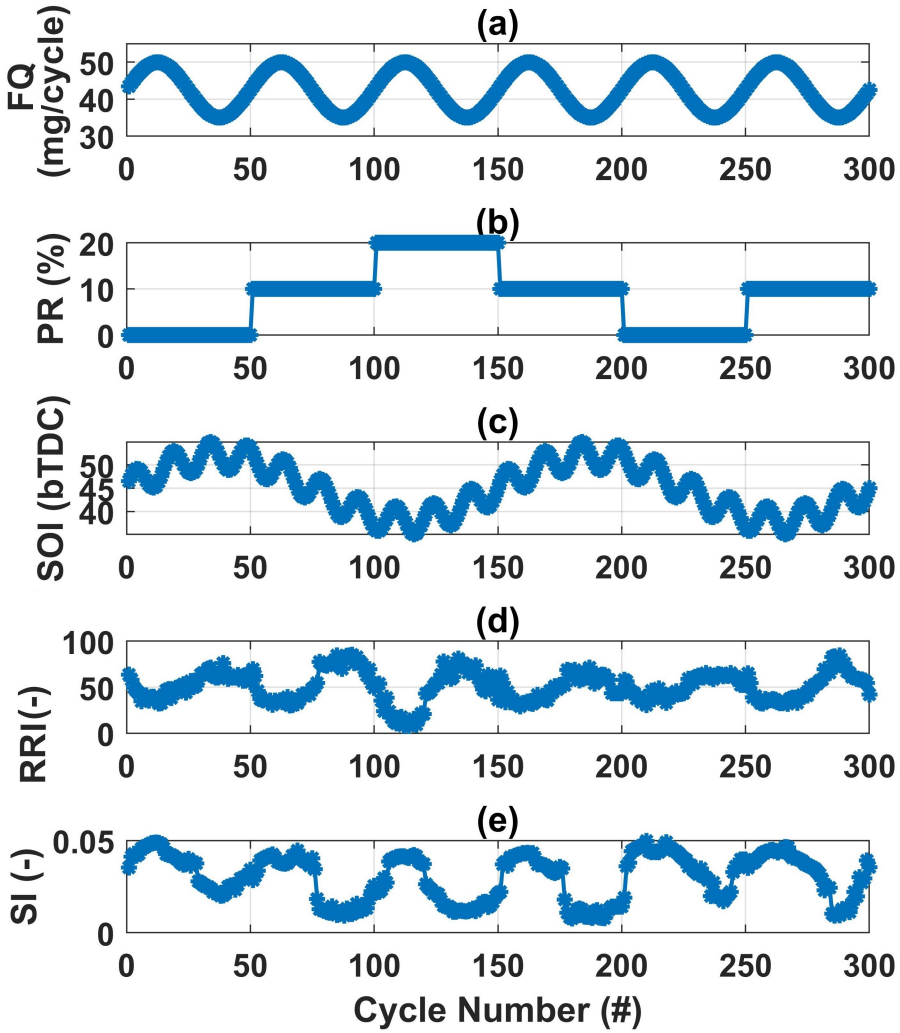

Figure 5.16: Relative reactivity index (RRI) and stratrification index (SI) variations for transient test plan at $T_{in} = 333$ K, $N = 1200$ RPM, $P_{in} = 96.5$ kPa

Estimation of reactivity and stratification levels requires computationally expensive CFD simulations and post-processing. In this study, a data-driven approach based on Kernelized Canonical Correlation Analysis (KCCA) identification approach is presented to estimate RRI and SI values associated with engine input parameters.

5.5 Data driven model of Reactivity and Stratification

The data-driven state space modeling of reactivity and stratification is demonstrated in this section. Without prior physics understanding, data-driven modeling techniques can generate stratification and reactivity estimates. Compared to physics-based approaches, this can greatly speed up the modeling process. This is because the development of high-fidelity physics-based models for complex systems requires tedious calibration. As a result, this section adapts a data-driven strategy based on KCCA to create a data-driven identification of reactivity and stratification dynamics based on the KCCA method for the RCCI engine. Fig. 5.17 represents the structure of the data-driven KCCA identification strategy adopted in this study. This strategy is conducted in four steps which are state estimation, dynamic identification, output estimation, and model evaluation. Initially, the inputs and outputs of the plan are divided into training and test sections. The training section is used to estimate

the dynamic and the test section is used to evaluate the accuracy of the model. All inputs and outputs are provided to the state estimation stage and estimated unknown states are computed. Estimated unknown states are also divided into training and test sections. The Linear parameter varying (LPV)strategy then used the training estimated unknown states and train inputs and training outputs to identify the dynamic plan model at the dynamic identification step. The identified state-space dynamic model was provided the test inputs and test estimated states to predict test outputs at the output estimation step. Finally predicted test outputs are compared to actual test outputs to evaluate model accuracy at the last step.

The input-output based KCCA approach is explained here by forming state-space dynamic equations. These equations can be presented as shown in Eq. (5.7).

$$X_{k+1} = A(p_k)X_k + B(p_k)U_k + K(p_k)E_k, \tag{5.7a}$$

$$Y_k = C(p_k)X_k + E_k, \tag{5.7b}$$

Where the inputs and outputs, respectively, are denoted by the variables U_k and Y_k, and at discrete-time instant k, X_k stands for unidentified states. $A(p_k)$, $B(p_k)$, $K(p_k)$, and $C(p_k)$ matrices denote LPV state-space matrices that are governed by scheduling variables, p_k; E_k represents additive Gaussian white noise, respectively. Eq. (5.7) can

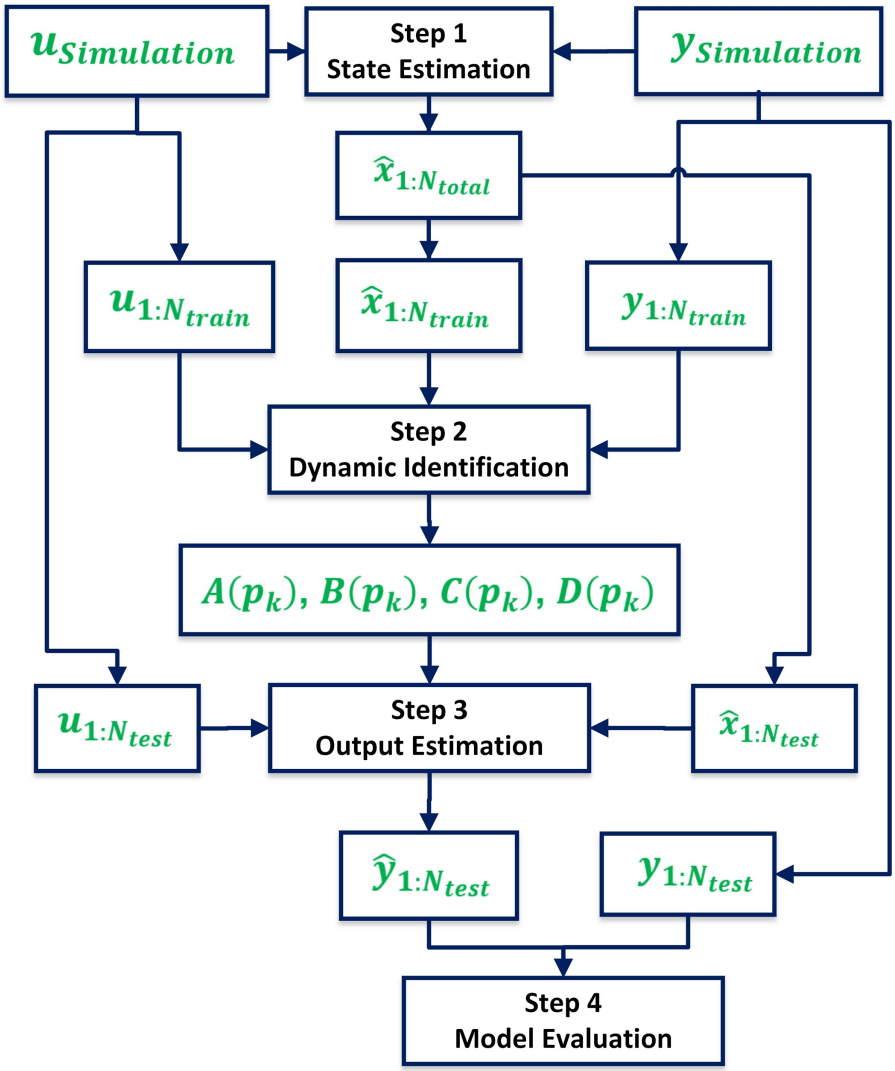

Figure 5.17: Input-Output based Kernelized Canonical Correlation Analysis (KCCA) modeling flow chart

be rewritten as $E_k = Y_k - C(p_k)X_k$ to form the state-space model as follows:

$$X_{k+1} = \widetilde{A}(p_k)X_k + \widetilde{B}(p_k)U_k + K(p_k)E_k, \tag{5.8a}$$

$$Y_k = C(p_k)X_k + E_k, \tag{5.8b}$$

where $\widetilde{A}(p_k) = B(p_k) - K(p_k)D(p_k)$ and $\widetilde{B}(p_k) = A(p_k) - K(p_k)C(p_k)$. These state-space matrices are established using the feature maps and support vector weighting matrices shown in Eq. (5.9). As seen below, the feature maps and weighting matrices can be used to create state-space matrices [82].

$$\tilde{A}_e(\cdot) = W_1\Phi_1(\cdot) = \sum_{k=1}^{N} \alpha_k x_k^T \bar{k}^1(p_k, \cdot), \tag{5.9a}$$

$$B_e(\cdot) = W_2\Phi_2(\cdot) = \sum_{k=1}^{N} \alpha_k u_k^T \bar{k}^2(p_k, \cdot), \tag{5.9b}$$

$$K_e(\cdot) = W_3\Phi_3(\cdot) = \sum_{k=1}^{N} \alpha_k y_k^T \bar{k}^3(p_k, \cdot), \tag{5.9c}$$

$$C_e(\cdot) = W_4\Phi_4(\cdot) = \sum_{k=1}^{N} \beta_k x_k^T \bar{k}^3(p_k, \cdot), \tag{5.9d}$$

Where α and β are Lagrangian multipliers of the least square support vector machine (LS-SVM) optimization problem, and $\bar{k}^i(p_j, p_k)$ is Gaussian kernel function defined as

$$\bar{k}^i(p_j, p_k) = \exp\big(-\frac{||p_j - p_k||_2^2}{2\sigma_i^2}\big), \tag{5.10}$$

Where, σ_i denotes the standard deviation and $||.||_2$ is the l_2 norm. Using on this KCCA approach, a state space formation for the relative reacitvity index and stratification index are determined as presented in Equations (5.11) and (5.12). Fuel quantity is selected as the scheduling parameter since reacivity and stratification levels is mainly determined by mixture equivalence ratio which is adjusted by injected fuel quantity.

$$\begin{bmatrix} X_1 \\ X_2 \\ X_3 \\ X_4 \\ X_5 \end{bmatrix}_{k+1} = A(FQ) \begin{bmatrix} X_1 \\ X_2 \\ X_3 \\ X_4 \\ X_5 \end{bmatrix}_{k} + B(FQ) \begin{bmatrix} SOI \\ FQ \\ PR \end{bmatrix}_{k} \tag{5.11}$$

$$\begin{bmatrix} RRI \\ SI \end{bmatrix}_{k+1} = C(FQ) \begin{bmatrix} X_1 X_2 X_3 X_4 X_5 \end{bmatrix}^{T}_{k+1} \tag{5.12}$$

In order to determine how the fuel quantity (FQ), direct injection timing (SOI), and premixed ratio (PR) affected the relative reactivity index and stratification index, these variables were examined using the CFD model for the RCCI engine. A test plan was established, and the transient CFD model was executed. The change of FQ, SOI, and PR over the course of the simulation test plan for the 300 cycles is shown in Fig. 5.16. The relative reactivity index and stratification for every cycle were determined by sampling and post-processing CFD outcomes at 10 CAD bTDC at each cycle. This crank angle is selected to provide enough mixing period for the DI fuel and avoid combustion initiation which can release energy and effect reacivity levels. The data-driven model was developed and evaluated utilizing this set of data. The training process of the data-driven model's estimation for the RRI and SI was done using 75% of the data, while the rest 25% was employed to evaluate the model's performance. The accuracy of the data-driven model for predicting RRI and SI is

shown in Fig. 5.18. RRI and SI were predicted using the data-driven model with root mean square errors of 5.5 and 0.003, respectively. This demonstrates the capability of the data-driven models to predict stratification and reactivity levels for a variety of input conditions without the need to run computationally intensive CFD models.

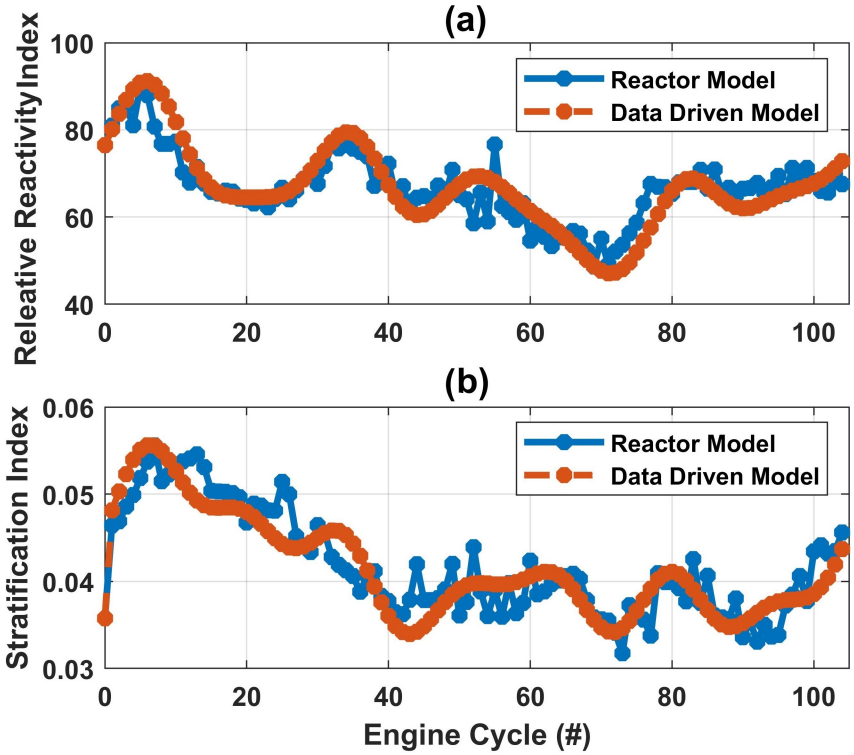

Figure 5.18: Data-driven estimation of RCCI fuel reactivity and stratification at $T_{in} = 333$ K, $P_{in} = 96.5$ kPa

The estimated reactivity and fuel stratification levels can be used as combustion states to develop a state space dynamic model for RCCI combustion which can be used to estimate desired RCCI engine output parameters such as combustion timing and maximum pressure rise rate (MPRR). Fig. 5.19 presents the variation start of RRI, SI, start of combustion (SOC), crank angle of 50% fuel burnt (CA50), burn duration (BD), and MPRR for the engine inputs previously shown at Fig. 5.16. These results

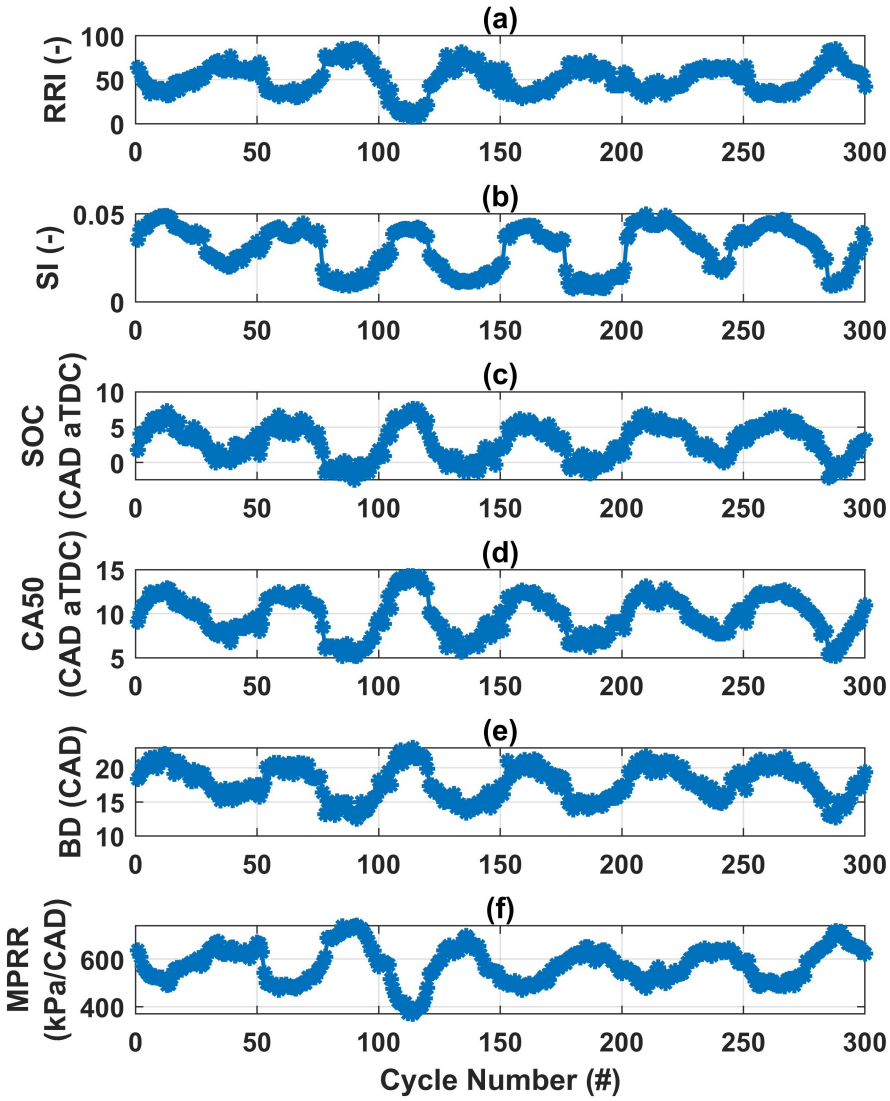

Figure 5.19: Variation of start of combustion, CA50, burn duration, and MPRR based on reactivity and stratification variations for test conditions in Fig. 5.16, and $T_{in} = 333$ K, $N = 1200$ RPM, $P_{in} = 96.5$ kPa

demonstrate that SOC, CA50, BD, and MPRR variation correlates with RRI and SI variations. These correlations can be identified through scatter plots presented in Fig. 5.20 and Fig. 5.21.

Variations of SOC, burn duration, CA50, and MPRR based on relative reactivity

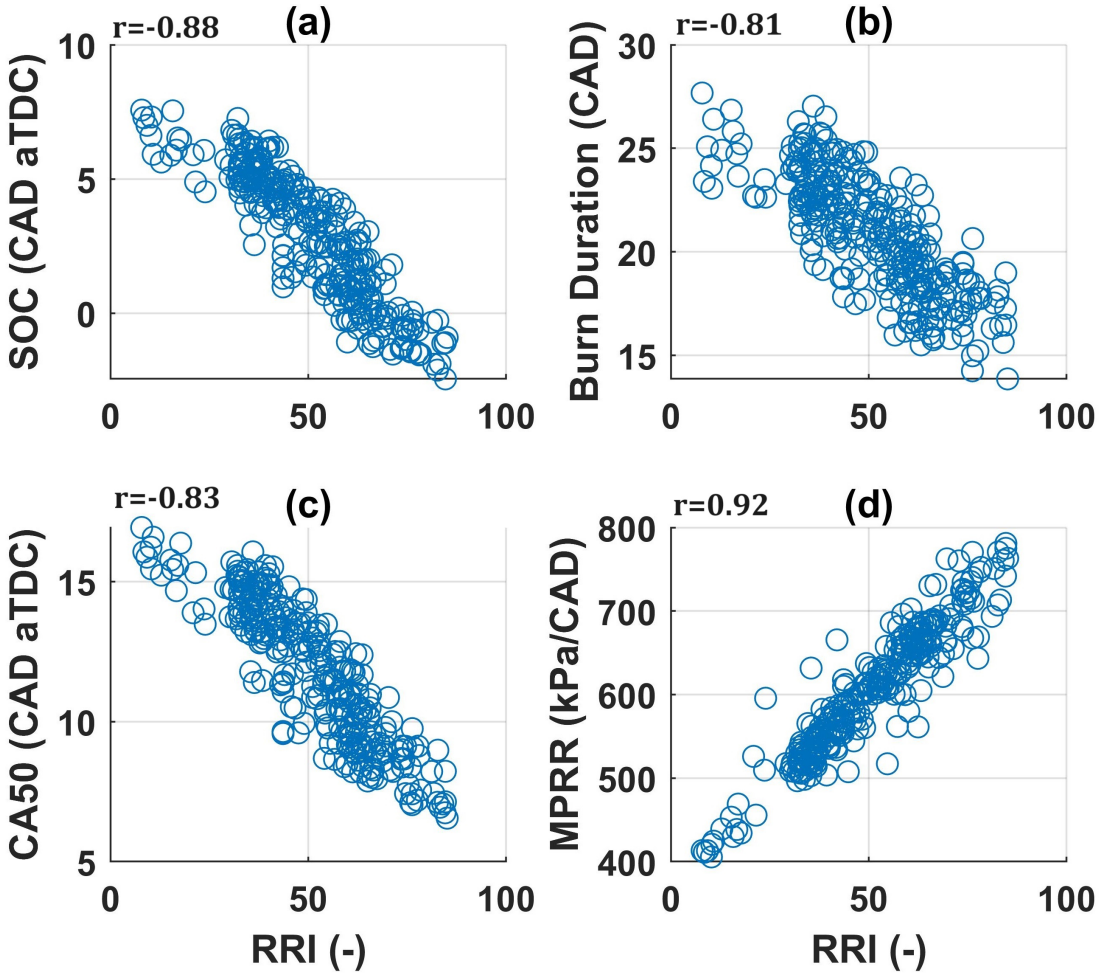

Figure 5.20: Effect of reactivity levels on (a) start of combustion, (b) burn duration, (c) CA50 , and (d) MPRR for for test conditions in Fig. 5.16, and $T_{in} = 333$ K, $N = 1200$ RPM, $P_{in} = 96.5$ kPa

index variation are shown in Fig. 5.20. SOC shows an inverse relation with the RRI. Increasing RRI means a higher percentage of fuel forms a reactive mixture with the air. This increases the chance of the existence of very high reactive pockets which will cause imminent combustion. Therefore, mixtures with higher RRI have earlier SOC timings.

On the other hand, mixtures with higher RRI values have shorter burn durations.

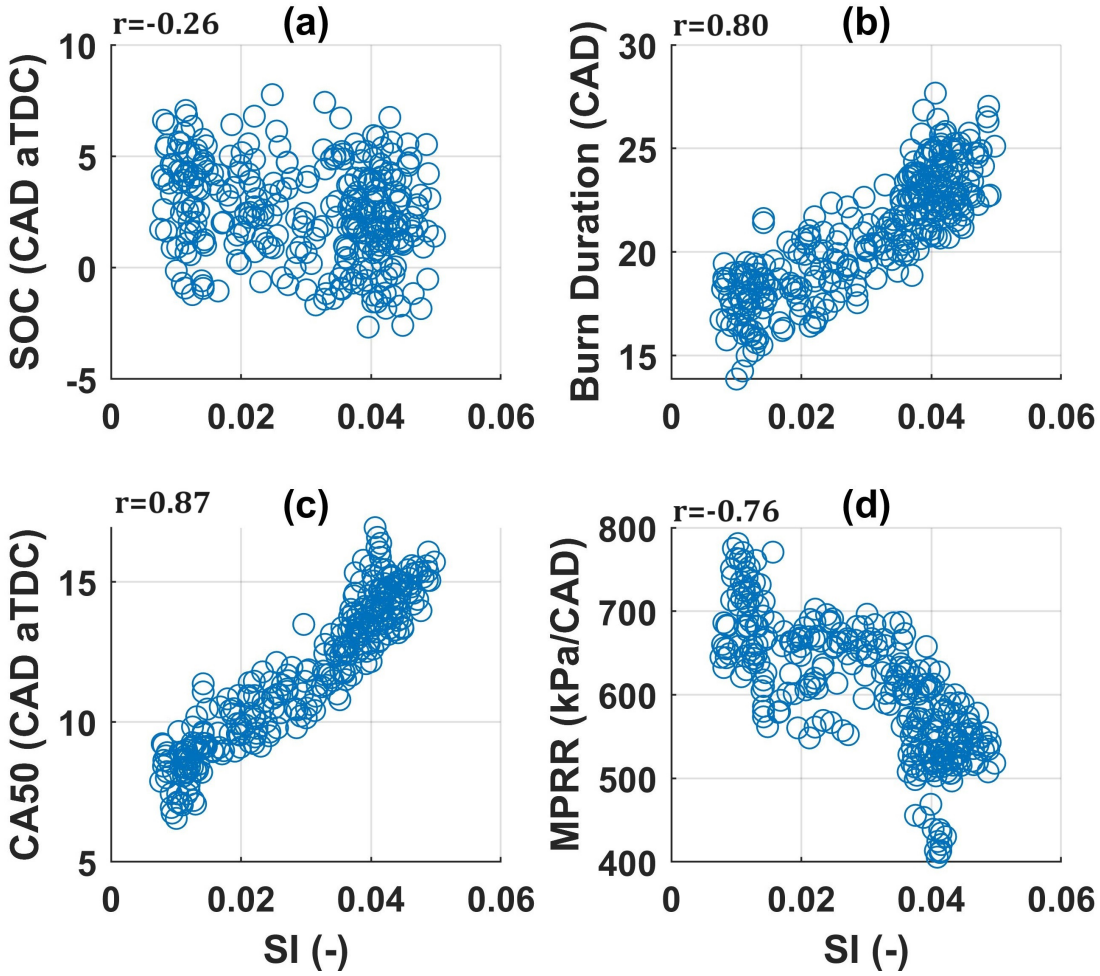

Figure 5.21: Effect of stratification levels on (a)start of combustion, (b) burn duration, (c) CA50 , and (d) MPRR for test conditions in Fig. 5.16 and $T_{in} = 333$ K, $N = 1200$ RPM, $P_{in} = 96.5$ kPa

This happens due to high chance of forming auto-ignition pockets at higher RRI values which initiate combustion at multiple locations within the combustion chamber and reduces flame propagation distances. The inverse correlations of SOC and BD with RRI cause the CA50 advance as RRI increases. As the combustion starts earlier and completes within a shorter duration, the CA50 timing also reduces at mixtures with higher RRI values. Fig. 5.20(d) presents a direct correlation between MPRR and RRI. Higher values for RRI represent a higher percentage of fuel within the

combustion chamber that is reactive and ready to combust. This results in a higher chance for the release of a significant portion of injected fuel energy simultaneously which causes higher pressure rise rate values and consequently higher MPRR values.

Variation trends between SOC, BD, CA50, and MPRR with SI are presented by scatter plots in Fig. 5.21. Based on the results in Fig. 5.21(a), SOC does not have a meaningful correlation with SI. However, BD shows a direct relation with the SI. This can be explained as reduced SI values are associated with relatively homogeneous mixtures. In these mixtures, combustion starts at multiple auto-ignited points which reduces regions that require flame prorogation to be ignited. This simultaneous start of combustion at multiple points causes the fuel-air mixture to convert faster to combustion products and consequently reduces the burn duration. Fig. 5.21(c) shows the trend between CA50 and SI for the test plan data. Increased SI values cause the CA50 timing to be retarded. This happens due to longer BD which delays completion of combustion and consequently increases the CA50 timing. Fig. 5.21(d) demonstrates the relation between MPRR and SI. It can be understood that MPRR has a moderate inverse relation with SI. Decreased SI values are observed at highly homogenous mixtures which have a higher chance of multiple simultaneous auto-ignition formation and consequently having multiple combustion centers which cause rapid heat release rate and consequently higher MPRR values.

Trends between SOC, BD, CA50, and MPRR with RRI and SI which are obtained

from Fig. 5.20 and Fig. 5.21 can be connected to the effect of FQ, SOI and PR on RRI and SI which were obtained from Figures 5.9 to 5.15 to form a control strategy to adjust FQ, SOI and PR as the control actions to control RCCI combustion metrics (e.g. CA50 or MPRR) at the desired values.

5.6 Summary and conclusion

computational fluid dynamic (CFD) models can provide usefull information for the engine combustion control but this information is rately used for engine control since CFD models are computaionally expensive for use in real-time cycle-by-cycle engine control. This paper studied the use of CFD models for a 2-liter reactivity controlled compression ignition (RCCI) engine to drive key combustion and air-fuel mixture preparation parameters, including relative reactivity index (RRI) and mixture stratification index (SI) for engine combustion control. The resualts from this paper led creating a control-oriented data driven RCCI model that links engine control inputs (e.g. fuel quantity, premixed fuel ratio, and fuel injection timing) for the estimation of RCCI and SI for engine combustion control. Here are the steps followed in this work:

First, an open-cycle CFD model for the RCCI engine was created, and it was verified using steady-state and transient experimental data. A reactivity model was

then created across a variety of engine-relevant circumstances and verified using experimental shock tube data. The stratification of fuel inside the combustion chamber was then evaluated using a stratification metric that was established. The impact of engine inputs on stratification and reactivity levels during transient operation was determined using these models. With the help of this data set, a state space data-driven model (DDM) based on the Kernel Canonical Correlation Analysis (KCCA) technique was trained. Here are the major findings from this study:

❶ The resulting DDM can predict RRI and SI with root mean square errors of 5.5 and 0.003, respectively. The DDM is computationally efficiency and can predict RRI and SI for each engine cycle in less than 2 msec on a core i5@3.3 GHz computer.

❷ Mixture reactivity levels and stratification levels show an inverse relation. Higher reactivity indexes were observed at lower stratified mixtures and vice versa.

❸ Fuel-air mixtures with high SI have advanced combustion phasing (CA50) and high maximum pressure rise rate (MPRR) values. Therefore limiting MPRR or retarding CA50 can be achieved by targeting engine inputs which associates with lower SI values.

❹ High reactive mixtures with higher RRI values show advance combustion timings, lower burn duration, and higher MPRR. This can be used to set the

control strategy for combustion timing and MPRR.

❹ Dual fuel ignition delay has two distinctive data clusters defined. The first cluster was observed at lower temperatures and higher high reactive fuel content and the second cluster was observed at higher temperatures and lower high reactive fuel concentration.

Utilizing the developed reactivity and stratification control models from this work, the future work may include the design of RCCI combustion control on a real engine setup. In addition, the same methodology from this work for using CFD models for engine combustion can be studied for other types of internal combustion engines.

Chapter 6

Summary and Conclusion

Low-temperature combustion strategies are proposed as a potential combustion strategy to meet the strict emission regulations on internal combustion engines. These strategies run the combustion at lower temperatures compared to conventional combustion processes and generate lower toxic emissions such as nitrogen oxides. Reactivity controlled compression ignition engines are one of these LTC strategies developed to operate with a blend of two fuels with different reactivity levels. The combustion process at RCCI engines is very difficult to model based on governing fluid dynamics and kinetics models. This leads to significant challenges in controlling RCCI combustion and running these engines at their optimal conditions. This research is performed to address these challenges and propose a fast and reliable approach for modeling highly nonlinear RCCI combustion and control.

6.1 Summary of research

This study was conducted in several areas which were joined to achieve research objectives. It was initialized by developing an open-cycle computational fluid dynamic model for an RCCI engine. The piston was 3D scanned and combustion chamber geometry was created for the CFD model. The model was further developed by adding dual fuel injector models, valve lift profiles, chemical reaction mechanisms, and fluid dynamic models. The CFD model was later validated against eight steady-state operational points and five transient cycles data obtained from the actual RCCI engine. This model was used to obtain thermal and chemical distribution inside the combustion chamber which are required for studying reactivity formation and stratification inside the combustion chamber. This section of research was continued by the development of a dual fuel reactivity model at engine-relevant conditions. Fuel air mixture reactivity was defined as an inverse function of mixture ignition delay. This function is tuned based on the reactivity and ignition delays of two primary reference fuels. Moreover, the ignition delay is considered a nonlinear function of temperature, pressure, and mixture composition. A validated homogenous closed reactor model was developed at CONVERGE CFD and was used to obtain ignition delay data. The reactor model was coupled with MATLAB and ran for 20,000 cases with temperature, pressure, and fuel-air composition found inside the combustion chamber close TDC timing and ignition delay values were obtained for these cases.

A multiple linear regression method was implemented on ignition delay data and the nonlinear ignition delay function was obtained. This function was coupled with the reactivity function and the mixture reactivity model was obtained based on thermal and chemical properties of the mixture. This reactivity model was then implemented on CFD model results to obtain reactivity values and distribution inside the combustion chamber. Fuel stratification is the other parameter studied in this section. Homogenously mixed dual fuel-air mixture was considered as the zero stratified mixture. Local dual fuel mass fraction difference with homogenous dual fuel mass fraction was defined as the local stratification value. The stratification level for the entire combustion chamber was defined as the average of the local stratification values. This section of research studied the effect of engine operational inputs such as fuel quantity, premixed ratio, and direct injection timing on reactivity and stratification levels inside the combustion chamber. A transient operational test plan was developed and the CFD model was run for 300 consecutive cycles. Temperature, pressure, and chemical composition distribution inside the combustion chamber were obtained for every cycle and were used to compute the reactivity and stratification levels inside the combustion chamber. Two data-driven methods based on a linear parameter varying approach were implemented to build two data-driven models between engine inputs and reactivity and stratification levels. The findings showed that the proposed data-driven method has good predictive performance at estimating reactivity and stratification levels. The predicted reactivity and stratification can be

used to predict engine outputs such as combustion timing and maximum pressure rise rate. The study found that high stratification values cause higher MPRR and advanced CA50 timing. Moreover, High reactive values correlate with lower burn duration, advanced combustion timings, and higher MPRR values.

In another section of this research, a control-oriented model based on linear parameter varying identification of RCCI combustion dynamics was developed and a predictive controller was created based on the identified model. This section was conducted to propose a fast and reliable method to control RCCI combustion. This process was initialized by obtaining experimental data from the RCCI engine. A test plan was developed for varying engine inputs and the RCCI engine was operated in transient operation and combustion timing data was recorded. Experimental measurements of the RCCI engine inputs (i.e., SOI, PR, FQ) and the desired output (i.e., CA50) were used to develop the data-driven state space model. This model used FQ (engine load) as the scheduling variable and determined CA50 as a function of three control inputs. The developed data-driven model was employed to estimate CA50 by using measured engine inputs from another experimental data set and validated based on comparing estimated CA50 results with measured CA50 values. Validation results showed that the estimated state space LPV model could predict combustion phasing (CA50) with an average error less than 1 CAD. The generated control-oriented model was then incorporated into an MPC framework to control CA50 by modifying the start of injection (SOI) of *n*-heptane as the DI fuel. Experimental results for the controller

demonstrated that the LPV-based MPC controller was able to track the desired CA50 with a maximum of 0.8 CAD average error for varying engine conditions. These experimental results demonstrated that data-driven MPC combustion controllers can provide similar results compared to physics-based MPC combustion controllers while requiring less development time.

The LPV identification method which was used to develop a data-driven model for reactivity, stratification, and combustion timing requires plant states to be measurable and known plant outputs. This research also proposed the Kernelized Canonical Correlation Analysis approach for RCCI state-space dynamic identification which can develop a state-space model with unknown states. Experimental measurements were obtained from a 2-liter 4-cylinder RCCI engine by changing the start of injection timing for n-heptane, premixed ratio, and fuel quantity as the control inputs to the engine and measuring CA50 and IMEP as the outputs from the engine. These data are then used to estimate unknown states and create a data-driven LPV model to determine CA50 and IMEP as a function of three control inputs. The LPV model was later connected into a constrained MPC framework to track reference CA50 and IMEP. The developed controller results showed that the KCCA-LPV-based constrained MPC controller followed the referenced CA50 and IMEP with less than 1.4 CAD and 37 kPa average tracking errors, respectively. Future work includes the implementation of the designed controller on the RCCI engine experimental platform.

One of the other achievements of this research is the development and validation of two control-oriented MPRR models for an RCCI engine at APS labs. The first MPRR model is developed based on a physics-based method while the second model is obtained through a data-driven modeling approach. The physics-based MPRR model simulated the in-cylinder pressure rise rate through the first law implementation and calibrated the model by calibrating a Wiebe function which represents the fuel heat release rate. Test results showed that the physics-based MPRR model can estimate experimental MPRR with a mean estimation error equal to 87 kPa/CAD. The second MPRR model was developed through a data-driven KCCA-LPV identification approach. In this method, unknown states are estimated by the KCCA method and state-space representations of the RCCI combustion dynamics are computed by the LPV method. The developed data-driven MPRR model could estimate the experimental MPRR values with an average error equal to 47 kPa/CAD. This study demonstrated that stochastic MPRR phenomena at RCCI engines can be modeled through physics-based modeling and machine-learning approaches. Modeling efforts and estimation accuracies showed that the machine learning algorithm can develop a data-driven MPRR model with less modeling effort and can provide higher estimation accuracies compared to physics-based modeling. This superior performance of the data-driven model is due to the implementation of highly non-linear support vector functions to learn the stochastic behavior of the MPRR at RCCI engines.

Main findings from this study is summarized below:

- Data-driven modeling and predictive control of combustion phasing for RCCI engines
  - ✳ The experimental results of the data-driven model predictive controller demonstrated that a data-driven MPC combustion controller can provide similar results compared to a physics-based MPC combustion controller while requiring less development

- Input-output Data-driven Modeling and MIMO Predictive Control of an RCCI Engine Combustion.
  - ✳ State-space dynamic identification of plants depends on state selections which is challenging in complex systems. In this situation, using the unknown state identification approach based on the KCCA algorithm provides better estimation results compared to using plant outputs as the states.

- Control-Oriented Data-Driven and Physics-Based Modeling of Maximum Pressure Rise Rate in Reactivity Controlled Compression Ignition Engines.
  - ✳ Stochastic MPRR phenomena at RCCI engines can be modeled through physics-based modeling and machine learning approaches. Modeling efforts and estimation accuracies showed that the machine learning algorithm can develop a data-driven MPRR model with less modeling effort and

can provide higher estimation accuracies compared to physics-based modeling. This superior performance of the data-driven model is due to the implementation of highly non-linear support vector functions to learn the stochastic behavior of the MPRR at RCCI engines.

■ Data-driven Identification of Reactivity and Stratification Dynamics at RCCI Engines Based on Kernel Canonical Correlation Analysis

  ✳ Dual-fuel reactivity is a nonlinear function of thermal properties and mixture composition. A higher reactive mixture is a result of the optimum ratio between high reactive fuel, low reactive fuel, and oxygen content.

  ✳ High-stratified mixtures have advanced CA50 and higher MPRR values.

  ✳ High reactive mixtures show advance combustion timings, lower burn duration, and higher MPRR values.

6.2 Proposals for future works

This research proposed and implemented data-driven methodology to control RCCI combustion. This approach proved to develop a fast control-oriented model with short development time. This study can be further continued at the following areas

† Development of online data-driven combustion controller by automating the

identification and controller implementation.

† Development of multi-dimensional data-driven models for higher identification accuracy

† Development of predictive reacivity and stratification controller using the developed reactivity and stratification dynamics model.

References

[1] C. B. Ribeiro, F. H. C. Rodella, and L. Hoinaski, "Regulating light-duty vehicle emissions: an overview of US, EU, China and Brazil programs and its effect on air quality," *Clean Technologies and Environmental Policy*, pp. 1–12, 2022.

[2] H. Ciezki and G. Adomeit, "Shock-tube investigation of self-ignition of n-heptane-air mixtures under engine relevant conditions," *Combustion and flame*, vol. 93, no. 4, pp. 421–433, 1993.

[3] R. D. Reitz and S. L. Kokjohn, "Comparison of conventional diesel and reactivity controlled compression ignition (RCCI) combustion in a light-duty engine," *Presentation at 2012 Directions in Engine-Efficiency and Emissions Research (DEER) Conference*, 2012.

[4] E. Ansari, K. Poorghasemi, B. K. Irdmousa, M. Shahbakhti, and J. Naber, "Efficiency and emissions mapping of a light duty diesel-natural gas engine operating in conventional diesel and RCCI modes," 2016.

[5] A. B. Dempsey, N. R. Walker, and R. Reitz, "Effect of piston bowl geometry on dual fuel reactivity controlled compression ignition (RCCI) in a light-duty engine operated with gasoline/diesel and methanol/diesel," *SAE International Journal of Engines*, vol. 6, no. 1, pp. 78–100, 2013.

[6] S. L. Kokjohn, M. P. Musculus, and R. D. Reitz, "Evaluating temperature and fuel stratification for heat-release rate control in a reactivity-controlled compression-ignition engine using optical diagnostics and chemical kinetics modeling," *Combustion and Flame*, vol. 162, no. 6, pp. 2729–2742, 2015.

[7] R. D. Reitz and G. Duraisamy, "Review of high efficiency and clean reactivity controlled compression ignition (RCCI) combustion in internal combustion engines," *Progress in Energy and Combustion Science*, vol. 46, pp. 12–71, 2015.

[8] Y. Rui-Qiang, T. Xin, and Y. Xiang-Long, "CO2 emission of urban passenger transportation in china from 2000 to 2014," *Advances in Climate Change Research*, vol. 10, no. 1, pp. 59–67, 2019.

[9] F. M. Orr, "2015 quadrennial technology review," in *Proceedings of the International Conference for High Performance Computing, Networking, Storage and Analysis*, 2015.

[10] U. EIA, "Monthly energy review-energy information administration," *Total Energy*, 2023.

[11] J. A. Bittle, B. M. Knight, and T. J. Jacobs, "Heat release parameters to assess low temperature combustion attainment," tech. rep., SAE Technical Paper, 2011. Paper No. 2011-01-1350.

[12] G. D. Neely, S. Sasaki, Y. Huang, J. A. Leet, and D. W. Stewart, "New diesel emission control strategy to meet us tier 2 emissions regulations," *SAE transactions*, pp. 512–524, 2005.

[13] J. A. Caton, "Thermodynamic advantages of low temperature combustion (LTC) engines using low heat rejection (LHR) concepts," 2011. Paper No. 01-0312.

[14] S. L. Kokjohn, R. M. Hanson, D. A. Splitter, and R. D. Reitz, "Experiments and modeling of dual-fuel HCCI and PCCI combustion using in-cylinder fuel blending," *SAE International Journal of Engines*, vol. 2, no. 2, pp. 24–39, 2010.

[15] S. Curran, Z. Gao, and R. Wagner, "Reactivity controlled compression ignition drive cycle emissions and fuel economy estimations using vehicle systems simulations with e30 and ulsd," *SAE International Journal of Engines*, vol. 7, no. 2, pp. 902–912, 2014.

[16] C. Daw, M. Kennel, C. Finney, and F. Connolly, "Observing and modeling nonlinear dynamics in an internal combustion engine," *Physical Review E*, vol. 57, no. 3, p. 2811, 1998.

[17] Y. Shi, H.-W. Ge, and R. D. Reitz, *Computational optimization of internal combustion engines*. Springer Science & Business Media, 2011.

[18] D. Splitter, R. Hanson, S. Kokjohn, and R. Reitz, "Improving engine performance by optimizing fuel reactivity with a dual fuel PCCI strategy," *Journal of Automobile Engineering*, vol. 8, p. 9, 2010.

[19] S. L. Kokjohn, *Reactivity controlled compression ignition (RCCI) combustion*. PhD thesis, The University of Wisconsin-Madison, 2012.

[20] S. L. Kokjohn and R. D. Reitz, "Reactivity controlled compression ignition and conventional diesel combustion: a comparison of methods to meet light-duty nox and fuel economy targets," *International Journal of Engine Research*, vol. 14, no. 5, pp. 452–468, 2013.

[21] R. Hanson, S. Curran, R. Wagner, S. Kokjohn, D. Splitter, and R. Reitz, "Piston bowl optimization for RCCI combustion in a light-duty multi-cylinder engine," *SAE International Journal of Engines*, vol. 5, no. 2, pp. 286–299, 2012.

[22] P. Zoldak, A. Sobiesiak, M. Bergin, and D. D. Wickman, "Computational study of reactivity controlled compression ignition (RCCI) combustion in a heavy-duty diesel engine using natural gas," 2014. SAE Technical Paper.

[23] M. Nazemi and M. Shahbakhti, "Modeling and analysis of fuel injection parameters for combustion and performance of an RCCI engine," *Applied Energy*, vol. 165, pp. 135–150, 2016.

[24] M. M. Salahi, V. Esfahanian, A. Gharehghani, and M. Mirsalim, "Investigating the reactivity controlled compression ignition (RCCI) combustion strategy in a natural gas/diesel fueled engine with a pre-chamber," *Energy Conversion and Management*, vol. 132, pp. 40–53, 2017.

[25] Y. Li, M. Jia, Y. Chang, M. Xie, and R. D. Reitz, "Towards a comprehensive understanding of the influence of fuel properties on the combustion characteristics of a RCCI (reactivity controlled compression ignition) engine," *Energy*, vol. 99, pp. 69–82, 2016.

[26] Y. Li, M. Jia, Y. Chang, S. L. Kokjohn, and R. D. Reitz, "Thermodynamic energy and exergy analysis of three different engine combustion regimes," *Applied Energy*, vol. 180, pp. 849–858, 2016.

[27] K. Poorghasemi, R. K. Saray, E. Ansari, B. K. Irdmousa, M. Shahbakhti, and J. D. Naber, "Effect of diesel injection strategies on natural gas/diesel RCCI combustion characteristics in a light duty diesel engine," *Applied energy*, vol. 199, pp. 430–446, 2017.

[28] J. U. Eichmeier, R. Reitz, and C. Rutland, "A zero-dimensional phenomenological model for RCCI combustion using reaction kinetics," *SAE International Journal of Engines*, vol. 7, no. 1, pp. 106–119, 2014.

[29] M. Ates, R. D. Matthews, and M. J. Hall, "A full-cycle multi-zone quasi-dimensional direct injection diesel engine model based on a conceptual model developed from imaging experiments," 2017. Paper No. 2017-01-0537.

[30] E. Doosje, F. Willems, and R. Baert, "Experimental demonstration of RCCI in heavy-duty engines using diesel and natural gas," tech. rep., SAE Technical Paper, 2014. Paper No. 2014-01-1318.

[31] Z. Jia and I. Denbratt, "Experimental investigation of natural gas-diesel dual-fuel RCCI in a heavy-duty engine," *SAE International Journal of Engines*, vol. 8, no. 2, pp. 797–807, 2015.

[32] M. Dahodwala, S. Joshi, E. W. Koehler, and M. Franke, "Investigation of diesel and cng combustion in a dual fuel regime and as an enabler to achieve RCCI combustion," tech. rep., SAE Technical Paper, 2014. Paper No. 2014-01-1308.

[33] M. Dahodwala, S. Joshi, E. Koehler, M. Franke, and D. Tomazic, "Experimental and computational analysis of diesel-natural gas rcci combustion in heavy-duty engines," 2015. Paper No. 2015-01-0849.

[34] R. Hanson and R. Reitz, "Experimental investigation of engine speed transient operation in a light duty RCCI engine," *SAE International Journal of Engines*, vol. 7, no. 2, pp. 888–901, 2014.

[35] R. Hanson, A. Ickes, and T. Wallner, "Comparison of RCCI operation with and

without egr over the full operating map of a heavy-duty diesel engine," tech. rep., SAE Technical Paper, 2016. Paper No. 2016-01-0794.

[36] S. S. Kalsi and K. Subramanian, "Experimental investigations of effects of egr on performance and emissions characteristics of cng fueled reactivity controlled compression ignition (RCCI) engine," *Energy Conversion and Management*, vol. 130, pp. 91–105, 2016.

[37] J. Bengtsson, P. Strandh, R. Johansson, P. Tunestål, and B. Johansson, "Closed-loop combustion control of homogeneous charge compression ignition (HCCI) engine dynamics," *International Journal of Adaptive Control and Signal Processing*, vol. 18, no. 2, pp. Pages: 167–179, 2004.

[38] C.-J. Chiang, A. G. Stefanopoulou, and M. Jankovic, "Nonlinear observer-based control of load transitions in homogeneous charge compression ignition engines," *IEEE Transactions on Control Systems Technology*, vol. 15, no. 3, pp. Pages: 438–448, 2007.

[39] M. Shahbakhti and C. R. Koch, "Physics based control oriented model for HCCI combustion timing," *Journal of Dynamic Systems, Measurement, and Control*, vol. 132, no. 2, p. Pages: 021010, 2010.

[40] G. M. Shaver, J. C. Gerdes, P. Jain, P. Caton, and C. Edwards, "Modeling for control of HCCI engines," in *American Control Conference*, vol. 1, pp. Pages: 749–754, 2003.

[41] X. Yang, G. G. Zhu, and Z. Sun, "A control oriented SI and HCCI hybrid combustion model for internal combustion engines," in *ASME 2010 Dynamic Systems and Control Conference*, pp. Pages: 657–664, 2010.

[42] Y. Wu, R. Hanson, and R. D. Reitz, "Investigation of combustion phasing control strategy during reactivity controlled compression ignition (RCCI)," *Journal of Engineering for Gas Turbines and Power*, vol. 136, no. 9, 2014.

[43] K. Khodadadi Sadabadi, M. Shahbakhti, A. N. Bharath, and R. D. Reitz, "Modeling of combustion phasing of a reactivity-controlled compression ignition engine for control applications," *International Journal of Engine Research*, vol. 17, no. 4, pp. Pages: 421–435, 2016.

[44] A. Indrajuana, C. Bekdemir, X. Luo, and F. Willems, "Robust multivariable feedback control of natural gas-diesel RCCI combustion," *IFAC-PapersOnLine*, vol. 49, no. 11, pp. Pages: 217–222, 2016.

[45] A. Indrajuana, C. Bekdemir, E. Feru, and F. Willems, "Towards model-based control of RCCI-CDF mode-switching in dual fuel engines," 2018. Paper No. 2018-01-0263.

[46] J. K. Arora and M. Shahbakhti, "Real-time closed-loop control of a light-duty RCCI engine during transient operations," *SAE International*, 2017. Paper No. 2017-01-0767.

[47] N. N. T. Kondipati, J. K. Arora, M. Bidarvatan, and M. Shahbakhti, "Modeling, design and implementation of a closed-loop combustion controller for an RCCI engine," in *American Control Conference*, pp. 4747–4752, 2017.

[48] A. Raut, B. K. Irdmousa, and M. Shahbakhti, "Dynamic modeling and model predictive control of an RCCI engine," *Control Engineering Practice*, vol. 81, pp. Pages: 129–144, 2018.

[49] A. Raut, M. Bidarvatan, H. Borhan, and M. Shahbakhti, "Model predictive control of an RCCI engine," in *2018 Annual American Control Conference (ACC)*, pp. Pages: 1604–1609, IEEE, 2018.

[50] J. Mohammadpour and C. W. Scherer, *Control of linear parameter varying systems with applications*. Springer Science & Business Media, 2012.

[51] A. P. White, G. Zhu, and J. Choi, *Linear parameter-varying control for engineering applications*. Springer, 2013.

[52] W. J. Rugh and J. S. Shamma, "Research on gain scheduling," *Automatica*, vol. 36, no. 10, pp. 1401–1425, 2000.

[53] J. S. Shamma, *Analysis and design of gain scheduled control systems*. PhD thesis, Massachusetts Institute of Technology, 1988.

[54] J. S. Shamma and M. Athans, "Analysis of gain scheduled control for nonlinear

plants," *IEEE Transactions on Automatic Control*, vol. 35, no. 8, pp. 898–907, 1990.

[55] M. Nemani, R. Ravikanth, and B. A. Bamieh, "Identification of linear parametrically varying systems," in *Proceedings of 1995 34th IEEE Conference on Decision and Control*, vol. 3, pp. 2990–2995, IEEE, 1995.

[56] M. Lovera, M. Verhaegen, and C. Chou, "State space identification of mimo linear parameter varying models," in *Proceedings of the International Symposium on the Mathematical Theory of Networks and Systems*, pp. 839–842, 1998.

[57] L. H. Lee and K. Poolla, "Identification of linear parameter-varying systems via lfts," in *Proceedings of 35th IEEE Conference on Decision and Control*, vol. 2, pp. 1545–1550, IEEE, 1996.

[58] F. Previdi and M. Lovera, "Identification of a class of non-linear parametrically varying models," *International Journal of Adaptive Control and Signal Processing*, vol. 17, no. 1, pp. 33–50, 2003.

[59] B. Bamieh and L. Giarre, "Identification of linear parameter varying models," *International Journal of Robust and Nonlinear Control: IFAC-Affiliated Journal*, vol. 12, no. 9, pp. 841–853, 2002.

[60] P. Gáspár, I. Szaszi, and J. Bokor, "Active suspension design using lpv control," *IFAC Proceedings Volumes*, vol. 37, no. 22, pp. 565–570, 2004.

[61] C. Poussot-Vassal, C. Spelta, O. Sename, S. M. Savaresi, and L. Dugard, "Survey and performance evaluation on some automotive semi-active suspension control methods: A comparative study on a single-corner model," *Annual Reviews in Control*, vol. 36, no. 1, pp. 148–160, 2012.

[62] P. Gaspar, Z. Szabo, J. Bokor, C. Poussot-Vassal, O. Sename, and L. Dugard, "Towards global chassis control by integrating the brake and suspension systems," *IFAC Proceedings Volumes*, vol. 40, no. 10, pp. 563–570, 2007.

[63] Z. Szabó, P. Gáspár, and J. Bokor, "Design of integrated vehicle chassis control based on lpv methods," *Control of Linear Parameter Varying Systems with Applications*, pp. 513–534, 2012.

[64] X. Wei and L. Del Re, "Gain scheduled hinfinity control for air path systems of diesel engines using lpv techniques," *IEEE transactions on control systems technology*, vol. 15, no. 3, pp. 406–415, 2007.

[65] M. Jung and K. Glover, "Calibratable linear parameter-varying control of a turbocharged diesel engine," *IEEE Transactions on control systems technology*, vol. 14, no. 1, pp. 45–62, 2005.

[66] A. U. Genc, *Linear parameter-varying modelling and robust control of variable cam timing engines*. PhD thesis, Citeseer, 2003.

[67] A. P. White, *A Systematic Approach for Linear Parameter Varying Modeling*

and Control of Internal Combustion Engines. Michigan State University. Mechanical Engineering, 2012.

[68] C. Gauthier, O. Sename, L. Dugard, and G. Meissonnier, "Modelling of a diesel engine common rail injection system," *IFAC Proceedings Volumes*, vol. 38, no. 1, pp. 188–193, 2005.

[69] G. Christophe, O. Sename, L. Dugard, and G. Meissonnier, "An linear parameter-varying (lpv) controller for a diesel engine common rail injection system," in *2007 European Control Conference (ECC)*, pp. 1932–1939, IEEE, 2007.

[70] C. Gauthier, O. Sename, L. Dugard, and G. Meissonnier, "An lft approach to h control design for diesel engine common rail injection system," *Oil & Gas Science and Technology-Revue de l'IFP*, vol. 62, no. 4, pp. 513–522, 2007.

[71] Y. Ra and R. D. Reitz, "A combustion model for multi-component fuels using a physical surrogate group chemistry representation (psgcr)," *Combustion and Flame*, vol. 162, no. 10, pp. 3456–3481, 2015.

[72] A. Jamali, A. K. Purushothaman, and Y. Ra, "A combustion model for multi-component fuels based on relative reactivity and molecular structure," *Fuel*, vol. 292, p. 120291, 2021.

[73] L. Yin, M. Lundgren, Z. Wang, P. Stamatoglou, M. Richter, Ö. Andersson, and P. Tunestål, "High efficient internal combustion engine using partially premixed

combustion with multiple injections," *Applied Energy*, vol. 233, pp. 516–523, 2019.

[74] S. Vedharaj, R. Vallinayagam, Y. An, A. Dawood, M. I. Najafabadi, B. Somers, J. Chang, and B. Johansson, "Fuel effect on combustion stratification in partially premixed combustion," tech. rep., SAE Technical Paper, 2017. Paper No. 2017-24-0089.

[75] M. Tanaskovic, L. Fagiano, C. Novara, and M. Morari, "Data-driven control of nonlinear systems: An on-line direct approach," *Automatica*, vol. 75, pp. 1–10, 2017.

[76] D. Solomatine, L. M. See, and R. Abrahart, "Data-driven modelling: concepts, approaches and experiences," in *Practical Hydroinformatics*, pp. 17–30, Springer, 2009.

[77] M. Sjöberg and J. E. Dec, "Effects of engine speed, fueling rate, and combustion phasing on the thermal stratification required to limit HCCI knocking intensity," *SAE transactions*, pp. Pages: 1472–1486, 2005. Paper No. 2005-01-2125.

[78] R. Hanson, S. Curran, R. Wagner, and R. Reitz, "Effects of biofuel blends on RCCI combustion in a light-duty, multi-cylinder diesel engine," *SAE International Journal of Engines*, vol. 6, no. 1, pp. Pages: 488–503, 2013.

[79] A. Kakoee, Y. Bakhshan, A. Barbier, P. Bares, and C. Guardiola, "Modeling combustion timing in an RCCI engine by means of a control oriented model," *Control Engineering Practice*, vol. 97, p. Pages: 104321, 2020.

[80] W. Sui, J. Pulpeiro González, and C. M. Hall, "Modeling and control of combustion phasing in dual-fuel compression ignition engines," *Journal of Engineering for Gas Turbines and Power*, vol. 141, no. 5, 2019.

[81] L. A. Basina, B. K. Irdmousa, J. M. Velni, H. Borhan, J. D. Naber, and M. Shahbakhti, "Data-driven modeling and predictive control of maximum pressure rise rate in RCCI engines," in *2020 IEEE Conference on Control Technology and Applications (CCTA)*, pp. Pages: 94–99, IEEE, 2020.

[82] S. Z. Rizvi, J. Mohammadpour, R. Tóth, and N. Meskin, "A kernel-based approach to MIMO LPV state-space identification and application to a nonlinear process system," *IFAC-PapersOnLine*, vol. 48, no. 26, pp. Pages: 85–90, 2015.

[83] L. Wang, *Model Predictive Control System Design and Implementation using MATLAB®*. Springer Science & Business Media, 2009. *Chapter 1.*

[84] O. Mikulas, "Quadratic programming algorithms for fast model-based predictive control," Master's thesis, Czech Technical University, Prague, Czech Republic, 2013.

[85] B. K. Irdmousa, S. Z. Rizvi, J. M. Veini, J. Nabert, and M. Shahbakhti, "Data-driven modeling and predictive control of combustion phasing for RCCI engines," pp. 1617–1622, 2019.

[86] S. Z. Rizvi, J. M. Velni, F. Abbasi, R. Tóth, and N. Meskin, "State-space LPV model identification using kernelized machine learning," *Automatica*, vol. 88, pp. Pages: 38–47, 2018.

[87] T. W. Ryan III and T. J. Callahan, "Engine and constant volume bomb studies of diesel ignition and combustion," *SAE transactions*, pp. 756–764, 1988. Paper No. 881626.

[88] S. Curran, J. Szybist, B. Kaul, S. Sluder, and J. Easter, "Fuel stratification effects on gasoline compression ignition with a regular-grade gasoline on a single-cylinder medium-duty diesel engine at low load," *SAE Technical Paper*, vol. 2021, no. 01, 2021. Paper No. 2021-01-1173.

[89] W. H. Organization, *Global status report on road safety 2015*. World Health Organization, 2015.

[90] C. Zhang, C. Zhang, L. Xue, and Y. Li, "Combustion characteristics and operation range of a RCCI combustion engine fueled with direct injection n-heptane and pipe injection n-butanol," *Energy*, vol. 125, pp. 439–448, 2017.

[91] E. Ansari, T. Menucci, M. Shahbakhti, and J. Naber, "Experimental investigation into effects of high reactive fuel on combustion and emission

characteristics of the diesel-natural gas reactivity controlled compression ignition engine," *Applied Energy*, vol. 239, pp. 948–956, 2019.

[92] P. Harari, N. Banapurmath, V. Yaliwal, T. Y. Khan, M. E. M. Soudagar, and A. Sajjan, "Experimental studies on performance and emission characteristics of reactivity controlled compression ignition (RCCI) engine operated with gasoline and thevetia peruviana biodiesel," *Renewable Energy*, vol. 160, pp. 865–875, 2020.

[93] S. Pan, K. Cai, M. Cai, C. Du, X. Li, W. Han, X. Wang, D. Liu, J. Wei, J. Fang, *et al.*, "Experimental study on the cyclic variations of ethanol/diesel reactivity controlled compression ignition (RCCI) combustion in a heavy-duty diesel engine," *Energy*, vol. 237, p. 121614, 2021.

[94] L. Wang, J. Liu, Q. Ji, P. Sun, J. Li, M. Wei, and S. Liu, "Experimental study on the high load extension of pode/methanol RCCI combustion mode with optimized injection strategy," *Fuel*, vol. 314, p. 122726, 2022.

[95] Y. Li, M. Jia, Y. Chang, Y. Liu, M. Xie, T. Wang, and L. Zhou, "Parametric study and optimization of a RCCI (reactivity controlled compression ignition) engine fueled with methanol and diesel," *Energy*, vol. 65, pp. 319–332, 2014.

[96] S. Formentin, K. Van Heusden, and A. Karimi, "A comparison of model-based and data-driven controller tuning," *International Journal of Adaptive Control and Signal Processing*, vol. 28, no. 10, pp. 882–897, 2014.

[97] H. Hjalmarsson, "From experiment design to closed-loop control," *Automatica*, vol. 41, no. 3, pp. 393–438, 2005.

[98] K. Khodadadi Sadabadi and M. Shahbakhti, "Dynamic modelling and controller design of combustion phasing for an RCCI engine," vol. 50701, p. Pages: V002T20A004, 2016.

[99] T. Albin, P. Drews, F. Heßeler, A. M. Ivanescu, T. Seidl, and D. Abel, "A hybrid control approach for low temperature combustion engine control," pp. Pages: 6846–6851, 2011.

[100] A. Basina, "Modeling and control of maximum pressure rise rate in RCCI engines," Master's thesis, Michigan Technological University, 2019.

[101] U. E. I. Administration, "Annual Energy Outlook," January 2020 (Accessed: 11/01/2020). https://www.eia.gov/outlooks/aeo/pdf/AEO2020

[102] S. Batool, J. D. Naber, and M. Shahbakhti, "Data-driven modeling and control of cyclic variability of an engine operating in low temperature combustion modes," *IFAC-PapersOnLine*, vol. 54, no. 20, pp. 834–839, 2021.

[103] M. Vlaswinkel, B. de Jager, and F. Willems, "Data-based control structure selection for RCCI engines with electrically assisted turbocharger," in *2021 European Control Conference (ECC)*, pp. 491–496, IEEE, 2021.

[104] J. Verhaegh, F. Kupper, and F. Willems, "Data-driven air-fuel path control design for robust RCCI engine operation," *Energies*, vol. 15, no. 6, p. 2018, 2022.

[105] M. Shahbakhti, M. Ghafuri, A. Aslani, A. Sahraeian, S. Jazayeri, and S. Azadi, "A method to determine fuel transport dynamics model parameters in port fuel injected gasoline engines during cold start and warm-up conditions," *Journal of engineering for gas turbines and power*, vol. 132, no. 7, 2010.

[106] J. A. Suykens and J. Vandewalle, "Least squares support vector machine classifiers," *Neural processing letters*, vol. 9, no. 3, pp. Pages: 293–300, 1999.

[107] P. Drews, T. Albin, K. Hoffmann, N. Peters, D. Abel, *et al.*, "Model-based optimal control for PCCI combustion engines," *IFAC Proceedings Volumes*, vol. 43, no. 7, pp. Pages: 288–293, 2010.

[108] P. Drews, T. Albin, F.-J. Hesseler, N. Peters, and D. Abel, "Fuel-efficient model-based optimal MIMO control for PCCI engines," *IFAC Proceedings Volumes*, vol. 44, no. 1, pp. Pages: 12998–13003, 2011.

[109] AEO, "Annual Energy Outlook 2022 (aeo2022)," *Energy Information Agency*, p. 23, U.S. EIA 2022.

[110] L. Xia, B. de Jager, T. Donkers, and F. Willems, "Robust constrained optimization for RCCI engines using nested penalized particle swarm," *Control Engineering Practice*, vol. 99, p. 104411, 2020.

[111] M. Vlaswinkel, B. de Jager, and F. Willems, "Data-based in-cylinder pressure model including cyclic variations of an RCCI engine," *IFAC-PapersOnLine*, vol. 55, no. 24, pp. 13–18, 2022.

[112] W. Yu, F. Zhao, W. Yang, and H. Xu, "Integrated analysis of CFD simulation data with k-means clustering algorithm for soot formation under varied combustion conditions," *Applied Thermal Engineering*, vol. 153, pp. 299–305, 2019.

[113] C. Kavuri and S. L. Kokjohn, "Exploring the potential of machine learning in reducing the computational time/expense and improving the reliability of engine optimization studies," *International Journal of Engine Research*, vol. 21, no. 7, pp. 1251–1270, 2020.

[114] I. Morev, B. Tekgül, M. Gadalla, A. Shahanaghi, J. Kannan, S. Karimkashi, O. Kaario, and V. Vuorinen, "Fast reactive flow simulations using analytical jacobian and dynamic load balancing in openfoam," *Physics of Fluids*, vol. 34, no. 2, p. 021801, 2022.

[115] B. K. Irdmousa, J. D. Naber, J. M. Velni, H. Borhan, and M. Shahbakhti, "Input-output data-driven modeling and mimo predictive control of an RCCI engine combustion," *IFAC-PapersOnLine*, vol. 54, no. 20, pp. 406–411, 2021.

[116] M. Aliramezani, C. R. Koch, and M. Shahbakhti, "Modeling, diagnostics, optimization, and control of internal combustion engines via modern machine

learning techniques: A review and future directions," *Progress in Energy and Combustion Science*, vol. 88, p. 100967, 2022.

[117] W. Pan, M. Korkmaz, J. Beeckmann, and H. Pitsch, "Nonlinear identification modeling for PCCI engine emissions prediction using unsupervised learning and neural networks," tech. rep., SAE Technical Paper, 2020. Paper No. 2020-01-0558.

[118] J. Cao, J. Kim, M. Takahashi, and Y. Yamasaki, "Model based control with online automatic adaptation by neural network for advanced diesel combustion," *IFAC-PapersOnLine*, vol. 53, no. 2, pp. 14040–14046, 2020.

[119] D. Kakati, S. Roy, and R. Banerjee, "Development and validation of an artificial intelligence platform for characterization of the exergy-emission-stability profiles of the ppci-rcci regimes in a diesel-methanol operation under varying injection phasing strategies: A gene expression programming approach," *Fuel*, vol. 299, p. 120864, 2021.

[120] K. Yaovaja and W. Chatlatanagulchai, "Knock control in a diesel-dual-fuel premixed-charge compression-ignition (DF-PCCI) engine using a fuzzy supervisory system," *Agriculture and Natural Resources*, vol. 48, no. 1, pp. 120–138, 2014.

[121] J. Hu, Z. Chen, Y. Yao, L. Shi, and K. Deng, "Study on control-oriented

emission predictions of ppci diesel engine with two-stage fuel injection," *Fuel*, vol. 320, p. 123984, 2022.

[122] V. M. Janakiraman, X. Nguyen, and D. Assanis, "Nonlinear identification of a gasoline HCCI engine using neural networks coupled with principal component analysis," *Applied Soft Computing*, vol. 13, no. 5, pp. 2375–2389, 2013.

[123] A. Vaughan and S. V. Bohac, "An extreme learning machine approach to predicting near chaotic HCCI combustion phasing in real-time," *arXiv preprint arXiv:1310.3567*, 2013.

[124] V. M. Janakiraman, X. Nguyen, J. Sterniak, and D. Assanis, "Identification of the dynamic operating envelope of HCCI engines using class imbalance learning," *IEEE transactions on neural networks and learning systems*, vol. 26, no. 1, pp. 98–112, 2014.

[125] V. M. Janakiraman, X. Nguyen, J. Sterniak, and D. Assanis, "A system identification framework for modeling complex combustion dynamics using support vector machines," in *Informatics in Control, Automation and Robotics*, pp. 297–313, Springer, 2014.

[126] V. M. Janakiraman, X. Nguyen, and D. Assanis, "Nonlinear model predictive control of a gasoline HCCI engine using extreme learning machines," *arXiv preprint arXiv:1501.03969*, 2015.

[127] M. Taghavi, A. Gharehghani, F. B. Nejad, and M. Mirsalim, "Developing a model to predict the start of combustion in HCCI engine using ann-ga approach," *Energy Conversion and Management*, vol. 195, pp. 57–69, 2019.

[128] M. T. Henry de Frahan, N. T. Wimer, S. Yellapantula, and R. W. Grout, "Deep reinforcement learning for dynamic control of fuel injection timing in multi-pulse compression ignition engines," *International Journal of Engine Research*, vol. 23, no. 9, pp. 1503–1521, 2022.

[129] B. K. Irdmousa, L. A. Basina, J. Naber, J. M. Velni, H. Borhan, and M. Shahbakhti, "Control-oriented data-driven and physics-based modeling of maximum pressure rise rate in reactivity controlled compression ignition engines," *SAE International Journal of Engines*, vol. 16, no. 03-16-06-0040, 2022.

[130] A. A. Khameneian, B. K. Irdmousa, P. Dice, M. Shahbakhti, J. D. Naber, P. Moilanen, C. Archer, C. Glugla, and G. Huberts, "A dynamic method to analyze cold-start first cycles engine-out emissions at elevated cranking speed conditions of a hybrid electric vehicle including a gasoline direct injection engine," *SAE International Journal of Engines*, vol. 15, no. 03-15-06-0044, pp. 807–823, 2022.

[131] Y. Feng, H. Liu, Z. WANG, T. Wang, *et al.*, "Numerical investigation of the

combustion regime in pilot-ignited high-pressure direct injection (HPDI) low reactivity fuel combustion with the eccentric configuration of injection system,"

[132] G. Görmez and B. A. Çeper, "Numerical analysis of a reactivity controlled compression ignition engine," *Fuel*, vol. 307, p. 121819, 2022.

[133] A. Gharehghani, A. H. Fakhari, and M. Aghahasani, "Investigating the influence of injection timing on the performance of a RCCI engine," *Engine Research*, vol. 70, no. 1, pp. 91–105, 2023.

[134] S. M. Lashkarpour, R. K. Saray, and M. Najafi, "Multi-zone model for reactivity controlled compression ignition engine based on CFD approach," *Energy*, vol. 156, pp. 213–228, 2018.

[135] S. Heidarabadi, R. Khoshbakhti Saray, and E. Neshat, "Detailed kinetic study on methane/diesel RCCI combustion," *International Journal of Engine Research*, vol. 22, no. 8, pp. 2422–2441, 2021.

[136] B. K. Irdmousa, J. D. Naber, and M. Shahbakhti, "CFD-based data-driven modeling of reactivity and stratification dynamics for RCCI engine control," *IFAC-PapersOnLine*, vol. 56, no. 2, pp. 8272–8277, 2023.

Appendix A

PhD publications

A.1 Peer reviewed journal papers

A.1.1 Published journal papers

❶ BK Irdmousa, LNA Basina, J Naber, JM Velni, H Borhan, M Shahbakhti, "Control-Oriented Data-Driven and Physics-Based Modeling of Maximum Pressure Rise Rate in Reactivity Controlled Compression Ignition Engines", SAE International Journal of Engines 16 (03-16-06-0040)(Ref. [129])

❷ AA Khameneian, BK Irdmousa, P Dice, M Shahbakhti, JD Naber, "A Dynamic Method to Analyze Cold-Start First Cycles Engine-Out Emissions at Elevated

Cranking Speed Conditions of a Hybrid Electric Vehicle Including a Gasoline Direct Injection Engine", SAE International Journal of Engines 15 (03-15-06-0044), 807-823 (Ref. [130])

❸ A Raut, BK Irdmousa, M Shahbakhti, "Dynamic modeling and model predictive control of an RCCI engine", Control Engineering Practice 81, 129-144 (Ref. [48])

❹ K Poorghasemi, RK Saray, E Ansari, BK Irdmousa, M Shahbakhti, "Effect of diesel injection strategies on natural gas/diesel RCCI combustion characteristics in a light duty diesel engine", Applied energy 199, 430-446 (Ref. [27])

A.1.2 Journal paper in preperation

❶ BK Irdmousa, J Naber, M Shahbakhti, "Data-driven Identification of Reactivity and Stratification Dynamics at RCCI Engines Based on Kernel Canonical Correlation Analysis", under preperation to Submit to Controls Engineering Practice

A.2 Refereed conference papers

❶ BK Irdmousa, J Naber, M Shahbakhti, "CFD-based Data-driven Modeling of Reactivity and Stratification Dynamics for RCCI Engine Control", IFAC

Modeling, Estimation and Control Conference 2023, July 9 - 14, 2023, Tokyo (Ref. [136])

❷ P BK Irdmousa, JD Naber, JM Velni, H Borhan, M Shahbakhti, "Input-output Data-driven Modeling and MIMO Predictive Control of an RCCI Engine Combustion", IFAC-PapersOnLine 54 (20), 406-411. (Ref. [115])

❸ BK Irdmousa, SZ Rizvi, JM Veini, JD Nabert, M Shahbakhti, "Data-driven modeling and predictive control of combustion phasing for RCCI engines", 2019 American Control Conference (ACC), 1617-1622. (Ref. [85])

❹ LNA Basina, BK Irdmousa, JM Velni, H Borhan, JD Naber, M Shahbakhti, "Data-driven modeling and predictive control of maximum pressure rise rate in RCCI engines", 2020 IEEE conference on control technology and applications (CCTA), 94-99. (Ref. [81])

❺ E Ansari, K Poorghasemi, BK Irdmousa, M Shahbakhti, J Naber, "Efficiency and emissions mapping of a light duty diesel-natural gas engine operating in conventional diesel and RCCI modes", SAE Technical Paper 2016-01-2309, 94-99. (Ref. [4])

Appendix B

PhD Research Data Repository

Appendix B represents list of model files and data developed in this study. This data is divided into models and visualization sections. The models section presents lists of MATLAB and CONVERGE models developed in this research. The visualization section provides MATLAB figures and Visio plots used in this dissertation. These sections are divided into chapter 2, chapter 3, chapter 4, and chapter 5 subsections.

B.1 Models

Lists of model files developed in each chapter of this research are described in the following subsections.

B.1.1 Chapter 2

File Name	Description
*allengine*68.*sdf*	compiled Simulink model
*Allengine*68.*slx*	RCCI Engine Operational and control model
Angle_Check.m	TDC calibration model
*CA*50.*m*	CA50 computation model
EOC.m	start of combustion estimation
HRR.m	Heat Release Rate Calculation
LPV_sim_final.slx	Linear Parameter Varying Model
Pegging.m	Pegging model

Table B.1
dSPACE LPV based MPC Controller. Location: *PhD Data\Models\Chapter 2\dSPACE LPV based MPC Controller)*

.

File Name	Description
$bfr.m$	best fit ratio calculation
$devec.m$	Lagrangian multiplier matrix development
$LPV\_Identifcation.m$	Linear parameter varying main model
$lssvmss\_eval.m$	LPV estimation evaluation
$lssvmss\_train.m$	LPV training model
$Test.mat$	test data
$vec.m$	vectorization matrix

Table B.2
Linear Parameter Varying Identification. Location: *PhD Data\Models\Chapter 2\LPV Identification)*

.

B.1.2 Chapter 3

File Name	Description
autotuner.m	inter-detailed algorithm
bfr.m	best fit ratio calculator
devec.m	Lagrangian multiplier matrix development
Dynamic_Seclection.m	state space matrices elements sorting
fmincost.m	function minimization using the downhill simplex algorithm
kcca_statest.m	unknown states estimation model
kernel.m	kernel functions description
lssvmss_eval.m	LPV estimation accuracy evaluation
lssvmss_train.m	LPV training model
main_engine.m	LPV estimation model
$US_Data_Visualization.m$	unknown states estimation visualization
vec.m	vectorization matrix

Table B.3
Unknown States LPV identification. Location: *PhD Data\Models\Chapter 3\Unknown States LPV identification)*

.

File Name	Description
$Constrained\_MPC.m$	constrained model predictive controller
$Controller\_Performance\_Plot.m$	controller performance visualization
$Kalman\_Gain\_calculator.m$	Kalman gain estimation algorithm
$RCCI\_dyn.m$	validated RCCI engine model
$RCCI\_dyn\_MPRR.m$	RCCI engine model with MPRR
$US\_LPV\_MPC\_Con.slx$	US LPV MPC controller
$US\_LPV\_MPC\_Con\_CA50.slx$	US LPV MPC controller for CA50
$US\_LPV\_MPC\_Con\_CA50\_IMEP.slx$	US LPV MPC controller for CA50 and IMEP
$US\_LPV\_MPC\_Con\_IMEP.slx$	US LPV MPC controller for IMEP
$US\_LPV\_MPC\_CA50\_IMEP\_C.slx$	constrained MIMO US LPV MPC controller

Table B.4
Unknown States (US) LPV MPC Controller. Location: *PhD Data\Models\Chapter 3\Unknown States (US) LPV MPC Controller*

.

B.1.3 Chapter 5

File Name	Description
bfr.m	best fit ratio calculation
devec.m	Lagrangian multiplier matrix development
kernel.m	kernel functions description
LPV_MPRR_1_Output.m	MPRR LPV estimation with 1 output
LPV_MPRR_3_Outputs.m	MPRR LPV estimation with 3 output
LPV_MPRR_reduced_States.m	Reduced states MPRR LPV estimation
lssvmss_eval.m	LPV estimation accuracy evaluation
lssvmss_train.m	LPV training model
Matrix_Plots.m	LPV state elements plot
vec.m	vectorization matrix

Table B.5
Known State MPRR Modeling. Location: *PhD Data\Models\Chapter 4\Data Driven MPRR Models\Known State MPRR Modeling*

.

File Name	Description
autotuner.m	inter-detailed algorithm
$bfr.m$	best fit ratio calculator
devec.m	Lagrangian multiplier matrix development
Dynamic_Seclection	state space matrices elements sorting
$fmincost.m$	downhill simplex function minimization
$KCCA\_MPRR\_1\_Output.m$	Unknown States MPRR estimation, 1 output
$KCCA\_MPRR\_3\_Outputs.m$	Unknown States MPRR estimation, 3 outputs
$KCCA\_MPRR\_3\_Outputs\_State\_Var.m$	Effect of unknown states number
kernel.m	kernel functions description
$lssvmss\_eval.m$	LPV estimation accuracy evaluation
$lssvmss\_train.m$	LPV training model
$US\_Data\_Visualization.m$	unknown states estimation visualization
vec.m	vectorization matrix

Table B.6
Unknown State MPRR Modeling. Location: *PhD Data\Models\Chapter 4\Data Driven MPRR Models\Unknown State MPRR Modeling*

.

File Name	Description
HR_analysis.mlx	Heat Release calculation
MPRR_modeling.mlx	MPRR model calibration
MPRR_Transient.m	Transient MPRR
Physics_Based_MPRR.m	Physics based MPRR model
RCCI_1000RPM_combined.mat	Experimental RCCI data for MPRR
RCCI_newdata_EXP_40.mat	Experimental RCCI data for MPRR (II)
Statistical_Analysis.mlx	Wiebe function calibration model

Table B.7
Physics based MPRR Model. Location: *PhD Data\Models\Chapter 4\Physics based MPRR Model*

.

B.1.4 Chapter 5

File Name	Description
amr.in	adaptive mesh refinement
boundary.in	Surface boundaries definition
combust.in	combustion model details
engine.in	engine geometry definition
gas.dat	Gas phase thermodynamic properties definition
initialize.in	Simulation initialization settings
inputs.in	general model inputs
liquid.dat	Gas phase thermodynamic properties definition
mech.dat	chemical mechanism definitions
post.in	post simulation data saving settings
rate.in	fuel injection rate profile
solver.in	computational solver settings
spray.in	fuel spray model settings
$surface.dat$	model geometry surface
turbulence.in	turbulence model settings

Table B.8
Closed Cycle RCCI CFD Model. Location: *PhD Data\Models\Chapter 5\Computational Fluid Dynamic Models\Closed Cycle RCCI CFD Model*

.

File Name	Description
amr.in	adaptive mesh refinement
boundary.in	Surface boundaries definition
combust.in	combustion model details
engine.in	engine geometry definition
gas.dat	gas phase thermodynamic properties definition
initialize.in	Simulation initialization settings
inputs.in	general model inputs
intake_lift.in	intake lift profiles
liquid.dat	liquid phase thermodynamic properties definition
mech.dat	chemical mechanism definitions
post.in	post simulation data saving settings
rate.in	fuel injection rate profile
solver.in	computational solver settings
spray.in	fuel spray model settings
surface.dat	model geometry surface
turbulence.in	turbulence model settings

Table B.9
Open Cycle RCCI CFD Model. Location: *PhD Data\Models\Chapter 5\Computational Fluid Dynamic Models\Open Cycle RCCI CFD Model*

.

File Name	Description
boundary.in	Surface boundaries definition
combust.in	combustion model details
$CONVERGE13.m$	MATLAB model for running CONVERGE
gas.dat	gas phase thermodynamic properties definition
initialize.in	Simulation initialization settings
inputs.in	general model inputs
liquid.dat	liquid phase thermodynamic properties definition
mech.dat	chemical mechanism definitions
post.in	post simulation data saving settings
$surface.dat$	model geometry surface
turbulence.in	turbulence model settings

Table B.10
Ignition delay data generator. Location: *PhD Data\Models\Chapter 5\Dual Fuel Reactivity Model \Ignition delay data generator*

.

File Name	Description
Data_all_new.mat	Ignition delay data
linear_regression.m	multiple linear regression model

Table B.11
Ignition Delay Regression Model. Location: *PhD Data\Models\Chapter 5\Dual Fuel Reactivity Model \Ignition Delay Regression Model*

.

B.2 Visualizations

This section presents a list of MATLAB figures and Visio documents developed in this research. It is divided into four subsections based on main dissertation chapters.

B.2.1 Chapter 2

File Name	Description
ControllerSetup.jpg	LPV based MPC controller setup
ControllerSetup.vsdx	Visio file of the LPV based MPC controller setup
FQvarition.jpg	control performance with variable FQ
*LPVValidationPR*20*.jpg*	LPV-SS model validation for PR=20
*LPVValidationPR*40*.jpg*	LPV-SS model validation for PR=40
LTCEngineSetup.jpg	RCCI Engine Setup
LTCEngineSetup.vsdx	Visio file RCCI Engine Setup
PRvarition.jpg	control performance with variable PR
$Setup_Image.jpg$	experimental RCCI setup
$Setup_Image.vsdx$	Visio file for the experimental RCCI setup

Table B.12
Chapter 2 visualization files list. Location: *PhD Data\Visualizations\Chapter 2*

.

B.2.2 Chapter 3

File Name	Description
A_matrix_paper.jpg	LPV representaion of "A" matrix by KCCA
*CA*50*_Con.jpg*	controller Performance with constant CA50
*CA*50*IMEP_Var.jpg*	control performance with variable CA50 and IMEP
IMEP_con.jpg	control performance with constant IMEP
Controller_Setup.jpg	KCCA based MPC controller setup
Controller_Setup.vsdx	Visio for KCCA based MPC controller
*PR*_10*.jpg*	Experimental training and test data
*PR*26*_USLPV.jpg*	unknown states LPV validation
State_Variation.jpg	Effect of number of states on estimation

Table B.13
Chapter 3 visualization files list. Location: *PhD Data\Visualizations\Chapter 3*

.

B.2.3 Chapter 4

File Name	Description
AB_matrix_KCCA	Variation of A and B matrices elements
KCCA.jpg	KCCA MPRR estimation performance
LPV.jpg	LPV MPRR estimation performance
physics_based.jpg	Physics based MPRR estimation performance
PR_14_20_28_compare.jpg	MPRR estimation comparison
States_effect.jpg	Effect of number of states on
Three_PRs.jpg	Experimental training and test data
Wiebe_compare.jpg	Single and double Wiebe function estimations

Table B.14
Chapter 4 visualization files list. Location: *PhD Data\Visualizations\Chapter 4*

.

B.2.4 Chapter 5

File Name	Description
Three_PRs.jpg	CFD test plan
CFD_Validation.jpg	Transient open cycle CFD model validation
CFD_Validation_Steady.jpg	Steady state open cycle CFD model validation
Geometry.png	Open cycle CFD model geometry
Ignition_Delay_Validation.jpg	Ignition delay validation
Ignitiondelay_Reactants.jpg	Simulated Reactor model Ignition Delay
MLR_Ignition_Delay.jpg	Validation for multiple linear regression
OH_concentration.jpg	Hydroxyl concentration during reactor simulation
RRI_FQ_2mg.png	RRI distribution at FQ=2mg/cycle
RRI_FQ_4mg.png	RRI distribution at FQ=4mg/cycle
RRI_FQ_6mg.png	RRI distribution at FQ=6 mg/cycle
RRI_PR_00.png	RRI distribution at PR=0 %
RRI_PR_30.png	RRI distribution at PR=30 %
RRI_PR_50.png	RRI distribution at PR=50 %
RRI_Scatter.jpg	Scatter plot of relative reactivity levels
RRI_SOI_15bTDC.jpg	RRI distribution at SOI=15 bTDC
RRI_SOI_35bTDC.jpg	RRI distribution at SOI=35 bTDC

File Name	Description
$RRI\_SOI\_55bTDC.jpg$	RRI distribution at SOI=55 bTDC
$SI_FQ_2mg.jpg$	SI distribution at FQ=2 mg/cycle
$SI\_FQ\_4mg.jpg$	SI distribution at FQ=4 mg/cycle
$SI\_FQ\_6mg.jpg$	SI distribution at FQ=6 mg/cycle
$SI\_PR\_00.jpg$	SI distribution at PR=0 %
$SI\_PR\_30.jpg$	SI distribution at PR=30 %
$SI\_PR\_50.jpg$	SI distribution at PR=50 %
$SI\_Scatter.jpg$	Scatter plot of SI levels
$SI\_SOI\_15bTDC.jpg$	SI distribution at SOI 15 (bTDC)
$SI\_SOI\_35bTDC.jpg$	SI distribution at SOI 35 (bTDC)
$SI\_SOI\_55bTDC.jpg$	SI distribution at SOI 55 (bTDC)

Table B.15
Chapter 5 visualization files list. Location: *PhD Data\Visualizations\Chapter 5*

.

Appendix C

Letters of permission to republish

Letters of permission and publisher policies to reuse material from previously published journal and conference papers is included in this section:

permission granted

External Inbox ×

IFAC Secretariat <secretariat@ifac-control.org>
to me

Dear Behrouz Khoshbakht Irdmousa,

We were forwarded your request.

You are the author of the paper published in IFAC-PapersOnLine and, according to the copyright of the paper, you are the owner and you can use the paper in your thesis. The appropriate acknowledgment to the original publication to be included in your dissertation should be:

© 2021 The Authors. Originally published in IFAC-PapersOnLine, 54-20 (2021), pp. 406-411.

Best regards,

Elske Haberl

--
IFAC Secretariat
Schlossplatz 12, A-2361 Laxenburg
Austria, EUROPE
Phone : +43/2236/71447
E-Mail : secretariat@ifac-control.org